Thermal Integration of a Liquid Acquisition Device Into a Cryogenic Feed System

L.J. Hastings
Alpha Technology, Inc., Huntsville, Alabama

L.G. Bolshinskiy
The University of Alabama in Huntsville, Huntsville, Alabama

R.G. Schunk, A.K. Martin, R.H. Eskridge, B.D. Hamill, and C.F. Gomez
Marshall Space Flight Center, Huntsville, Alabama

A. Frenkel
The University of Alabama, Tuscaloosa, Alabama

G. Grayson
Boeing Company, Huntington Beach, California

M.L. Pendleton
Jacobs Engineering Group, Huntsville, Alabama

The NASA STI Program…in Profile

Since its founding, NASA has been dedicated to the advancement of aeronautics and space science. The NASA Scientific and Technical Information (STI) Program Office plays a key part in helping NASA maintain this important role.

The NASA STI Program Office is operated by Langley Research Center, the lead center for NASA's scientific and technical information. The NASA STI Program Office provides access to the NASA STI Database, the largest collection of aeronautical and space science STI in the world. The Program Office is also NASA's institutional mechanism for disseminating the results of its research and development activities. These results are published by NASA in the NASA STI Report Series, which includes the following report types:

- TECHNICAL PUBLICATION. Reports of completed research or a major significant phase of research that present the results of NASA programs and include extensive data or theoretical analysis. Includes compilations of significant scientific and technical data and information deemed to be of continuing reference value. NASA's counterpart of peer-reviewed formal professional papers but has less stringent limitations on manuscript length and extent of graphic presentations.

- TECHNICAL MEMORANDUM. Scientific and technical findings that are preliminary or of specialized interest, e.g., quick release reports, working papers, and bibliographies that contain minimal annotation. Does not contain extensive analysis.

- CONTRACTOR REPORT. Scientific and technical findings by NASA-sponsored contractors and grantees.

- CONFERENCE PUBLICATION. Collected papers from scientific and technical conferences, symposia, seminars, or other meetings sponsored or cosponsored by NASA.

- SPECIAL PUBLICATION. Scientific, technical, or historical information from NASA programs, projects, and mission, often concerned with subjects having substantial public interest.

- TECHNICAL TRANSLATION. English-language translations of foreign scientific and technical material pertinent to NASA's mission.

Specialized services that complement the STI Program Office's diverse offerings include creating custom thesauri, building customized databases, organizing and publishing research results…even providing videos.

For more information about the NASA STI Program Office, see the following:

- Access the NASA STI program home page at <http://www.sti.nasa.gov>

- E-mail your question via the Internet to <help@sti.nasa.gov>

- Fax your question to the NASA STI Help Desk at 443–757–5803

- Phone the NASA STI Help Desk at 443–757–5802

- Write to:
  NASA STI Help Desk
  NASA Center for AeroSpace Information
  7115 Standard Drive
  Hanover, MD 21076–1320

Thermal Integration of a Liquid Acquisition Device Into a Cryogenic Feed System

L.J. Hastings
Alpha Technology, Inc., Huntsville, Alabama

L.G. Bolshinskiy
The University of Alabama in Huntsville, Huntsville, Alabama

R.G. Schunk, A.K. Martin, R.H. Eskridge, B.D. Hamill, and C.F. Gomez
Marshall Space Flight Center, Huntsville, Alabama

A. Frenkel
The University of Alabama, Tuscaloosa, Alabama

G. Grayson
Boeing Company, Huntington Beach, California

M.L. Pendleton
Jacobs Engineering Group, Huntsville, Alabama

Acknowledgments

TRADEMARKS

Available from:

NASA Center for AeroSpace Information
7115 Standard Drive
Hanover, MD 21076–1320
443–757–5802

This report is also available in electronic form at
<https://www2.sti.nasa.gov/login/wt/>

TABLE OF CONTENTS

TABLE OF CONTENTS (Continued)

LIST OF FIGURES

LIST OF FIGURES (Continued)

LIST OF TABLES

LIST OF ACRONYMS AND SYMBOLS

CFD   computational fluid dynamics

CMFR   condensation mass flow rate

GRC   Glenn Research Center

LAD   liquid acquisition device

LCH_4 liquid methane

LN_2 liquid nitrogen

LO_2 liquid oxygen

MHTB   multipurpose hydrogen test bed

MLI   multilayer insulation

MSFC   Marshall Space Flight Center

o.d.   outside diameter

PIV   particle image velocimetry

PMD   propellant management device

RCS   reaction control system

TC   thermocouple

TP   Technical Publication

TVS   thermodynamic vent system

NOMENCLATURE

A	area
a_0	constant for particular screen and liquid being used
C_1	constant
C_2	constant
D_c	capillary diameter
D_e	effective diameter
D_h	hydraulic diameter
G_{th}	thermal conductance
g_c	acceleration of gravity (9.8 m/s^2)
h_f	film heat transfer coefficient
h_{wall}	convective heat transfer coefficient at the wall
k	thermal conductivity
l	wicking distance (m)
N_R	Raleigh number
$P_{\text{heating}}, P_{\text{h}}$	heating power
P_{out}	applied heating power
Q	heat rate (W)
r	radius
s_v	standard deviation in the velocity measurements
T	temperature
T_{sink}	radiative boundary temperature
t	wicking time (s)
t_0	starting time constant of the liquid uptake
z	height
z_0	starting position constant of the liquid uptake
Δ	thermal conductivity
ε	infrared emissivity
σ_v	standard deviation in velocity
χ^2	goodness-of-fit parameter

TECHNICAL PUBLICATION

THERMAL INTEGRATION OF A LIQUID ACQUISITION DEVICE INTO A CRYOGENIC FEED SYSTEM

1. BACKGROUND

Despite the fact that capillary liquid acquisition devices (LADs) (fig. 1) have been used extensively in space-based storable propellant systems, there has been no on-orbit application with cryogenic propellants. Although the principles of surface tension are the same for both storable and cryogenic liquids, there are additional thermal control challenges inherent in the cryogen application. The propulsion system of interest in this program is the liquid oxygen (LO_2)/liquid methane (LCH_4) version of the lunar lander ascent stage wherein the reaction control system (RCS) propellants are supplied by a LAD within the main stage propellant tank. A LAD is therefore required to retain sufficient propellant to supply the RCS during rendezvous and docking maneuvers that follow the main engine burn and achievement of lunar orbit. Because the LAD interfaces directly with the feed system (fig. 2), which can be a significant heat leak source, the gradual accumulation of heat within a representative capillary LAD for the upper stage during long storage periods (up to 210 days) on the lunar surface is the main issue addressed herein. This accumulation can lead to feed system cavitation during propellant outflow.
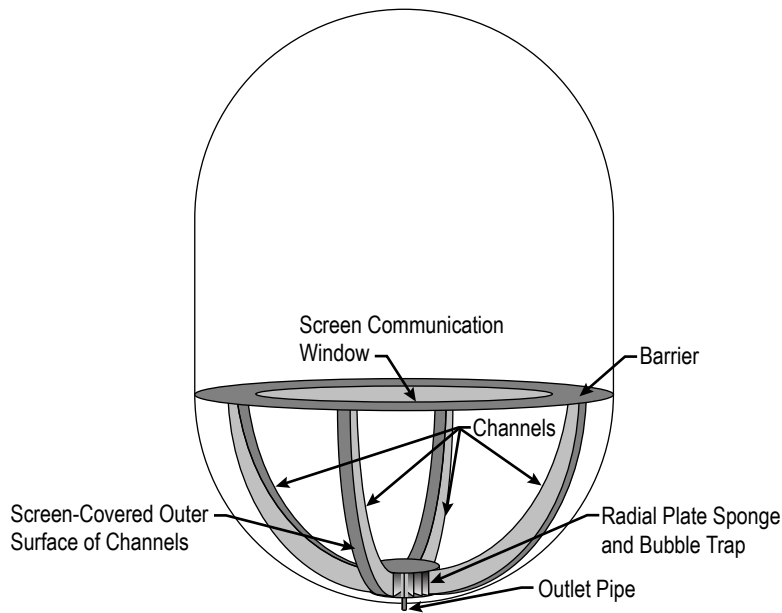
Figure 1. Representative LAD concept.
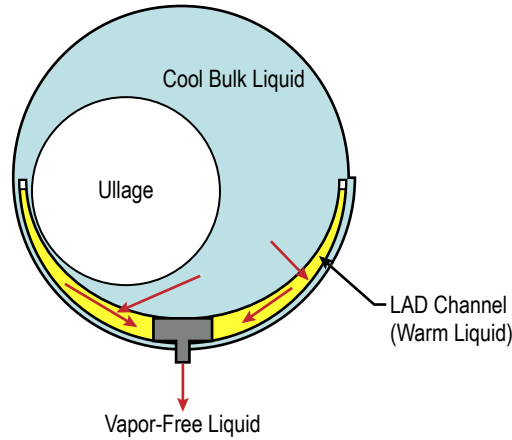
Figure 2. Thermal energy distributions within LADs.

The purpose of the work described in this Technical Publication (TP) is to determine the temperatures of propellants within the LAD, whether or not this will be a problem, and mitigation options. This is addressed both by computational modeling and testing.

1.1 Screen Heat Entrapment

The fundamental question first addressed by the Liquid Acquisition/Heat Entrapment program was: "To what degree are natural convection and the resultant mixing in a cryogenic liquid constrained by the capillary screen meshes envisioned for the LADs; i.e., how does one analytically model the effect of screen meshes on natural convection?"[1] Testing was first conducted with water as the test fluid, followed by liquid nitrogen (LN$_2$) tests. In either case, the basic experimental approach was to heat the bottom of a cylindrical column of test fluid that was 19.1 cm in diameter $\times$ 106 cm high to establish stratification patterns measured by temperature sensors located above and below a horizontal screen barrier position. Testing was conducted without barriers, with screens, and with a solid barrier. The two screen meshes tested were those typically used by LAD designers, 200$\times$1,400 and 325$\times$2,300, both with twill dutch weave.

Test results with water indicated that, with a barrier, temperatures below the barrier position consistently increased more rapidly than without the barriers, indicating the accumulation of thermal energy or heat entrapment. Neither mesh allowed the passage of convective currents; however, the fine mesh—being considerably thinner—allowed a greater degree of thermal conduction from the lower to the upper compartment. Also, although the aluminum solid plate represents the most complete barrier against convective flow, it actually showed a greater amount of heat transfer than either of the two mesh samples. Apparently this is due to the higher thermal conductivity of the aluminum barrier as compared to the stainless steel screen mesh. Therefore, with water as the test fluid, the 200$\times$1,400 and 325$\times$2,300 capillary screen meshes both represented barriers impervious to natural convection currents at two heater power levels, 920 and 1,840 W.

2

LN$_2$ testing was conducted within a 506l stainless steel Dewar. An inner polycarbonate cylinder, which was the same as that used in the water tests, was installed inside the Dewar to shield the stratification created by the heater from the sidewall heating effects. It is within this restricted volume that the experiment was conducted. Although stratification created by the 104 W heater was somewhat obscured by the heat leaks from the Dewar's top and bottom, the effects of heat entrapment were evident. Therefore, upon consideration of both the water and the LN$_2$ data, one can conclude that heat transfer across the screen meshes evaluated was dependent upon barrier thermal conductivity and that the passage of natural convection through the screens was effectively blocked. In conclusion, future LAD heat entrapment thermal analyses should consider only thermal conduction across capillary screen barriers with either 200×1,400 or 325×2,300 meshes.

Whether or not the constrained convection leads to an unacceptable degree of localized stratification was not the subject of this initial investigation, because such a determination is dependent on specific engine operational requirements, tank/feed system thermal characteristics, the propellant, vehicle orientation, and mission profile. Therefore, the objective of the next step was to investigate the thermal issues associated with the lunar ascent stage feed system for the LO$_2$/LCH$_4$ propulsion concept.

2. APPROACH AND OBJECTIVES OVERVIEW

The heat entrapment evaluation approach depicted in figure 3 implements both experimental and analytical facets and uses a cross section of talent within government, industry, and academia. The approach and objectives include (a) thermal modeling of the LAD interior temperatures and heat transfer across the feed line and bulk fluid interfaces; (b) computational fluid dynamics (CFD) analyses to define bulk liquid thermal environments surrounding the LAD, thereby providing boundary conditions for the LAD thermal modeling; (c) testing and analyses of condensation conditioning techniques for stabilizing LAD liquid retention characteristics; and (d) fluid systems thermal integration testing using a full-scale LAD mockup submerged in water and interfaced with a range of feed line heat leaks. Once the potential for accumulating thermal energy within the LAD channels is quantified, measures to mitigate the problem can be devised with more confidence.
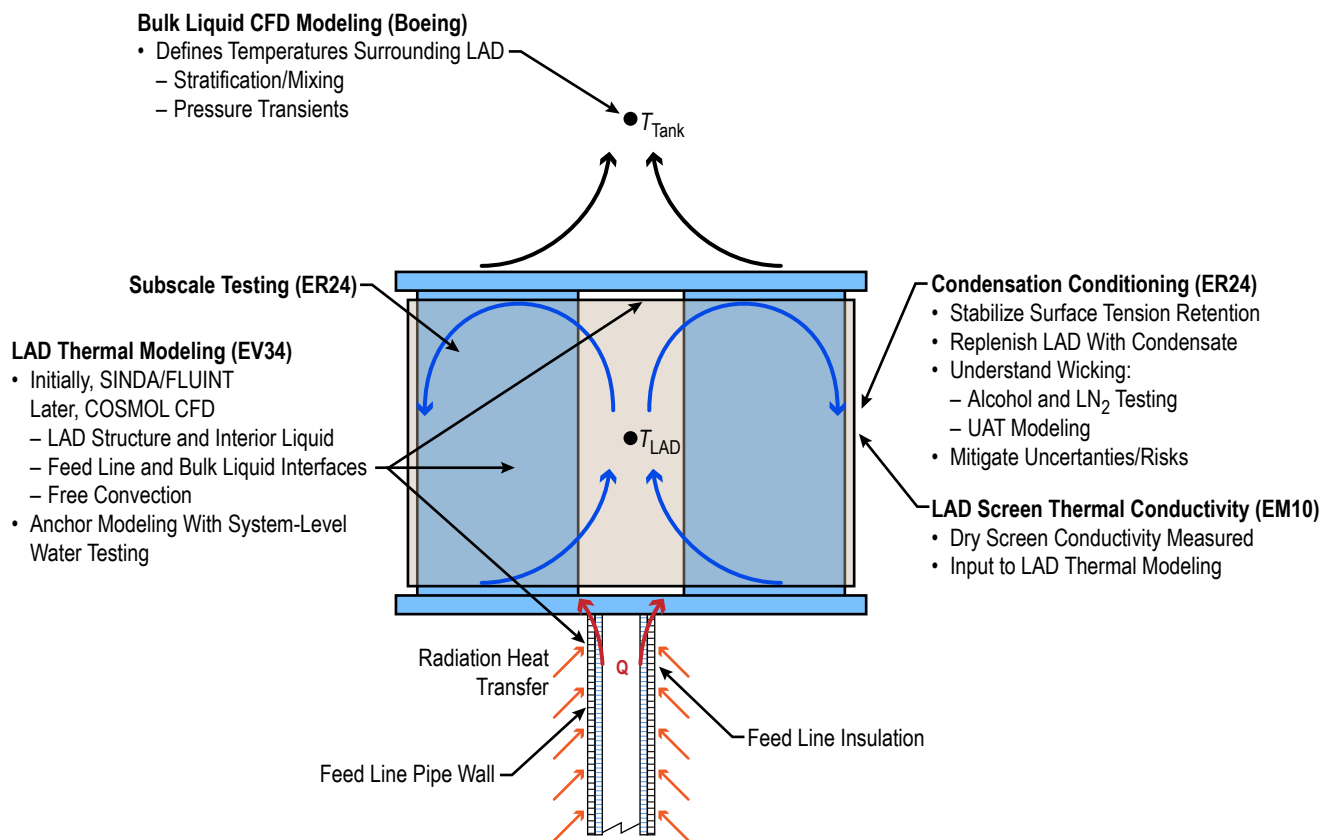
Figure 3. LO_2/LCH_4 ascent stage LAD heat entrapment overview.

3. LIQUID ACQUISITION DEVICE/FEED SYSTEM THERMAL MODELING

Because capillary screens used in LADs effectively block the passage of natural convection,[1] heat migrating from the feed system could accumulate within the LAD and elevate propellant temperatures. Thus, the basic objectives of this program element are to (a) quantify thermal energy entrapment for a representative LAD/feed system interface, (b) identify mitigation techniques as necessary, and (c) establish modeling techniques that can be used to evaluate other LAD/feed system concepts.

3.1 Preliminary Analyses

Initially, a thermal desktop model of the LAD was developed to evaluate trends and sensitivities to various parameters (fig. 4). The model included structural conduction and feed line heat leak, whereas convective effects were modeled empirically.
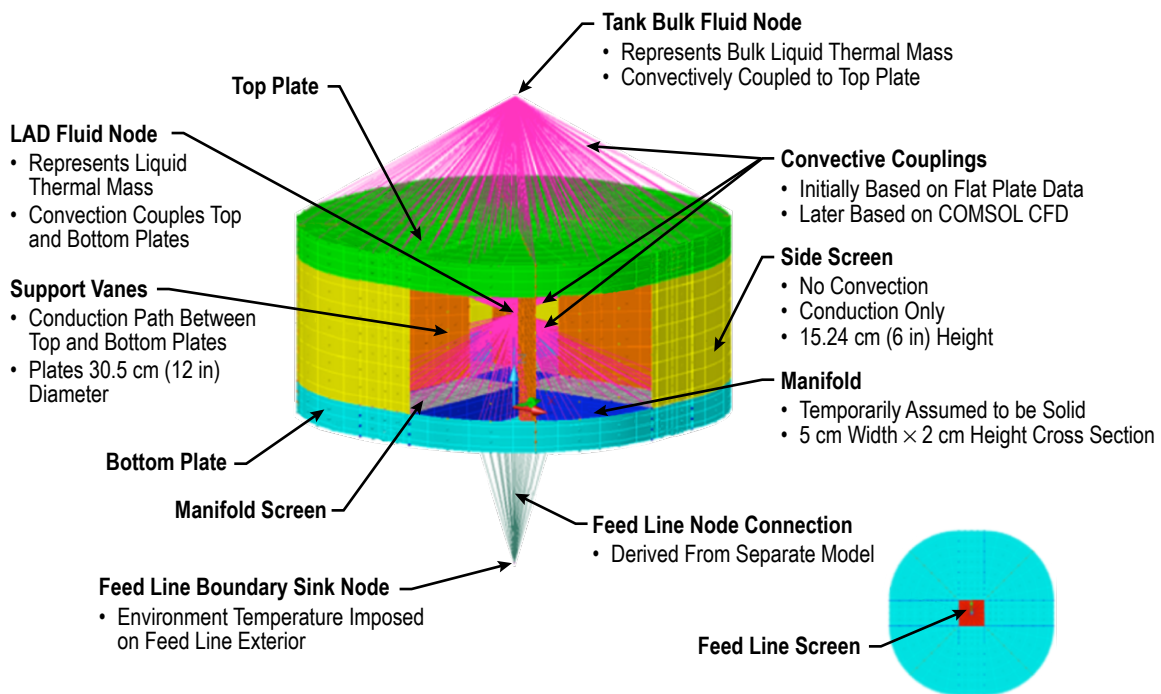
Figure 4. LAD thermal desktop model approach schematic with assumptions.

The representative LAD design was provided by D. Chato, NASA Glenn Research Center (GRC). The LAD is 30.48 cm (12 in) in diameter by 15.24 cm (6 in) high. The side is 325×2,300 stainless steel dutch twill mesh. The same mesh is used on the bottom of the liquid acquisition channels. The channel cross section is 2.54 cm (1 in) high by 5.08 cm (2 in) wide with a 325×2,300 mesh screen

covering the open area that faces downward. The LAD, which is applicable to both LO_2 and LCH_4, encloses a volume of $0.014\ m^3$ ($0.5\ ft^3$).

The key assumptions were as follows:

- No thermal isolation provisions existed between feed line and LAD; no coupling from feed line to the tank wall.

- The feed line screen was positioned at the entrance into the LAD; external coupling/heat leak was applied on the screen.

- The external heat leak into the tank through a multilayer insulation (MLI) blanket was not considered in this analysis.

- Solid top and bottom LAD covers were coupled by natural convection through a common fluid node inside the device as well as by conduction through the support vanes and outer screen.

- Only natural convection was considered from the top plate external to the LAD; convection coefficients were determined from empirical flat plate formulas.

- All analyses were performed with LCH_4 as working fluid because similar modeling with LO_2 indicated no significant differences.

A separate feed line model was used to determine the thermal coupling between the LAD and the environment (fig. 5). Because the environmental sink temperature was generally greater than the propellant temperature within the tank, heat absorbed by the feed line was conducted into the tank. The feed line base temperature (i.e., the LAD junction) was conservatively assumed to be 93 K. The propellant feed line was modeled as a 3-m-long, 38.1-mm-outside-diameter (o.d.), stainless steel cylinder with 1.65-mm-thick walls (1.5-in tube, 0.065-in wall) and was insulated with an MLI wrap that had an effective $\varepsilon = 0.05$. The feed line surface was coupled to a radiative boundary condition (i.e., sink temperature). The feed line was evacuated during the 210-day lunar surface mission and treated as an infinite fin accepting heat via radiation from the environment at temperature T_{sink}. Results from this model are summarized in figure 6, which depicts the cumulative heat entrapped in the basket versus days on the lunar surface.

After 20–30 days, the cumulative energy levels out at <2% of the total heat leak into the LAD volume for both LO_2 and LCH_4. Hence, the temperature difference between the fluid in the LAD volume and the tank at large is generally <1 K for the external feed line sink temperatures under consideration and for mission durations of 210 days or less.

The feed line sink temperature is parameterized in the model with the heat leak into the LAD computed at each sink temperature. The LAD base temperature (93 K) is subtracted from each sink temperature to create an array of heat load versus ΔT (fig. 7). An effective coupling is computed at each ΔT with the resulting Q versus ΔT array used in the LAD model to connect the feed line sink node to the base of the LAD. In the expected range of average feed line sink temperatures for a lunar application (170–90 K), the heat leak into the LAD is <0.4 W.

6
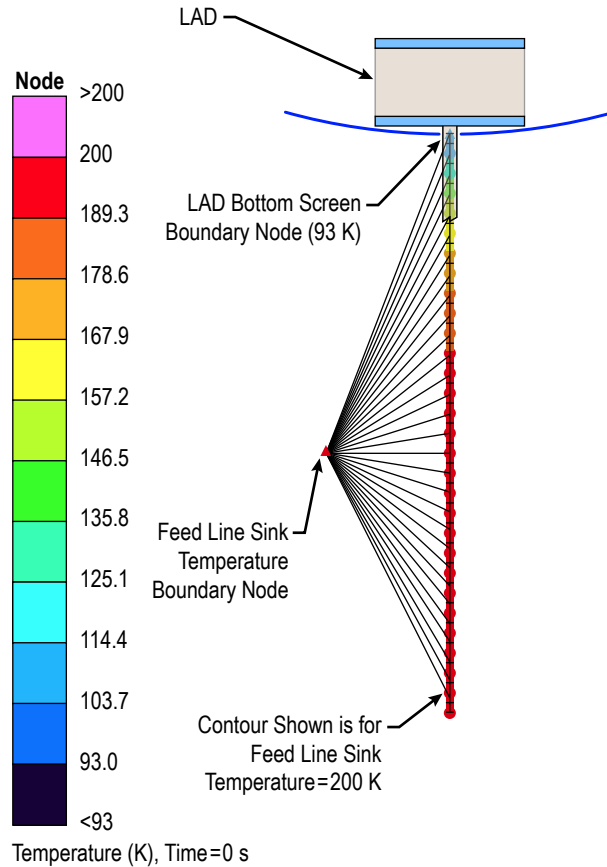
Figure 5. Feed line model to determine thermal coupling between the LAD
and the environment.

The increase in bulk LAD LCH$_4$ temperatures are shown against elapsed time on the lunar surface (fig. 8). The dashed lines represent the tank bulk fluid temperature whereas the solid lines represent the LAD. For a feed line sink temperature of 190 K and an LCH$_4$ starting temperature of 103 K, the LAD bulk temperatures remain below the vaporization limit (111.7 K) at 101.4 kPa (14.7 psia).

The bulk LAD LCH$_4$ temperatures are shown parametrically against the feed line sink temperature after a 210-day stay on the lunar surface (fig. 9). The dashed lines represent the tank bulk fluid temperature whereas the solid lines represent the LAD. Even with a feed line sink temperature of 230 K and an LCH$_4$ starting temperature of 103 K, the LAD bulk temperatures only approach the vaporization limit of 111.7 K at 101.4 kPa (14.7psia) after 210 days.

The initial efforts to model fluid motion due to natural convection inside the LAD start basket used heated/cooled flat-plate empirical data to represent convective heat transfer coefficients. However, application of the available empirical data to the problem left much to be desired. Therefore, it was decided that the natural convection would be better represented by using COMSOL, a commercially available program, to perform two-dimensional axisymmetric modeling. The enhanced resolution of the two-dimensional axisymmetric plane revealed a complex transient
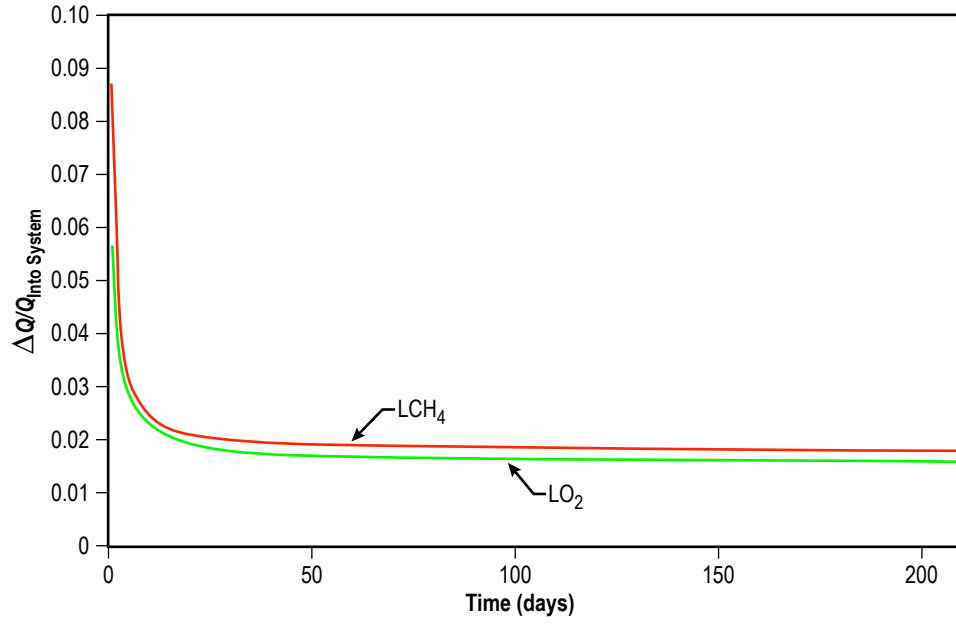
Figure 6. Heat entrapment shown as energy accumulated in relation to total energy into LAD.
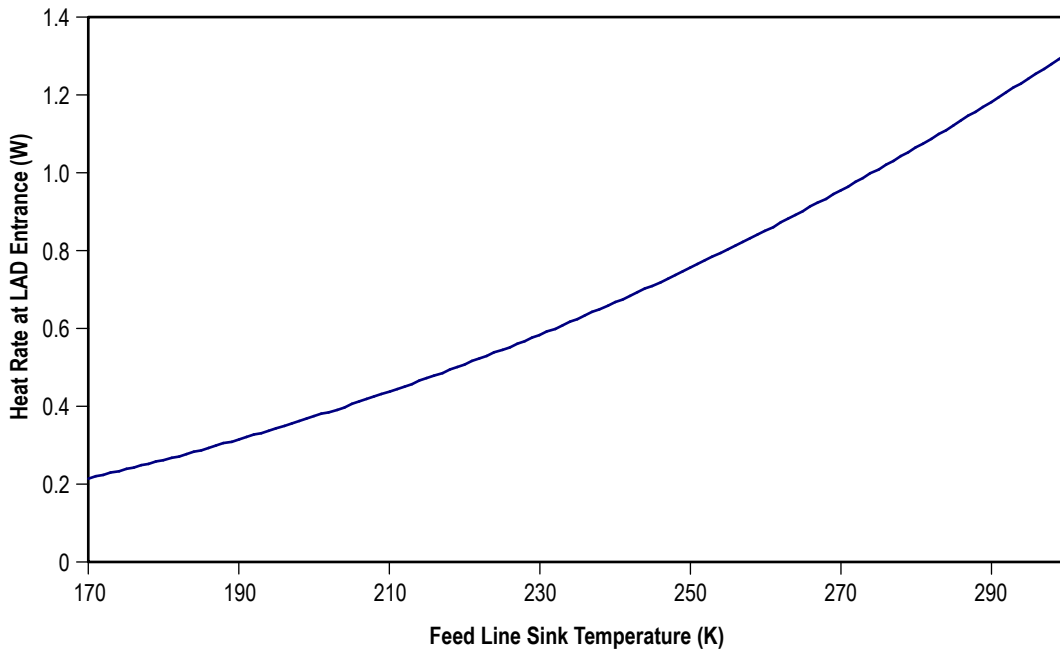
Figure 7. Heat rate versus feed line sink temperature.
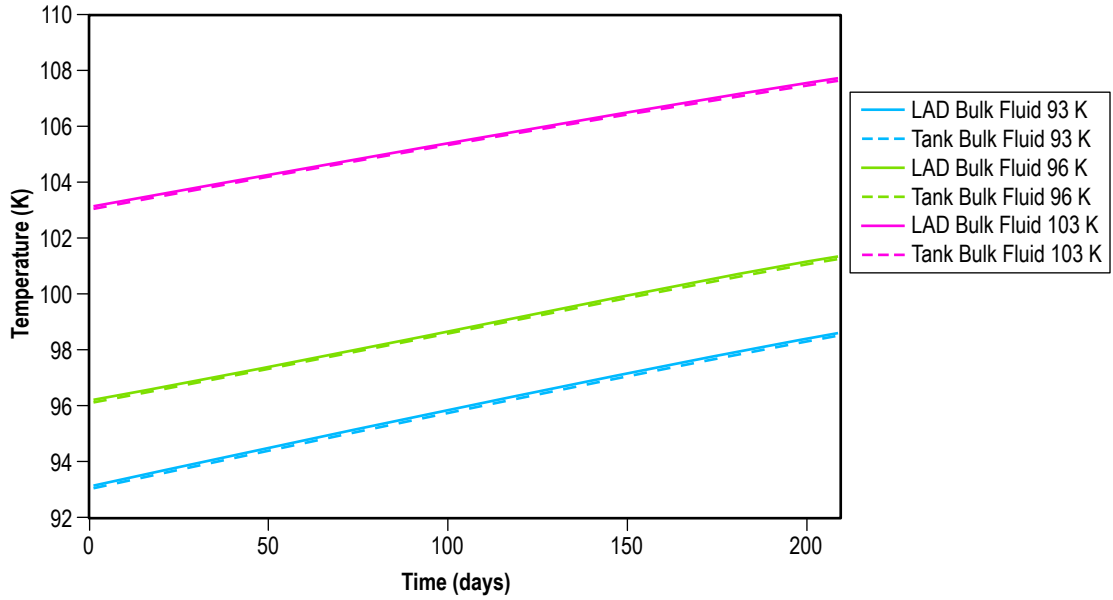
Figure 8. LCH$_4$ transient temperatures versus time for a feed line sink temperature of 190 K.
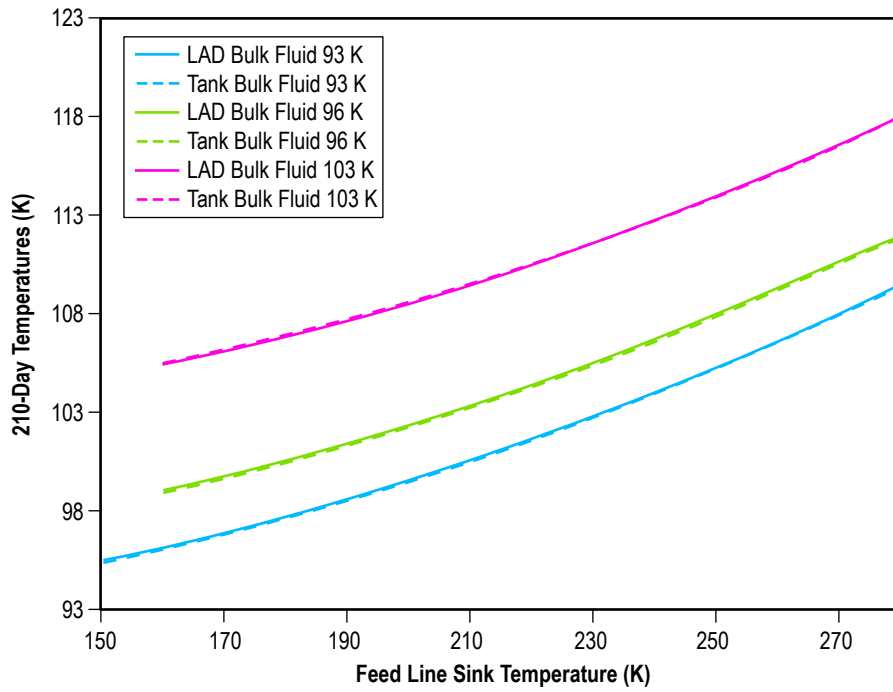
Figure 9. LCH$_4$ 210-day temperatures versus feed line sink temperature.

flow field (fig. 10). The two-dimensional simulations indicated that the convective heat transfer coefficient between the top and bottom plates of the LAD may be somewhat lower than that predicted by empirical flat plate relations used in the previous modeling effort. However, limitations in capturing the true physics of the problem led to the development of full three-dimensional simulations described in section 3.2.
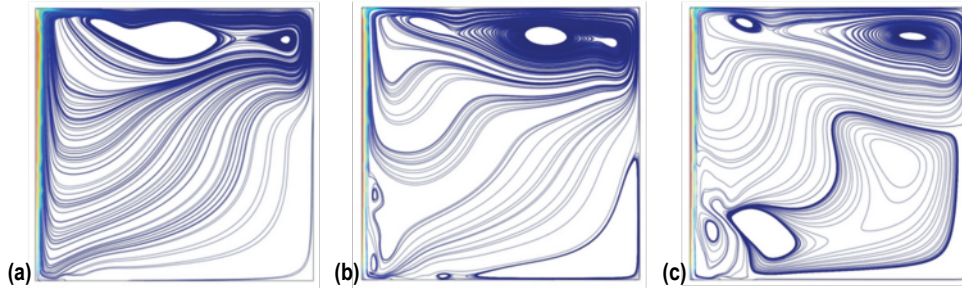
Figure 10.   Transient free convection in an annular cavity feed line $Q = 0.5$ W, flow streamlines, LCH_4 propellant: (a) 60 s, (b) 90 s, and (c) 120 s.

3.2 Refined Thermal Modeling: Flight System

As discussed earlier, a more refined analysis was necessary to model natural convection within the LAD, especially the LAD channels, at 1/6 g. Therefore, the development of a three-dimensional CFD COMSOL model of the LAD internal volume was initiated. This model used the incompressible Navier-Stokes flow module coupled with the conduction and convection module. The Boussinesq approximation is employed via a small modification to the COMSOL body force terms in the flow module. Transient simulations are used because the free convective flow inside the LAD is inherently unsteady under most conditions. A quasi-steady state is achieved when the temperatures at the feed line connection stop changing within a prescribed tolerance. Making use of the axial symmetry of the LAD, a 90° pie slice section of the start basket was modeled (fig. 11). All analyses are performed with LCH_4 as the working fluid because similar modeling with LO_2 indicated no significant differences.

Coupled volumes representing the start basket volume and the manifold channels were also included in the model. This allowed for a simulation of the interaction between the buoyant flow in the main cavity and oscillatory flow in the channels.

Predictions for the transient start basket flow are performed parametrically over a range of gravitational accelerations and heat loads. Even under microgravity conditions, with a modest heat load of 0.1 W, a buoyant flow circulation is observed, although the temperature distribution still tended toward what would be observed in the case of pure conduction (fig. 12).

In a lunar gravitational field, with comparable or even lower heat loads, a chaotic turbulent flow is observed in the main cavity (fig. 13). At accelerations approaching lunar gravity, a chaotic flow is observed in the manifold whereas a laminar circulation is evident under microgravity conditions (fig. 14).
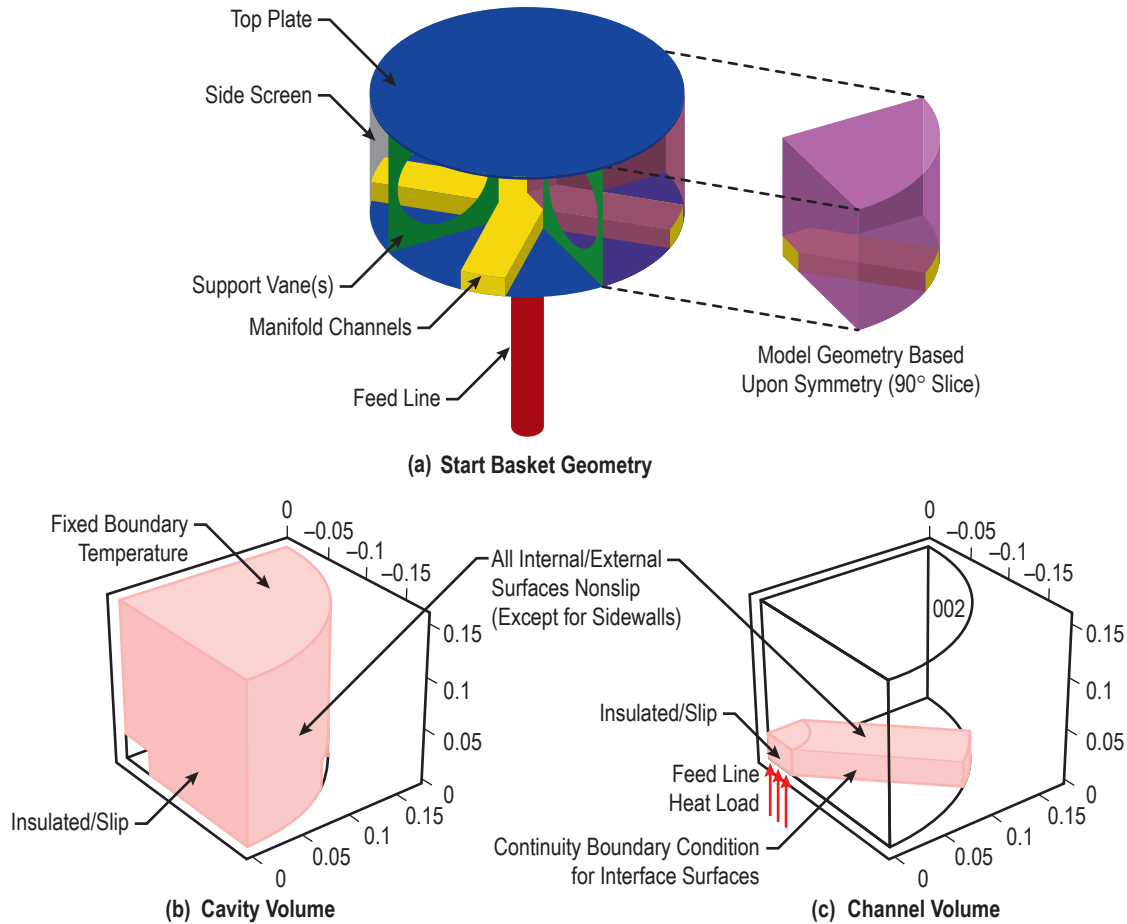
Figure 11. Geometry for three-dimensional CFD model and imposed boundary conditions: (a) Computational domain start basket geometry, (b) cavity volume, and (c) channel volume.

The impact of the LAD support structure in mitigating the top-to-bottom temperature gradient across the LAD is illustrated in figure 15. For the limiting conduction only case (i.e., largest gradient), the gradient is reduced by over 25% by including the 0.089-cm- (0.035-in-) thick stainless steel support structure.

The top-to-bottom temperature gradient across the LAD is shown parametrically versus heat leak in figure 16 for three scenarios: fluid conduction only, fluid conduction with structure, and natural convection. The impact of the LAD support structure in mitigating the top-to-bottom temperature gradient is readily apparent. Thickening the support structure showed a modest improvement. The fluid motion with natural convection greatly suppressed any thermal gradient (see dashed line).

This analysis indicates robust-free convection inside the start basket main cavity and manifold volume at low gravity with a small feed line heat leak. Free convective motion is even observable inside the start basket under microgravity conditions. In future efforts, it may be possible to integrate
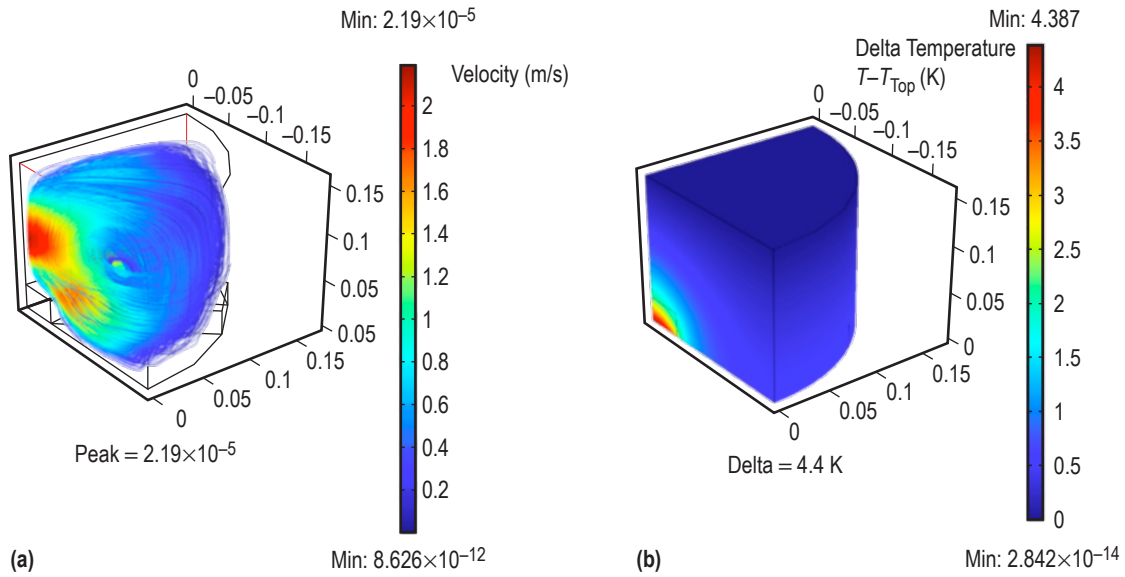
Figure 12. Computed velocity streamlines and temperature contours in microgravity: (a) Velocity streamlines, and (b) temperature contours ($g \sim 10^{-5}$ m/s^2) ($\approx 10^{-6} \, g_c$) and a heat load of $Q = 0.1$ W.
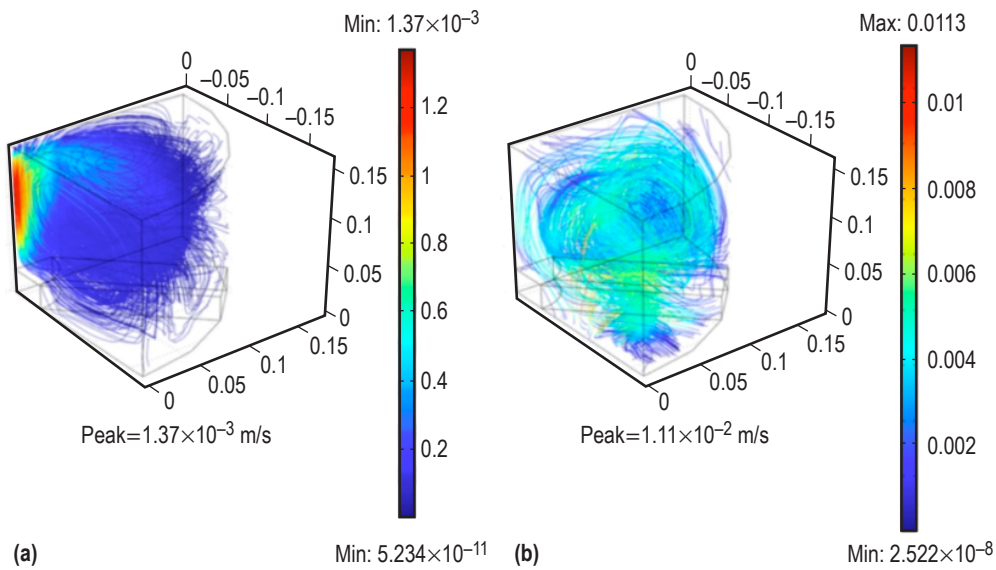
Figure 13. Velocity streamlines (m/s) for 0.16 g_c at (a) $Q = 0.01$ W and (b) $Q = 0.1$ W.
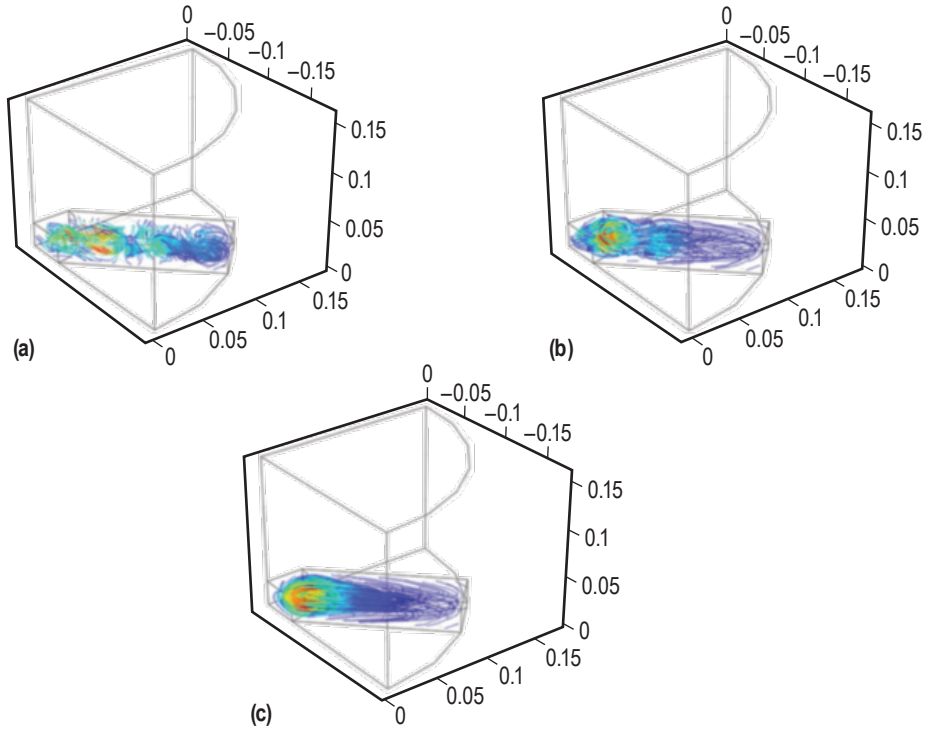
Figure 14. Velocity streamlines in LAD channel versus reduced gravity level: (a) $g=10^{-1}$ m/s^2, (b) $g=10^{-2}$ m/s^2, and (c) $g=10^{-5}$ m/s^2.

$\Delta T=4.2$ K $\Delta T=T_{max}-T_{min}$ $\Delta T=3$ K
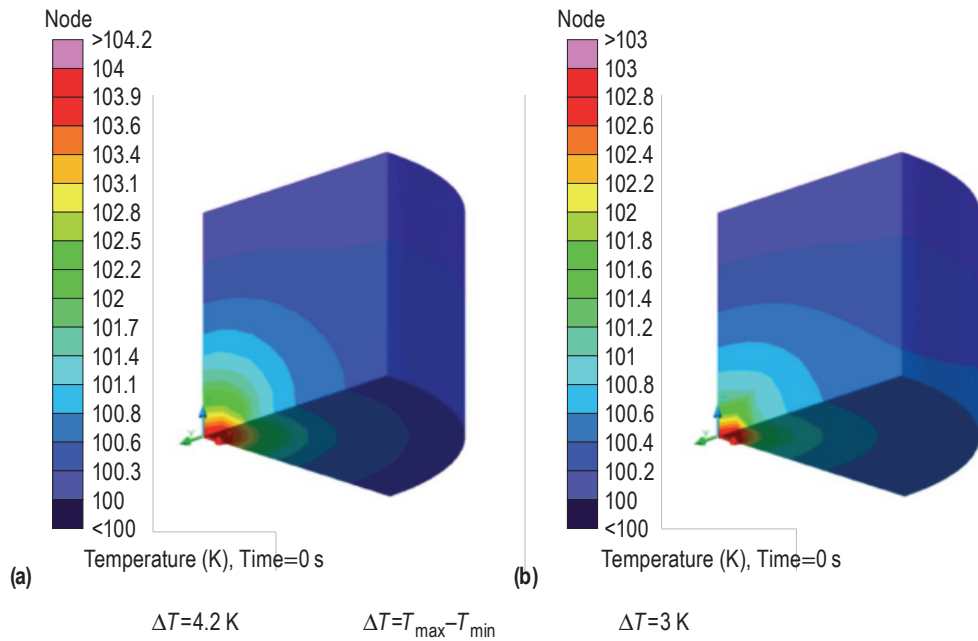
Figure 15. LAD fluid volume temperature profile: Conduction only, $Q=0.1$ W, LCH$_4$ at 95 K: (a) No support structure included and (b) with 0.035-in support structure.
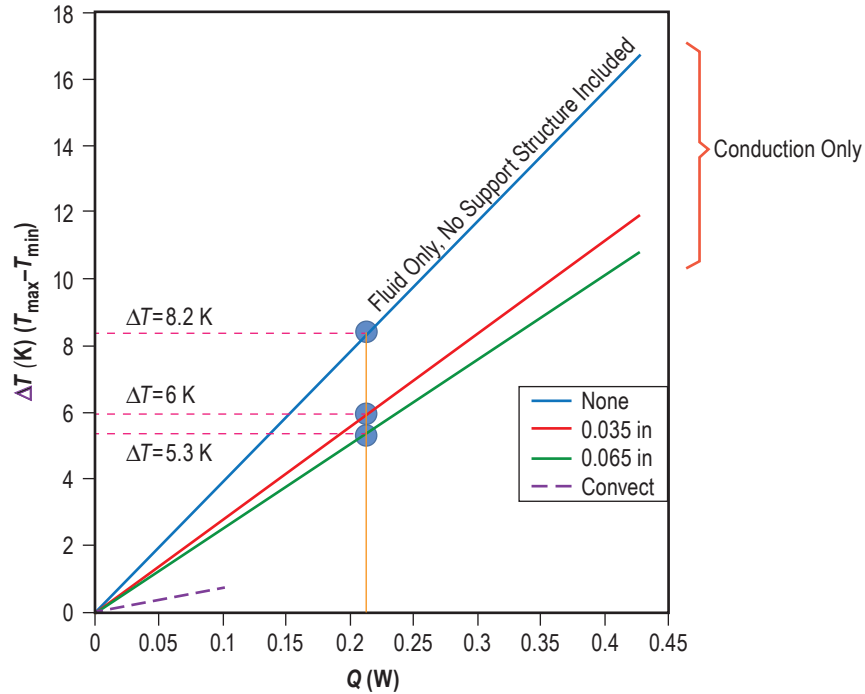
Figure 16. Parametric LAD change in temperature versus heat leak (LCH_4).

entire (thermal and fluid) analysis under COMSOL (depending upon the model size) to account for thermally conductive stainless steel support structure and mesh. Future activities will also include model correlations with test data from system integration testing with water (described in sec. 6).

3.3 COMSOL Thermal Modeling: System Testing With Water

COMSOL modeling of the LAD volume under terrestrial conditions with water as the working fluid showed that the flow can transition to turbulent conditions, even with only a relatively small input heat flux (fig. 17).

Numerical instability and unsteady flow, along with a transition to turbulence with sufficiently high feed line heat leaks, suggest implementing a Reynolds averaging approach with closure via a turbulence model. A two-equation, k-ε model within the COMSOL (in the multiphysics weakly compressible transport and nonisothermal flow modules) was integrated with the previous laminar model using a two-dimensional axisymmetric domain that included both the interior of the LAD and the tank.

Nonisothermal flow is modeled using a predefined coupling between the incompressible flow and the heat transfer modules in COMSOL: the Navier-Stokes equation in the laminar case, and a Reynolds averaged Navier-Stokes k-ε model in the turbulent case. The internal and external boundaries are treated as no-slip surfaces in the laminar case; the wall function method is used with turbulence. The body force terms in the equations of motion are modified using the Bousinnesq approximation. The external surface thermal boundary condition is represented by an effective heat
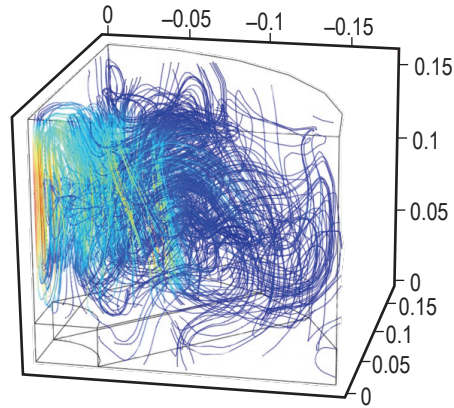
Figure 17. COMSOL modeled water velocity streamlines in LAD channel—Earth-based gravity, 293 K base temperature, 0.1 W heater input.

transfer coefficient, h_{wall}, that incorporates the effects of natural convection, and of Plexiglass™ (Rohmand Haas Company) and Styrofoam™ (Dow Chemical) thermal conductivities. The external boundary is represented by a effective film coefficient, $h_{wall} = 0.048$ W/m²·K, and temperature of 293.15 K. The LAD model assumptions are as follows: type 316 stainless steel, 1.65 mm thick, surrounded by an impermeable stainless steel mesh. The solution domain shown in figure 18 is based on
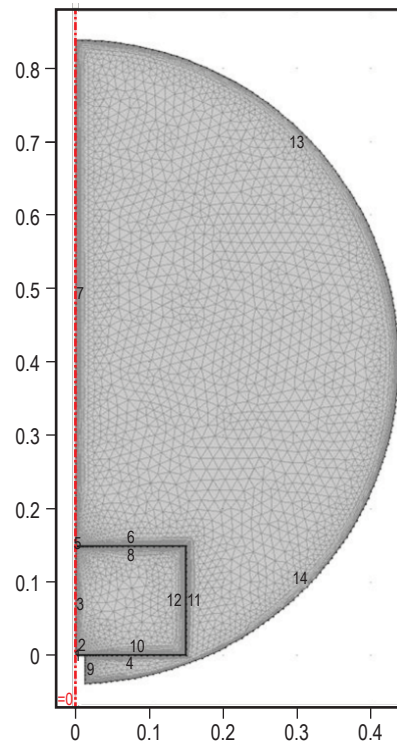
Figure 18. Two-dimensional axisymmetric model of the LAD/tank system: solution domain.

14,723 finite elements, 41,252 and 61,878 DOF for the laminar and turbulent cases, respectively. Transient simulations are used, as the free convective flow within the LAD is inherently unsteady under most conditions.

Detailed calculations were performed for the case of a constant heating power, $P_{heating} = 10$ W; the total simulated run time was 6,000 s. The temperature histories from thermocouple (TC) array F (a vertical array near the axis of symmetry and inside the LAD) are shown in figure 19; figure 19(a) shows the calculated temperatures using a laminar flow model, while figure 19(b) shows the temperatures using a turbulent flow model. Figure 19(c) shows the measured temperature data for a comparable experimental case with $P_{heating} = 9.4$ W (see sec. 6.4.1). The turbulent case yields better quantitative agreement with the data. The qualitative agreement is also better in that the modeled and measured axial temperature distributions both 'level out.' Color flood plots of the flow velocity and of the flow streamlines, for the same modeling conditions used to generate figure 19, are shown in figures 20 and 21, respectively.
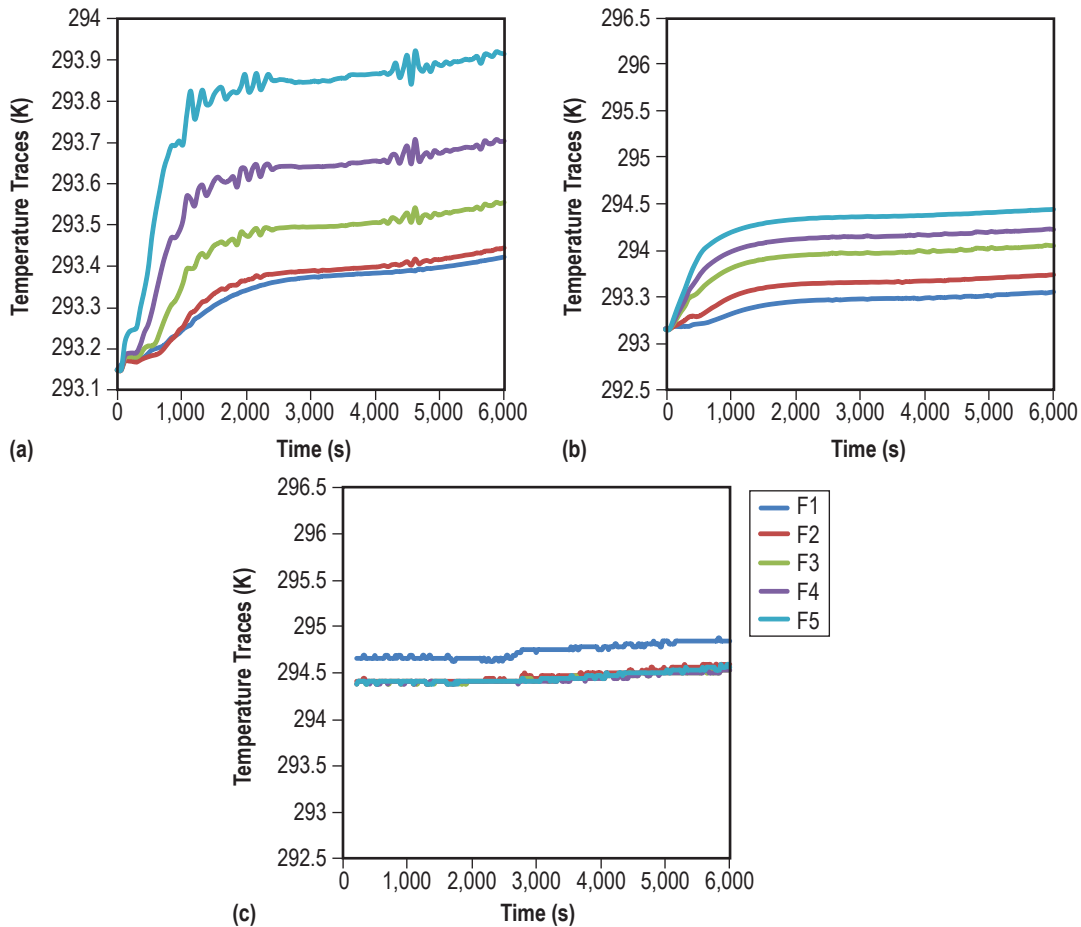
Figure 19. Measured and COMSOL computed temperature traces for the TC array F for the two-dimensional axisymmetric case: (a) Laminar flow model. computations, $P_{heating} = 10$ W, (b) turbulent flow model computations, $P_{heating} = 10$ W, and (c) measured temperatures, $P_{heating} = 9.4$ W.
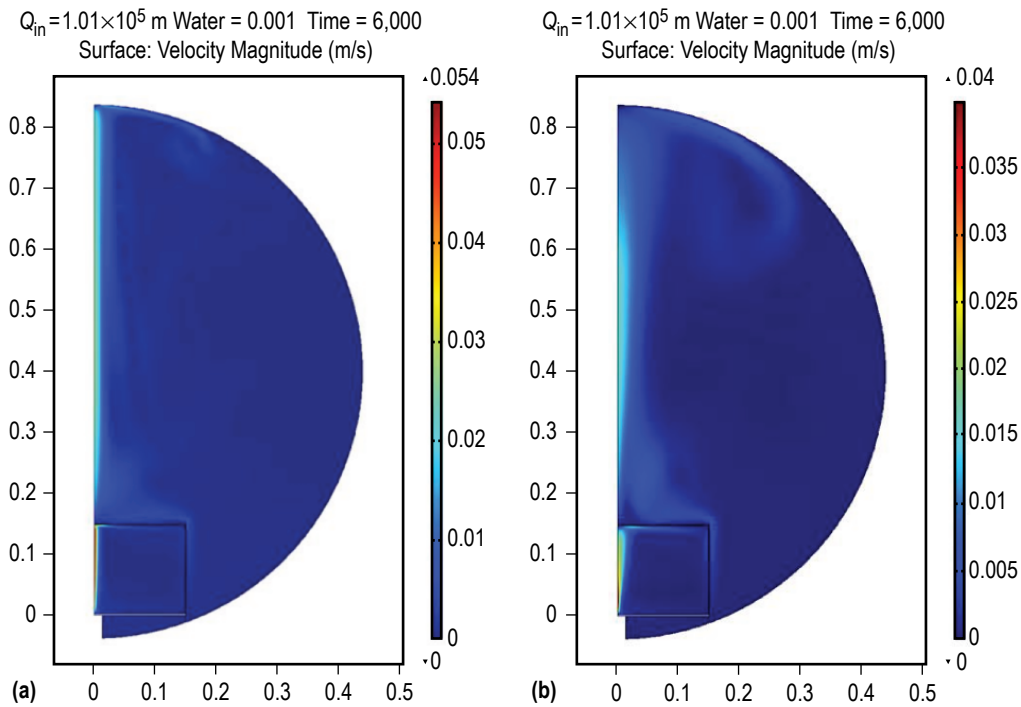
Figure 20. Flow velocities for the two-dimensional axisymmetric COMSOL calculation with a heating power of 10 W: (a) Laminar flow model and (b) turbulent flow model.
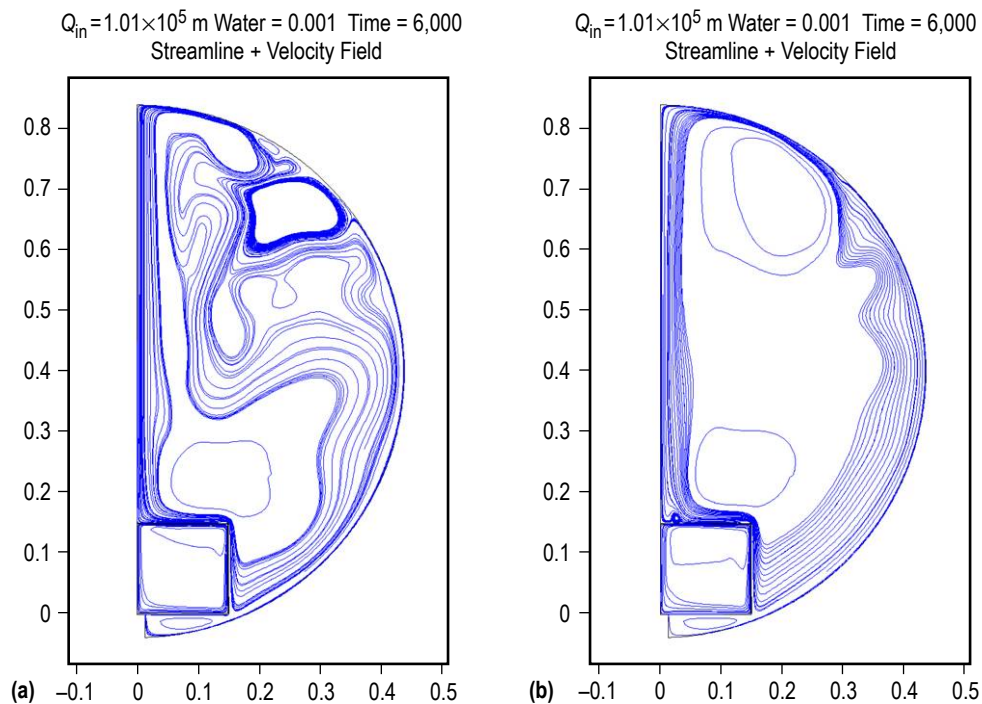
Figure 21. Flow streamlines for the two-dimensional axisymmetric COMSOL calculation with a heating power of 10 W: (a) Laminar flow model and (b) turbulent flow model.

17

As predicted by the turbulent calculations, the convective flow consists of a well-defined axial jet rising off of the LAD, with the fluid downfall occurring along the outer wall of the tank. The flow velocities at the locations of the probes in TC array H are shown in figure 22 for both the laminar and turbulent conditions. The laminar case overpredicts the axial flow velocities that were determined from the flow visualization measurements described in sec. 6.4.2. The turbulent calculations, however, show better quantitative agreement with the measured flow velocities.
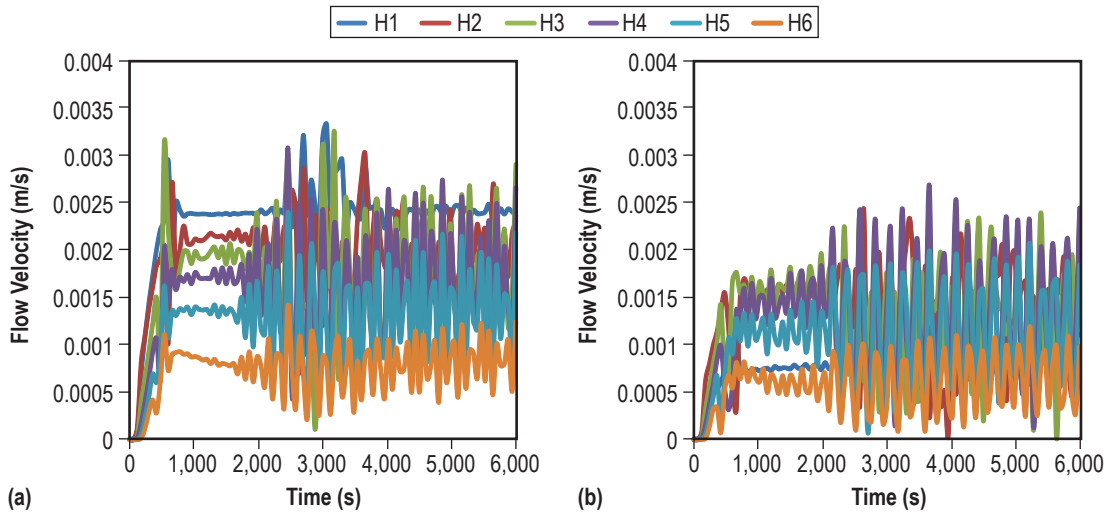
Figure 22. Calculated axial flow velocities for the two-dimensional axisymmetric COMSOL model at the probe locations of TC array H; $P_{heating} = 10$ W: (a) Laminar flow model and (b) turbulent flow model.

In summary, the model and test data correlation was not entirely conclusive. The modeled temperatures were not steady state, given the transient nature of the calculations. Also, the heat leak into the tank was uncertain. A more complete treatment would require additional cases to be run with additional values of input heating power inputs to better correlate the model with the test data. However, the flow velocities modeled and measured above the LAD as predicted by the model and as measured were of the same order of magnitude. Calculations with the turbulent flow model yielded better correlation with the test results than did those with the laminar model.

18

4. BULK FLUID COMPUTATIONAL FLUID DYNAMICS ANALYSES

The objective of this task was to investigate the bulk LCH_4/LAD interaction, thereby providing boundary conditions for the aforementioned LAD thermal model. These simulations were performed by Boeing with the CFD code FLOW-3D (written by Flow Science, Inc., Santa Fe, NM). This code has been used extensively to simulate a variety of cryogenic propellant systems and has been validated with data from the multipurpose hydrogen test bed (MHTB) and the solar thermal upper stage test demonstrator as well as against the Saturn S-IVB AS-203 flight experiment. At Boeing's request, Flow Science made a number of modifications to the code to better simulate cryogenic fluids, including the presence of a noncondensable gas (i.e., helium pressurant). By exercising or challenging the code with this task, a number of weaknesses were uncovered and corrected, thereby resulting in a more robust code for future applications. The baseline boundary conditions, CFD modeling description, and computational results are presented in the following sections.

4.1 Baseline Conditions

The NASA Marshall Space Flight Center- (MSFC-) specified LCH_4 tank problem included a spherical tank that was 1.04 m (3.4 ft) in diameter. As shown in figure 23, a cylindrical propellant management device (PMD) sits at the bottom of the tank with an axial jet thermodynamic vent system (TVS) mixer pump positioned on top. Heat leak enters the tank at different rates from discrete locations as indicated in figure 17. Total heat leak into the tank is 1.53 W (5.21 Btu/hr) during self-pressurization when the mixer is off. Distributed about the tank wall is a heat flow of 0.34 W (1.18 Btu/hr). Two tank structural attachments provide concentrated heating at 0.26 W (0.90 Btu/hr) each. The PMD heat leak varies depending on whether the mixer pump is operating. When the mixer is off, the heat leak from the combined PMD and mixer is 0.66 W (2.24 Btu/hr); when it is on, the mixer heat leak increases to 0.77 W (2.64 Btu/hr). The initial ullage gas fraction is specified as 2.1% of the tank volume. It contains a helium partial pressure of 1,828.5 kPa (265 psia) and a methane partial pressure of 110.4 kPa (16 psia) for a total initial tank pressure of 1,939 kPa (281 psia). Therefore, the liquid is initially saturated at 110.4 kPa (16 psia), which has a temperature of 112.71 K (202.88 R).

The requirements were to simulate the aforementioned described tank problem and provide at least four simulations with self-pressurization and mixing via the axial jet pump.

4.2 Baseline Computational Fluid Dynamics Model

The developed CFD model and computational grid are illustrated in figure 24, in which a total of 7,750 cells are used to resolve the tank geometry. As shown, the tank surfaces are divided into separate obstacles that permit application of discrete heat flow boundary conditions. Thus, the tank wall is divided into the straps and three wall sections. The axial jet pump is mounted atop the cylindrical PMD with the output source nestled at the top of a 2.54-cm (1-in) mixer outflow tube. Liquid enters the pump through the conical surface at the base of the pump and the models are operated with the inflow equal to the outflow so that the net mass in the tank remains constant.
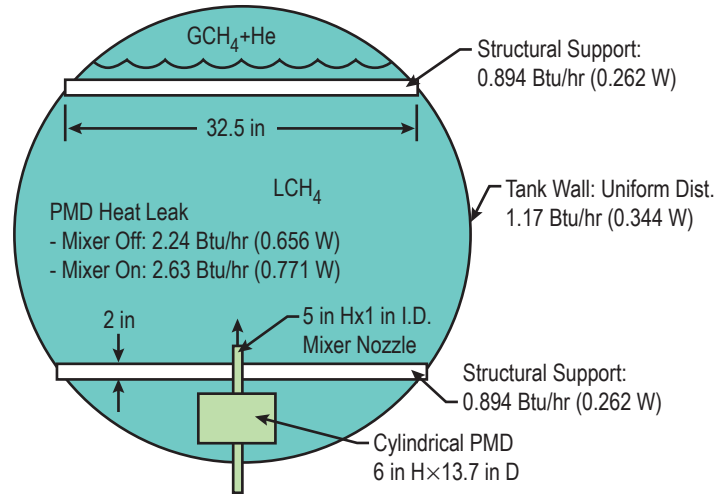
Figure 23. LCH$_4$ tank geometry and heat leak distribution.
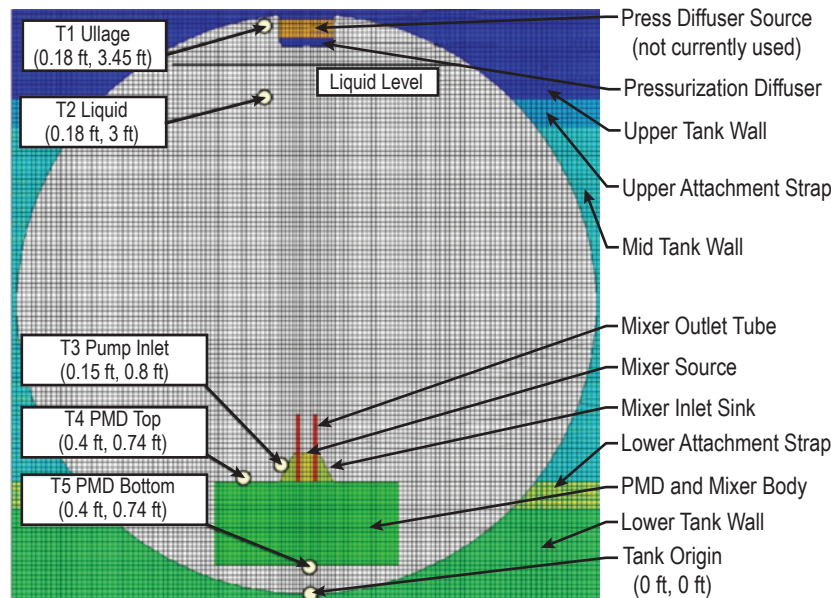
Figure 24. LCH$_4$ tank model.

A third mass source and obstacle is also included to represent the pressurization diffuser at the top of the tank. During initial condition development for the baseline problem, direct pressurization of the tank with helium was investigated and the helium entered the tank from this diffuser source. The direct injection method was not used in the final models presented here, rather the helium load was initialized at the beginning of the simulation. The diffuser, however, was retained in the simulation for potential future use. Numerical sensors were installed at the five locations shown in figure 24 for post-simulation analysis and discussion. All models reported temperature history data from these locations. Pressure data were taken from the T1 ullage sensor.

Assumptions in the FLOW-3D governing equations were consistent with the best practices developed during development. Model features included second-order momentum and energy equation approximations, discrete liquid-gas interface tracking, renormalized group theory turbulence, liquid density variation with temperature only, phase change (boiling and condensation), and liquid-gas wall heat transfer. Fluid viscosity, specific heat, expansion coefficient, latent heat, and speed of sound were all held constant in the model. Grid was selected based on resolutions used in MHTB validating cases. Each model operated by simulating the self-pressurization from heat addition and then, in selected cases, simulating the depressurization and thermal destratification during axial jet mixer operation.

4.3 Computational Fluid Dynamics Cases Evaluated and Results Summary

A total of 15 simulations were run with different initial bulk temperatures, and with and without TVS mixing. The assumed heat leak was a fixed 0.87 W through the walls and tank support rings, with a variable heat leak through the LAD of 0.15, 1.5, and 15 W. The tank was initially pressurized with 110 kPa (16 psia) of methane vapor and 1.83 mPa (265 psia) of helium gas for a total tank pressure of 1.94 mPa (281 psia), and simulations were run without mixing to determine the time elapsed until the ullage pressure rose by 34.5 kPa (5 psi), the assumed allowable pressure excursion range. These results are summarized in table 1.

Table 1. LCH$_4$ tank self-pressurization from 1.94 mPa (281 psia) as a function of LAD heat leak.

Case	LAD Heat Leak (W)	Pressure Rise (kPa)	Elapsed Time (hr)	Pressurization Rate (kPa/hr)
1	1.50	34.5	57.0	0.586
2	15.00	34.5	7.6	3.370
3	0.15	6.2	22.0	0.255

4.4 Pressure Reduction Results Summary

The 15 W LAD heat leak results are summarized in figure 25. The resulting curves show that, for a low enough flow rate (≈4 lpm or less) through the TVS, even with low outlet temperatures, the tank pressure does not decrease because the mixer plume stagnates before it can reach the surface and cool down the ullage.

4.5 Stratification Around Liquid Acquisition Devices

The heat leak into the tank through the LAD quickly established a buoyant plume with a radial temperature stratification. As warm fluid rose from the LAD and tank surfaces, the tank began to thermally stratify from top to bottom. For the tank pressure rise simulated, this vertical stratification was much greater than the thermal stratification from the submerged LAD. A layer of liquid, slightly warmer than the bulk liquid (by ≈0.02 K), surrounded the LAD (fig. 26), and this
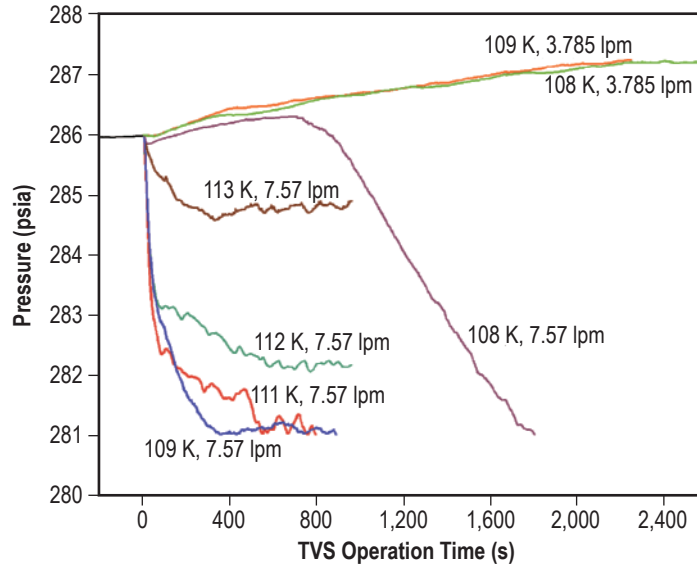
Figure 25. Pressure reduction rates with a LAD heat leak of 15 W versus assumed TVS flow rate and outlet temperature.
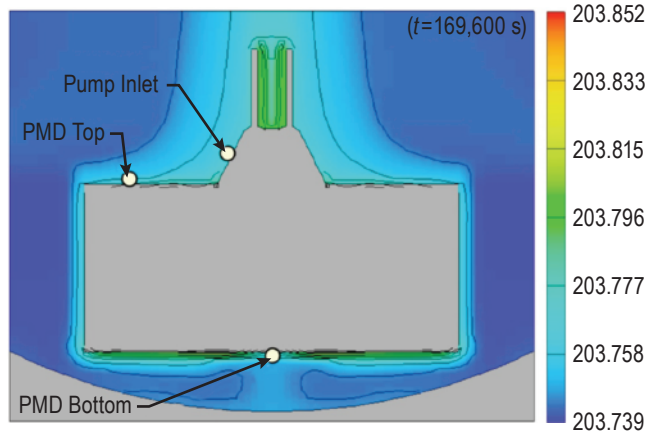
Figure 26. Temperature (K) distribution near the LAD during self-pressurization with a total heat leak into the tank of 1.5 W, of which approximately half is due to the LAD.

locally higher temperature should be accounted for in thermal models of the LAD. In particular, if warmer liquid accumulates below the LAD, a tapered LAD would allow this liquid to migrate away and reduce the trapped heat.

4.6 Detailed Modeling Examples

4.6.1 Self-Pressurization

The 15 cases completed produced reasonable results for the conditions simulated. Run times for the cases varied but the pressurization simulations required the most time to execute. Figure 27 indicates simulation run times on dual-core Intel Xeon 5160 3.0 GHz processor workstations with 3.5 GB of RAM.
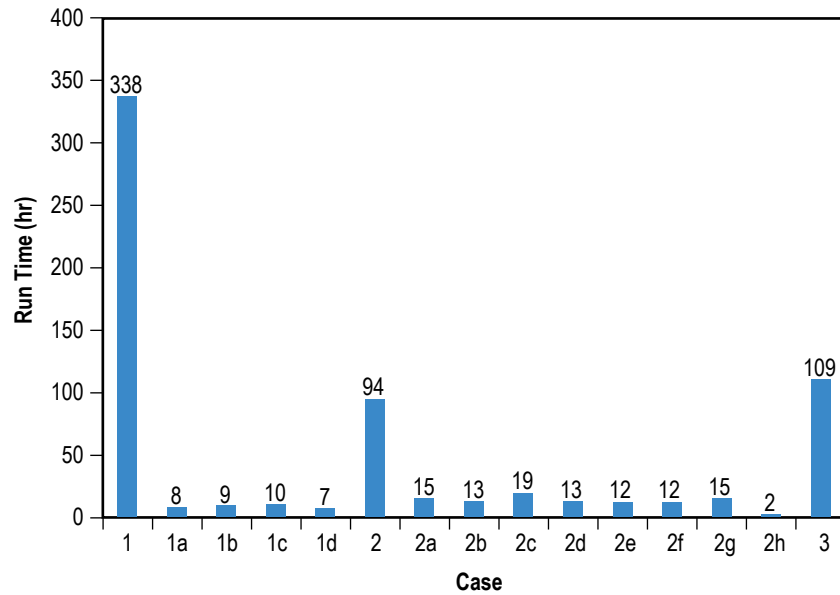
Figure 27. Model run time comparison.

Sample results are shown for case 1, in which the initially quiescent LCH_4 tank is heated at a rate of 1.5 W (5.13 Btu/hr) and allowed to self-pressurize by 34.5 kPa from 1.94 to 1.97 mPa (5 psi from 281 to 286 psia). Both the liquid and gas are initially of uniform temperature at 112.71 K (202.88 R). Figure 28 displays the predicted ullage pressure history when it was mainly linear with a steady self-pressurization rate of 0.473 kPa (0.07 psi/hr). To reach 1.97 mPa (286 psia), 69 hr are predicted by the CFD model. Fluid temperature histories are shown in figure 29 for the ullage at sensor T1, the liquid at sensor T2, and the liquid next to the pump inlet at T3 (fig. 18). The predicted ullage temperature was approximately 0.06 K (0.1 R) warmer than the liquid throughout the simulation. This was expected during self-pressurization, during which buoyancy causes the warmer, less dense fluid to collect at the top of an enclosure such as this tank. In case 1, the liquid temperature at the pump inlet is within 0.01 K (0.02 R) of the bulk liquid temperature as measured at T2. Both T2 and T3 increased with time as more energy flowed into the tank.

Temperature distributions versus time during a 34.5 kPa (5 psi) self-pressurization period with the 1.5 W LAD heat leak (case 1) are displayed in the series of contour plots in figure 30. After 100 s of heating, elevated temperatures were noticed emanating from the PMD and surrounding the
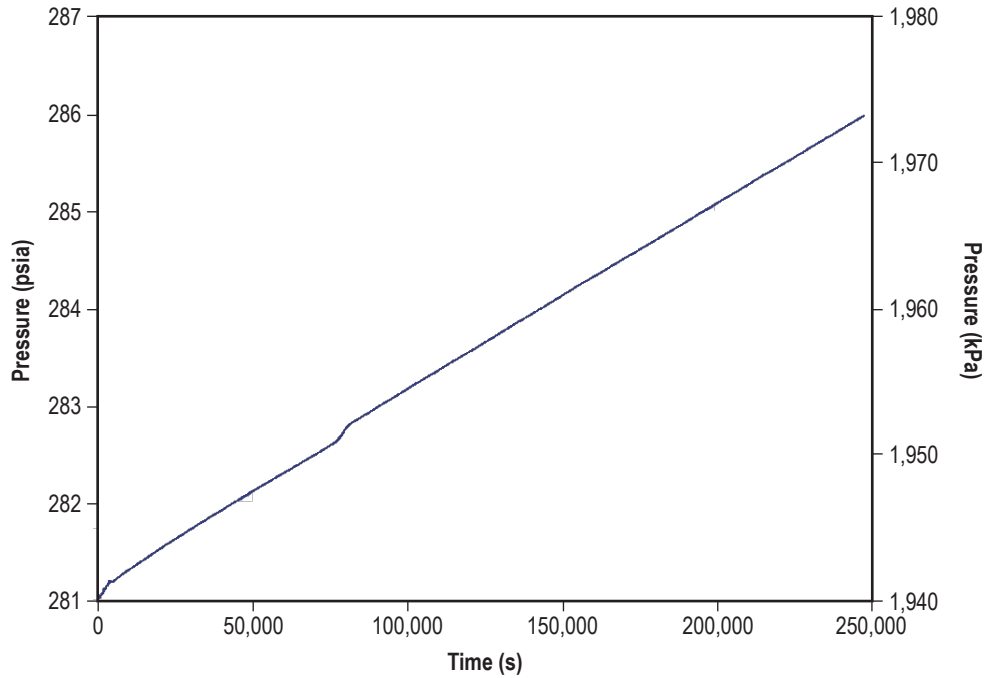
Figure 28. Case 1 ullage pressure history. Self-pressurization: LAD heat leak = 1.5 W or 5.13 Btu/hr.
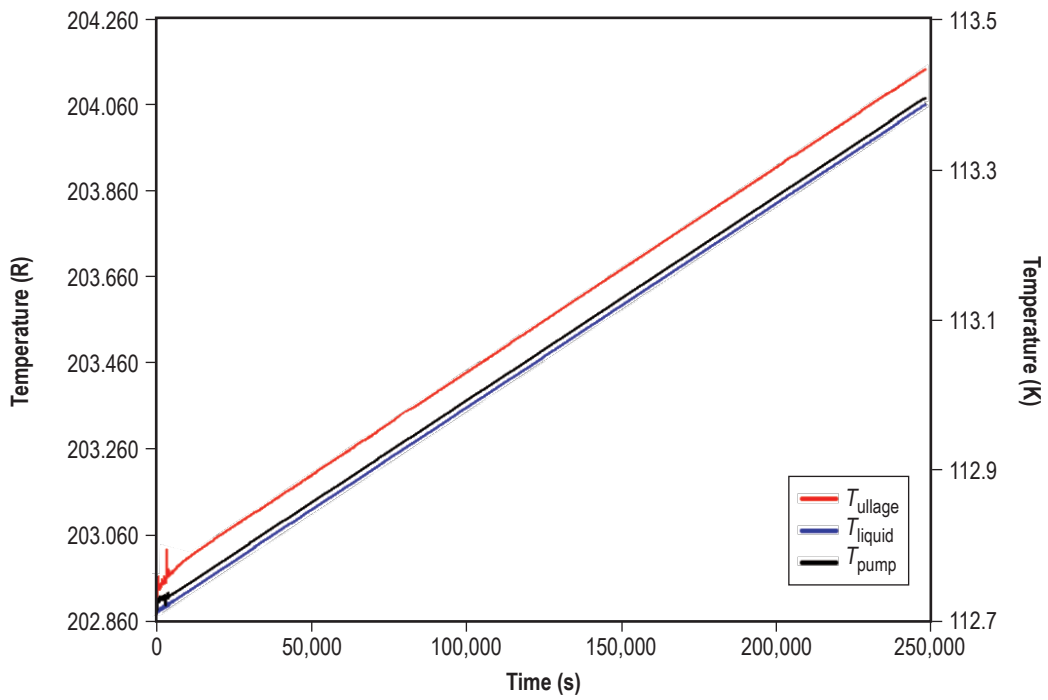
Figure 29. Case 1 fluid temperature histories. Self-pressurization: LAD heat leak = 1.5 W or 5.13 Btu/hr.
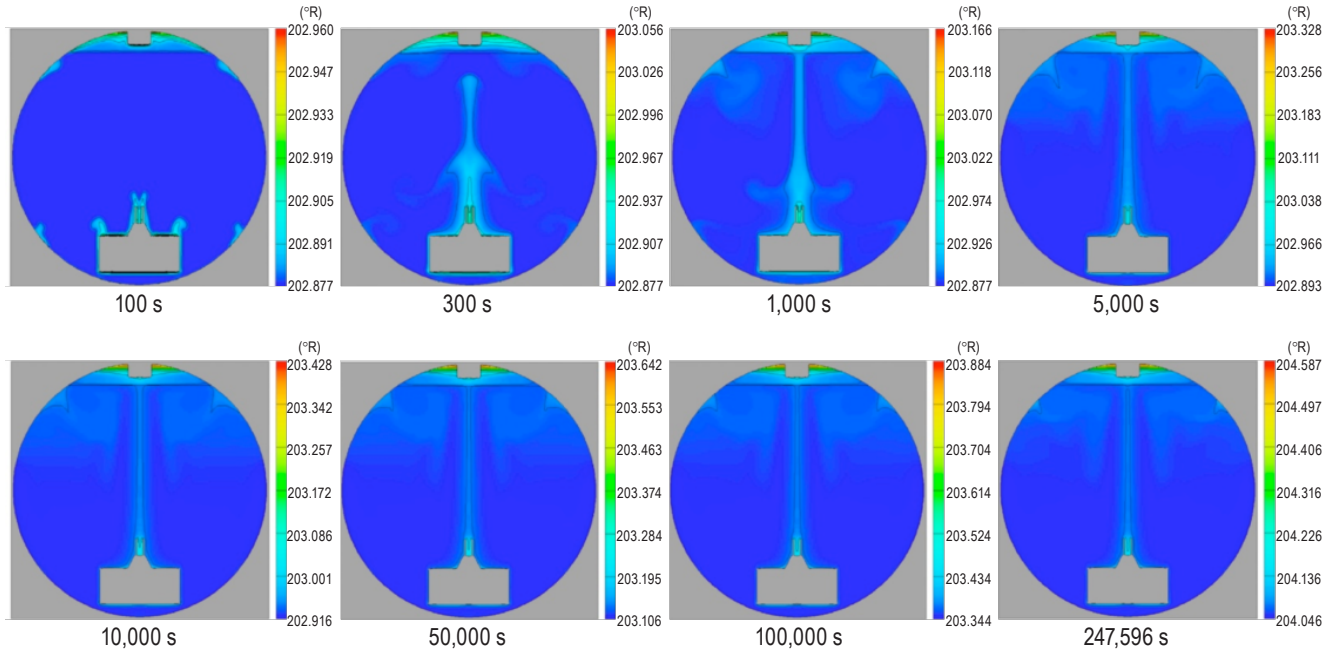
Figure 30. Case 1 temperature contour results (1.5 W or 5.13 Btu/hr self-pressurization).

structural mount locations. The ullage had already thermally stratified from its uniform initial temperature condition. By 300 s, a pronounced plume existed above the PMD as warmed liquid was pushed upward by buoyancy. For the same tank in the Earth's gravity, as opposed to the moon, the plume would be much stronger with larger velocities. From 300 s forward, the PMD plume retained its characteristic shape to the end of the simulation. At the end of the 34.5 kPa (5 psi) self-pressurization at 247,596 s or 69 hr, the LCH$_4$ tank was thermally stratified from top to bottom by 0.3 K (0.54 R) and was ready to be depressurized by the TVS mixer.

4.6.2 Mixing Results (Case 1c)

After 69 hr of slow pressurization and development of a 0.3 K (0.54 R) thermal stratification, the axial jet mixer was turned on in case 1c with 110.6 K (199 R) fluid provided by the TVS LCH$_4$ exits the mixer at 15.2 lpm (4 gpm), 110.6 K (199 R) and shot upward, impinging on the free surface and cooling the adjacent ullage gas. As the gas cooled, its density increases and the tank depressurizes. As shown in the pressure history case 1c in figure 31, the ullage pressure decreased by 24.8 kPa (3.6 psi) after operating the mixer for 60 s. After that initial pressure decrease, the depressurization rate slowed substantially, as indicated in the plot. Figure 32 graphs the fluid temperature histories at T1, T2, and T3 to represent the ullage, liquid, and pump inlet, respectively. The ullage temperature was predicted to decline rapidly as the cold axial jet impinged on the free surface and removed heat. Throughout the remainder of the simulated TVS and mixer operation, the ullage gas stayed colder than most of the liquid. The axial jet flow thus acted as a heat sink, constantly removing heat from the ullage at the liquid-gas interface. The pump inlet liquid temperature was predicted to be colder than that measured at T2 due to the cold downward-moving fluid from the axial jet as it operated.
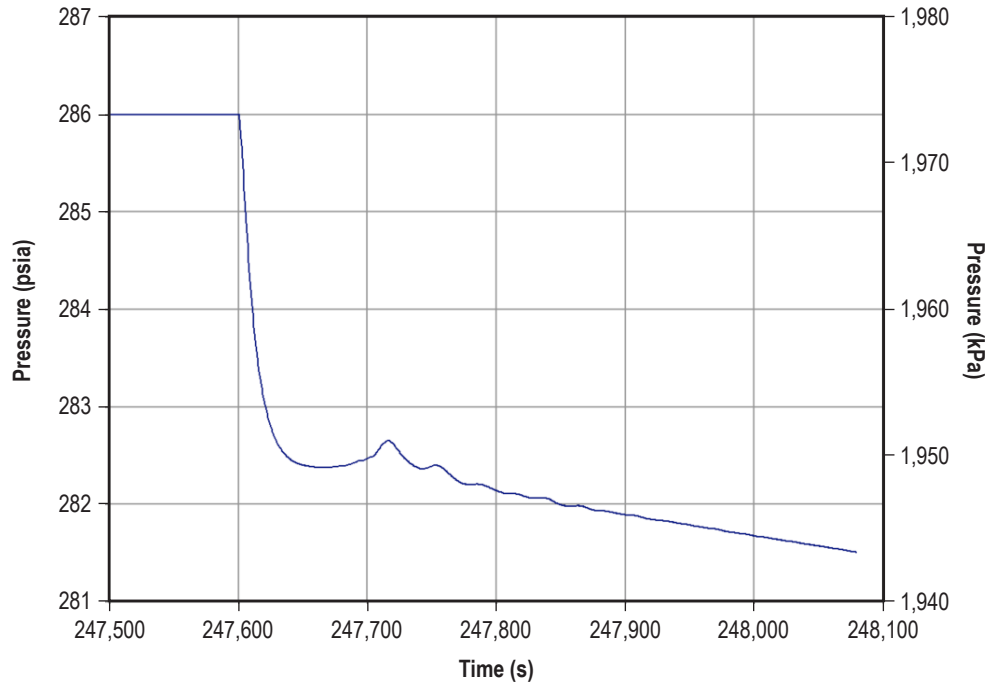
Figure 31. Case 1c ullage pressure history reduction with mixer operating at 110.6 K (199 R) and 15.2 lpm (4 gpm).
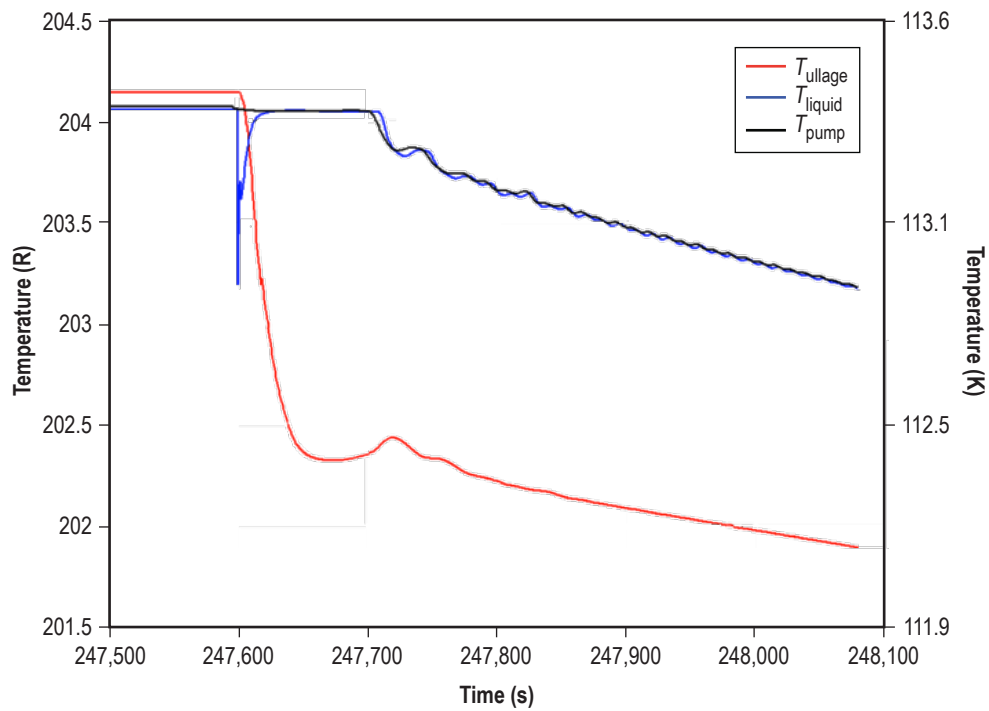
Figure 32. Case 1c fluid temperature reduction histories (110.6 K (199 R), 15.2 lpm (4 gpm)).

In the temperature contour plots in figure 33, the cooling effect of the TVS was observed at 247,596 s (or 69 hr) when the jet flow reached the liquid-gas interface and the ullage began to decrease its temperature. Some of the impinging fluid spread out over the free surface while some reversed direction and sank downward in a reverse shear layer surrounding the upward-moving jet flow. The temperature contour plot at 247,596 s in figure 33 displays this downward-moving reverse shear layer as it just reached the PMD. This illustrates how the pump inlet became cooler than the bulk liquid as some of its expelled liquid sank back downward toward the inlet. The horizontal spreading of the cooler jet flow was shown to curl under the free surface upon reaching the tank side walls at 247,596 s. This caused a second reverse shear layer as downward motion from the jet flow near the tank walls opposed the upward buoyant motion at the walls. Although the heat leak boundary condition used in the present analysis invariably transferred the specified energy into the fluid independent of local conditions, the interaction of the jet flow with the tank wall was expected to influence heat leak under actual conditions. This effect, along with the reduced buoyancy provided by the moon's gravity (1.63 m/s^2 (5.36 ft/s^2)), should be considered in any analysis using textbook heat transfer coefficients. In such complex fluid dynamic problems, the usefulness of accurate numerical simulation with CFD becomes apparent. By the end of the simulation, the maximum predicted gas temperature decreased from 113.66 K (204.59 R) to 113.09 K (203.57 R). This 0.57 K (1.02 R) reduction in the gas temperature increased the gas density enough for the tank ullage pressure to decrease by 24.84 kPa (3.6 psi) as shown earlier in figure 30.
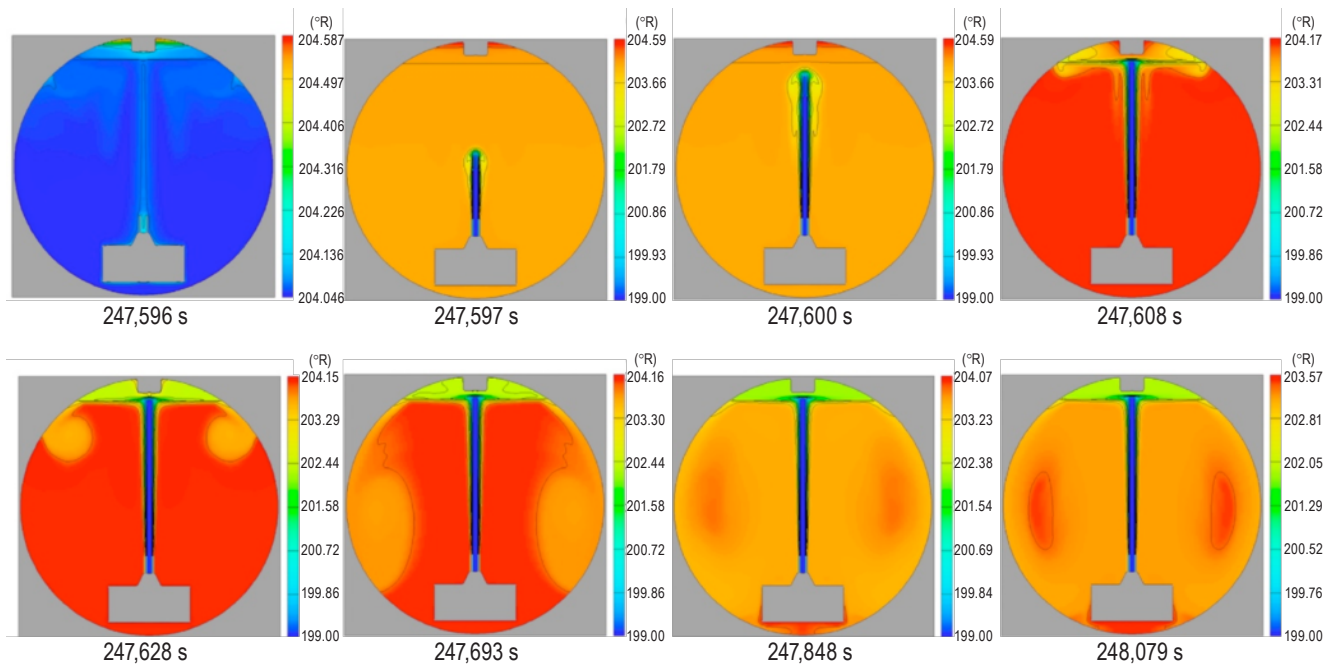
Figure 33. Case 1c temperature contour results (110.6 K (199 R), 15.2 lpm (4 gpm)).

4.7 Parametric Summary of Self-Pressurization and Reduction

By compiling all simulated results, obvious trends could be observed that indicated the tank behavior. As shown in figure 34, pressure rise rate increased as expected for increasing heat leak
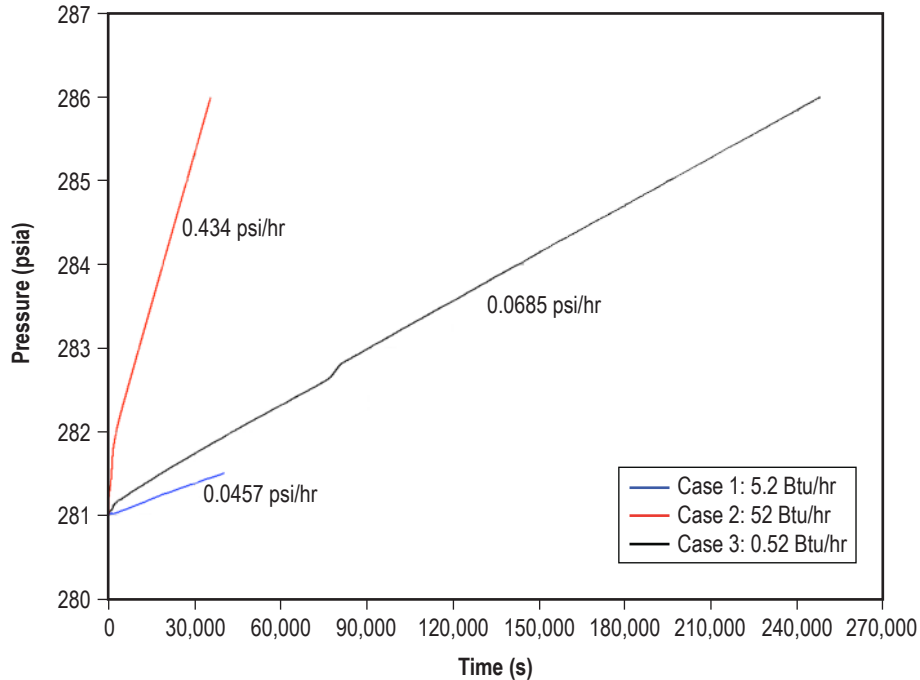
Figure 34. Self-pressurization versus tank heat leak.

boundary conditions. In figure 35, colder TVS fluid temperatures and higher mixer flow rates led to faster cooling and depressurization times. However, this trend did not continue for the 15.27 W/hr (52.2 Btu/hr) cases shown in figure 36. Here, it is shown that the TVS fluid temperature could become too cold for the selected flow rate. For example, the 110.6 K (199 R), 11.36 lpm (3 gpm) case did not reach the bottom of the pressure control band (1.94 mPa (281 psia)) and the tank began to repressurize after about 200 s of mixer use. In this particular case, the cold jet became submerged due to buoyancy differences between the jet and bulk fluid. When the flow rate was increased from 11.36 lpm (3 gpm) to 15.2 lpm (4 gpm) at this 110.6 K (199 R) temperature, the TVS and mixer performed better, as indicated by the lower tank pressure reached. It is important to understand fluid phenomena such as this for any hardware design, and the present CFD-based approach can, for a low cost, quickly identify such instances.

4.8 Bulk Fluid Computational Fluid Dynamics Analysis Conclusions

A warm layer of liquid, ≈0.06 K above the bulk propellant, could accumulate around the LAD exterior. When the mixer flow rate fell below 3.75 lpm (1 gpm), even with cool TVS outlet temperatures, the cool liquid fell to the tank bottom and the ullage pressure continued to rise. The FLOW-3D CFD program was substantially improved as a result of being challenged with the baseline thermodynamics. Several problems with the code were revealed and corrected as a consequence.
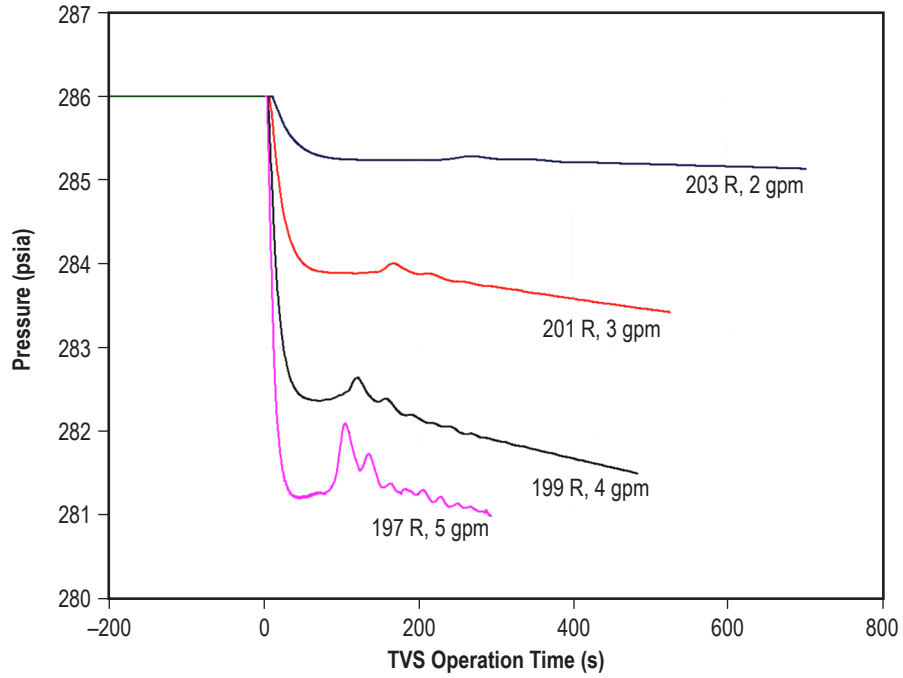
Figure 35. Ullage pressure reduction and TVS operating duration versus mixer flow rate and outlet temperature with 1.5 W heat leak.
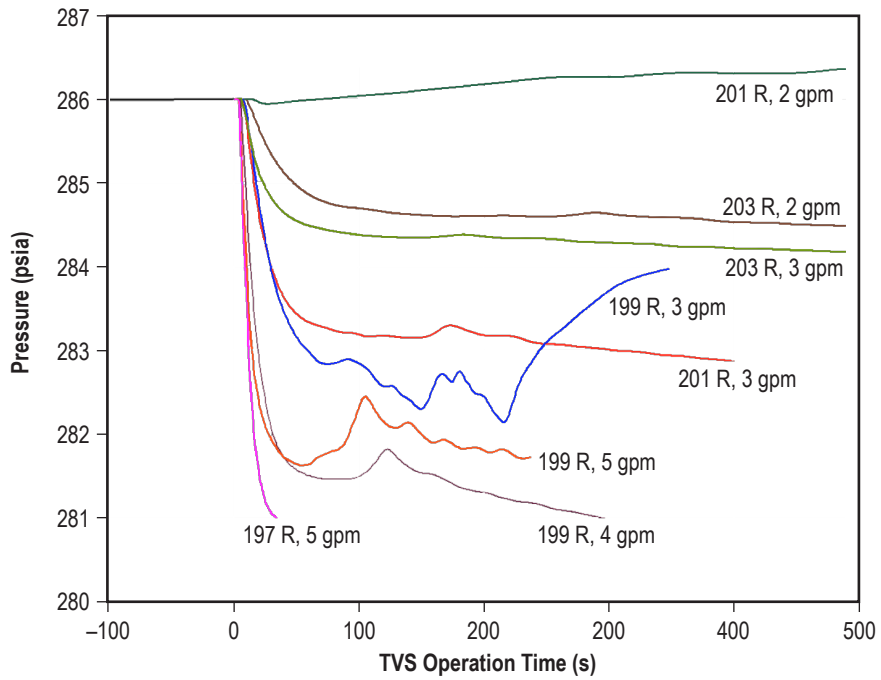
Figure 36. Ullage pressure reduction and TVS operating duration versus mixer flow rate and outlet temperature with 15 W heat leak.

5. LIQUID ACQUISITION DEVICE CONDENSATION CONDITIONING

As mentioned earlier, the objective of this program element was to explore the utilization of condensate conditioning to stabilize the retention characteristics of a LAD designed for cryogenic applications. The basic concept was to subcool the capillary screen surface in a manner that assured the accumulation of condensate, thereby replenishing the LAD contents and stabilizing the surface tension retention capability. Possible by-products included assisting with propellant transfer, LAD refill, and scavenging propellant vapors.

The condensate conditioning program consisted of the three programmatic phases shown in figure 37. The basic physics of liquid transfer and accumulation were demonstrated during phase 1 (FY 2008); screen wicking on small screen samples, first with alcohol, then with LN_2, during phase 2 (FY 2008, FY 2009); and then expanded screen conditioning and collection with larger, more complex screens during phase 3 (FY 2009, FY 2010). For this TP, the technical discussion has been divided into the four following subsections: condensate collection, alcohol wicking, LN_2 wicking, and condensate film flow analytical modeling.

Phase 1 (FY 2008)	Phase 2 (FY 2008, 2009)	Phase 3 (FY 2009, 2010)
• Concept Demonstration • Experiment Setup Precursor • Use Existing Equipment Insofar as Possible • Limited, if any, Quantative Data	• Procure More Suitable LN_2 Dewar, Camera, and Instrumentation • Implement Lessons Learned in Phase 1 • Interface With Small Screen Samples • Begin Film Flow/Screen Wicking Analytical and Experimental Evaluations	• Implement Phase 2 Lessons Learned • Interface With Larger, More Complex Shaped Screen • Expand Screen Conditioning and Collection Evaluation

Figure 37. LO_2/LCH_4 ascent stage LAD condensation conditioning program phases.

5.1 Condensate Collection

The first phase of the condensate collection program element was designed to achieve three goals: (1) Demonstrate the transfer of cryogenic liquid from one container to another against Earth's gravity, (2) acquire experience in photography and instrumentation for collecting cryogenic condensate, and (3) use low-cost and existing equipment to minimize funding requirements.

5.1.1 Condensate Collection Demonstration

The basic test concept (fig. 38) involved evaporation from a reservoir of liquid placed on the Dewar bottom and the condensation of vapors and liquid accumulation within a collector placed near the Dewar top. The instrumentation, component geometries, and materials are listed in table 2 and schematically represented in figure 39. Hardware pictures are presented in figures 40 and 41. The evaporator containing about 22.5 cm^3 of LN$_2$ was open at the top so that the evaporation vapors were free to migrate throughout the 0.08 m^3 Dewar internal volume at a temperature of 77.8 K. The vapors were then condensed on the copper condenser (surface area of about 84 cm^2). The condenser interior was maintained at a pressure of 75.8 kPa (11 psia) via the vacuum pump arrangement shown in figure 39, which sustained a subcooled temperature of 75.4 K on the condenser surface. The condensed liquid was then collected on a cone-shaped Teflon® (Dupont) surface and allowed to drip into the 29 cm^3 collector. The collected liquid was maintained in the liquid state by LN$_2$ circulation through coils wrapped around the collector exterior. The collector surface and coils were insulated to prevent condensation on the collector surface. Both the evaporator and collector were instrumented with liquid level sensors (silicon diodes), and the liquid condensation process was recorded by a video camera.
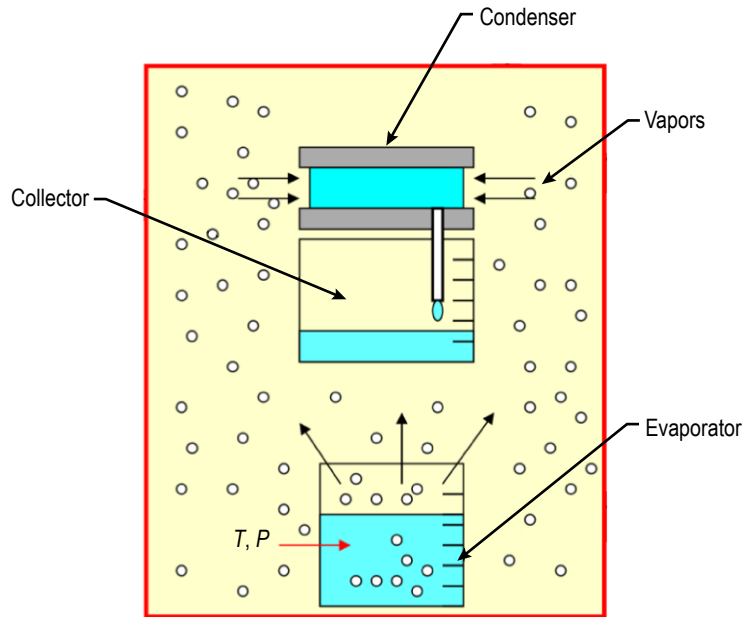
Figure 38. Approach to condensate collection demonstration.

5.1.2 Collection Demonstration Test Results

Test results are pictorially represented in figures 42 and 43, which show the condenser with liquid dripping into the collector. The test conditions are specified in table 3, and the test results are presented in figure 44.

Table 2. Condensate collection demonstration hardware geometry.

	Measurement
Condenser:	
Height	49.7 mm (1.96 in)
External diameter	53.8 mm (2.12 in)
Wall thickness	1.51 mm (0.059 in)
Material	Copper
Collector and evaporator:	
Collector height	126 mm (4.96 in)
Collector diameter	17.2 mm (0.67 in)
Evaporator height	128 mm (5.04 in)
Evaporator diameter	26.5 mm (1.04 in)
Cryostat:	
Internal height with fillers	522 mm (20.55 in)
Internal height without fillers	952 mm (37.48 in)
Internal diameter	328 mm (12.91 in)
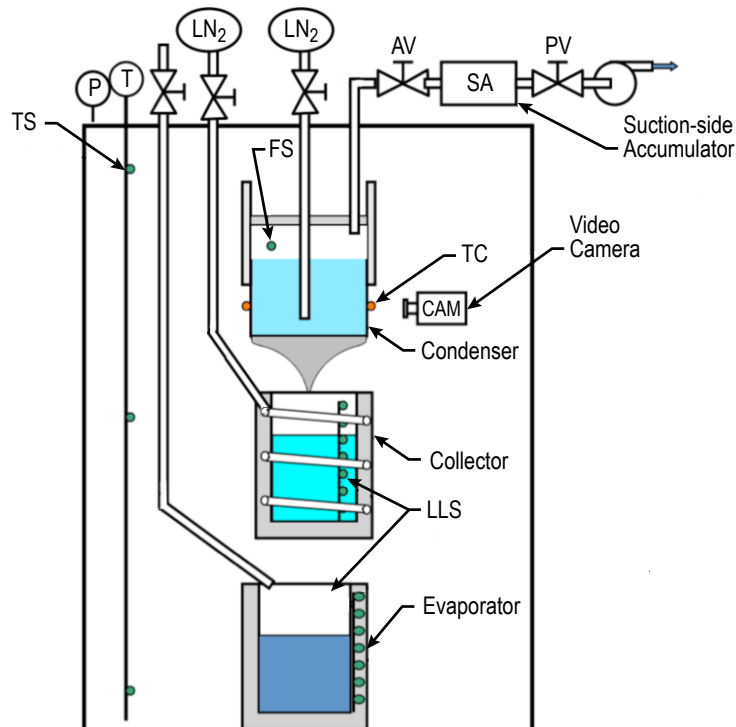
Figure 39. Demonstration test setup schematic (phase 1).
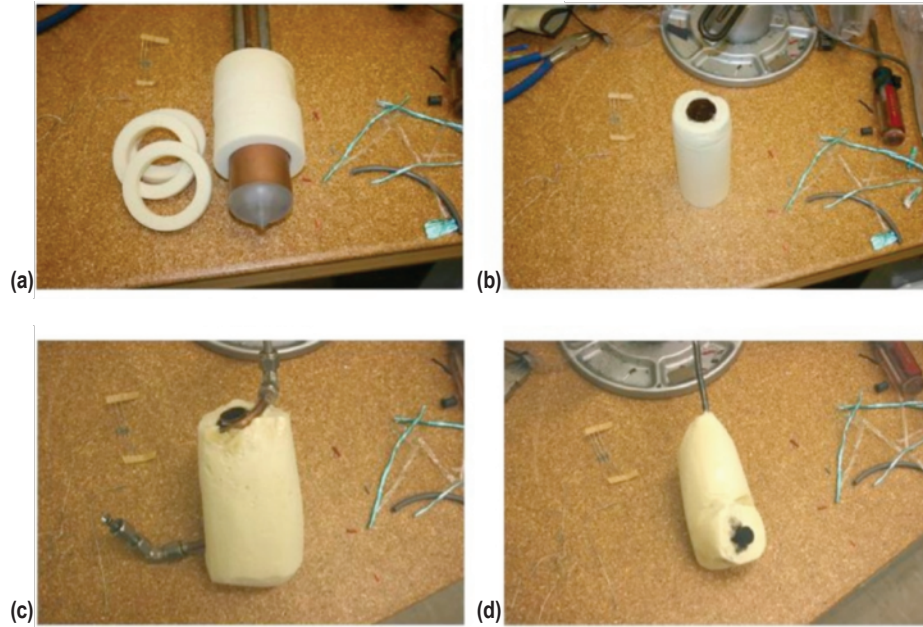
Figure 40. Hardware: (a) Condenser, (b) evaporator, (c) collector, and (d) camera.
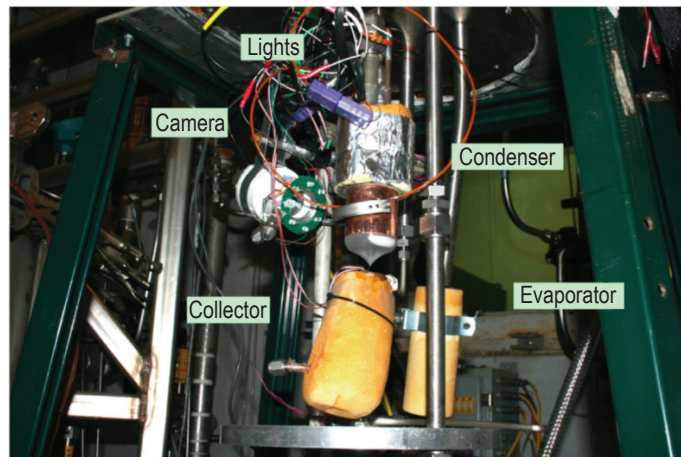
Figure 41. Condensation collection hardware prepared for Dewar placement.

5.1.3 Data Correlations

The analytical model (per W. Nusselt, 1916 and W.M. Rohsenow, 1956) used to evaluate the collection data is shown in figure 45.
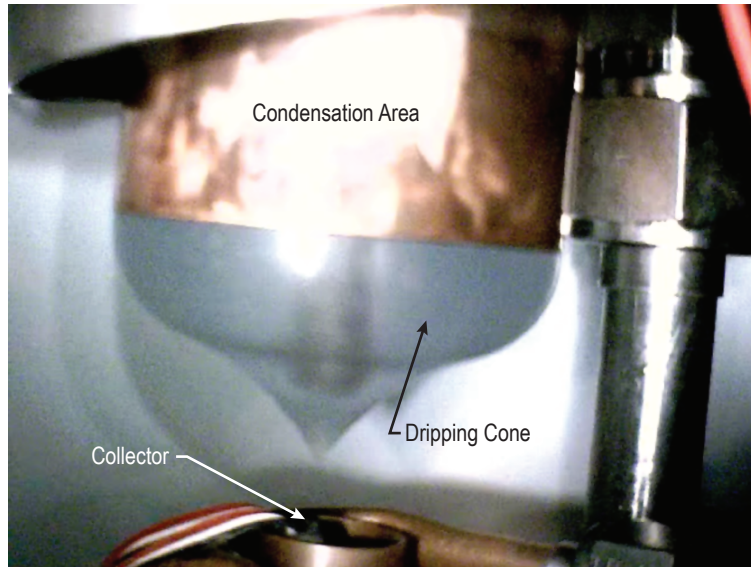
Figure 42. Camera view of the condensation collector.

Figure 43. Camera view of the condensation in action.

The assumptions/approach for the analytical correlation were as follows:

- The condensation mass flow rate (CMFR) was used for analytical/experimental comparison.

- Measured conditions inside the Dewar were used as inputs to the Nusselt model on the computed CMFR $= 0.2125$ g/s (0.00253 g/s·cm^2).

Table 3. Condensation collection test conditions.

	Measurement
Condenser:	
Internal pressure	7.58×10^4 Pa (11 psia)
Internal temperature	73.5 K
Surface temperature	75.4 K (calculated)
Cryostat:	
Internal pressure	1.05×10^5 Pa (15.2 psia)
Internal temperature	95 K (on the collector level)
Saturation temperature	77.8 K
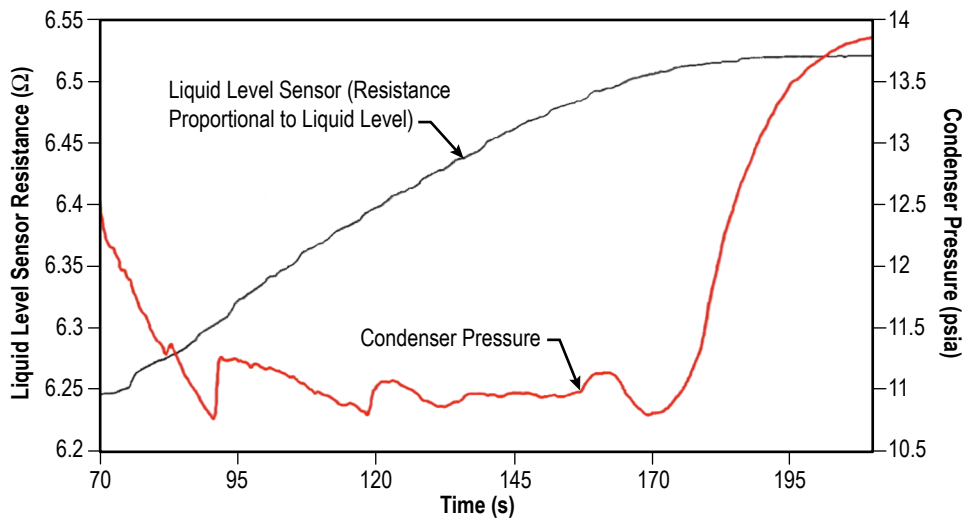
Figure 44. Test records example: condenser pressure and collector liquid level.

- The collector level sensor (electrical resistance versus liquid level) was calibrated to enable experimental condensed mass versus time.

- The measured collection rate was represented by linear function with slope equal to 0.1441 or 0.1441 g/s (0.00176 g/s·cm^2).

    The application of the these assumptions resulted in a CMFR about 32% above the measured rate (fig. 46). However, that was considered very reasonable given that the experiment setup was not designed to obtain quantitative data, i.e., it used low cost and existing hardware, the Dewar environment was not well controlled (Dewar too large), and simplified analytical modeling assumptions were used.
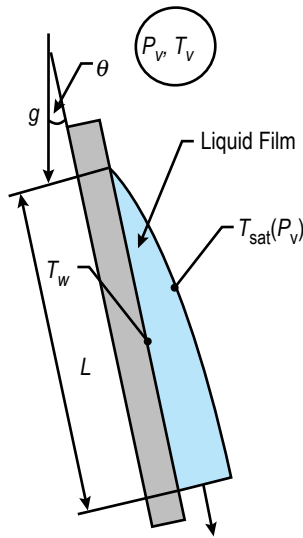
$$\bar{h}_L = 0.943 \left(\frac{g \cos\theta \rho_l (\rho_l - \rho_v) k_l^3 h'_{fg}}{L \mu_l (T_{sat} - T_w)} \right)^{1/4} \Rightarrow \text{Average Heat Transfer Coefficient}$$

$$Ja = \frac{C_{pl}(T_{sat} - T_w)}{h_{fg}} \Rightarrow \text{Jacob Number}$$

$$h'_{fg} = h_{fg}\left(1 + \frac{3}{8}Ja\right) \Rightarrow \text{Adjusted Latent Heat}$$

$$\dot{m} = \frac{\bar{h}_L A(T_{sat} - T_w)}{h'_{fg}} \Rightarrow \text{Mass Condensation Rate}$$

$$\dot{q} = \bar{h}_L A(T_{sat} - T_w) \Rightarrow \text{Total Heat Transfer to the Surface}$$

Figure 45. Analytical model data.
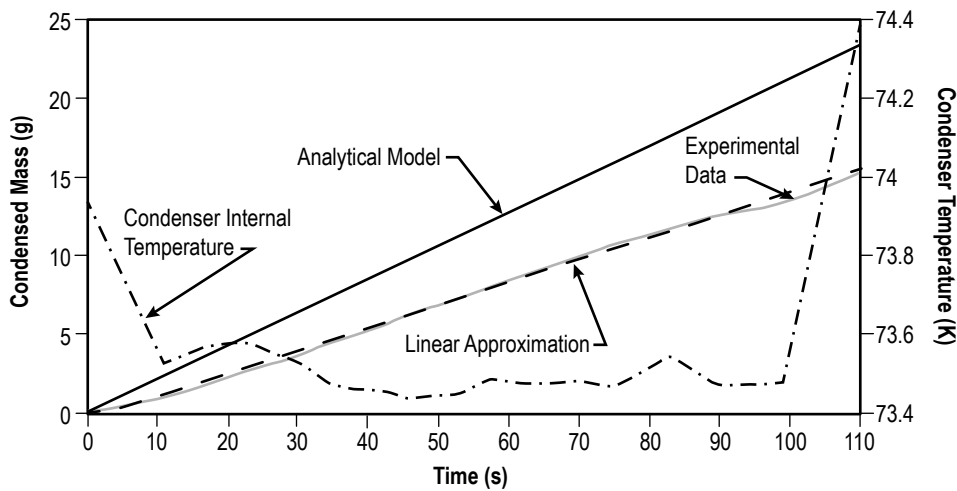
Figure 46. Condensation accumulation: test versus analytical correlation.

5.1.4 Conclusions and Lessons Learned

The three program goals previously specified in section 5.1 were achieved. Several conclusions and lessons learned were drawn. Regarding the instrumentation and controls, the silicon diodes were fragile and unstable and are not amenable to hardware adjustments; therefore, TCs may be a future solution. Also, more precise liquid level sensing is required. In addition, the Dewar is too large and the interior environment is unmanageable. A smaller, more specialized container is needed for stabilizing the temperature, pressure, and heat leak. Finally, the low-cost digital camera was able to pictorially record the physical processes in low temperature environments (LN$_2$), but a higher quality camera is needed for future tests.

Phase 1 testing demonstrated basic physics and the transfer of liquid cryogen against gravity. Valuable experience was acquired that guided the setup for phase 2. Though limited quantitative data were obtained, overall phase 1 testing was very encouraging.

5.2 Alcohol Wicking Tests

Once the condensation process was demonstrated, attention turned toward distribution of the collected liquid via wicking on the capillary screen surfaces, thereby assuring stable and predictable surface tension retention capability. Therefore, the objective of this element was to perform both vertical and horizontal screen wicking tests and to anchor the analytical modeling. Test and analytical modeling results are described below, beginning with the vertical tests.

5.2.1 Vertical Wicking Tests

The vertical screen wicking tests were conducted with 165×800, $200 \times 1,400$, $325 \times 2,300$, and $400 \times 2,800$ mesh screens. The test setup, depicted in figures 47 and 48, consisted of a vertical linear scale (ruler) positioned within a framework that provided a stable platform within which the screen sample could be interfaced with a small reservoir for the test liquid. A video camera was initiated upon filling the reservoir and the wicking characteristics were pictorially recorded. Room temperatures were recorded to monitor and compensate for any effects of ambient room temperature on fluid wicking behavior.
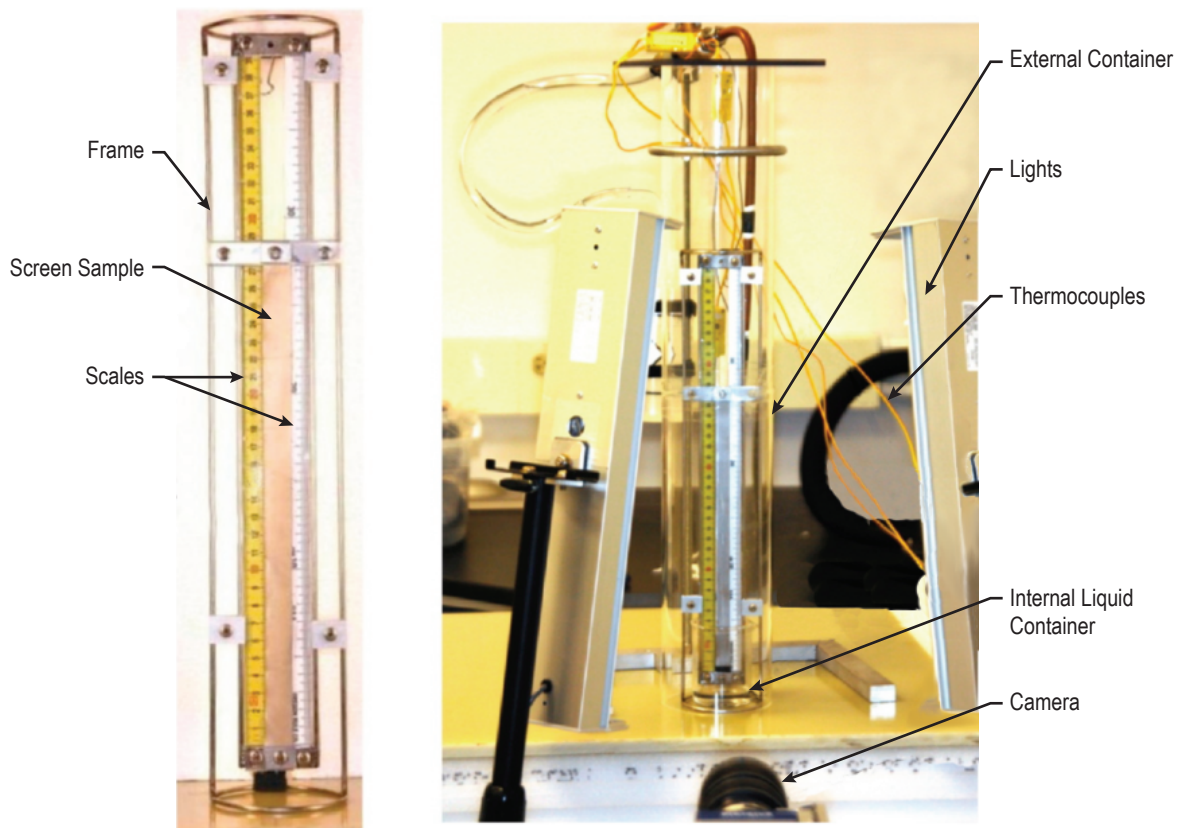
Figure 47. Wicking hardware for storable liquids.
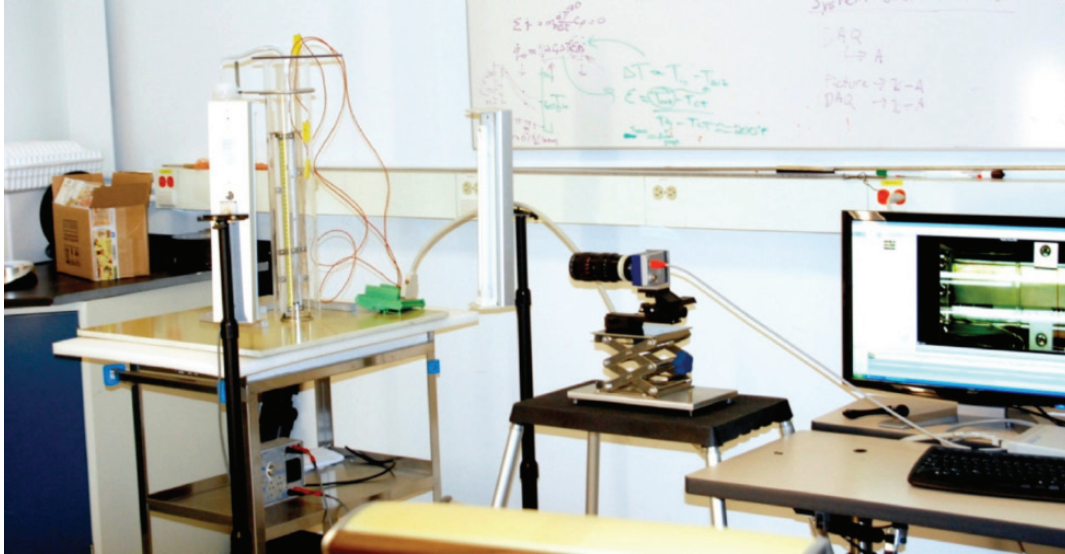
Figure 48. Vertical wicking test setup assembly.

Figure 49 displays the vertical wicking path when the flow is either parallel or perpendicular to the warp wires with a 165×800 mesh screen. Whenever the liquid velocity or movement was perpendicular to the warp wires, the wicking front was horizontal, or parallel to the warp wires (figs. 49(a) and 50). However, when the wicking movement was parallel to the warp wires, the front was inclined to the warp wires, i.e., parallel to the shute wire direction (figs. 49(b) and 51). The measured data were used to calculate the constants C_1 and C_2, which were then used to calculate the capillary and hydraulic diameters as shown.
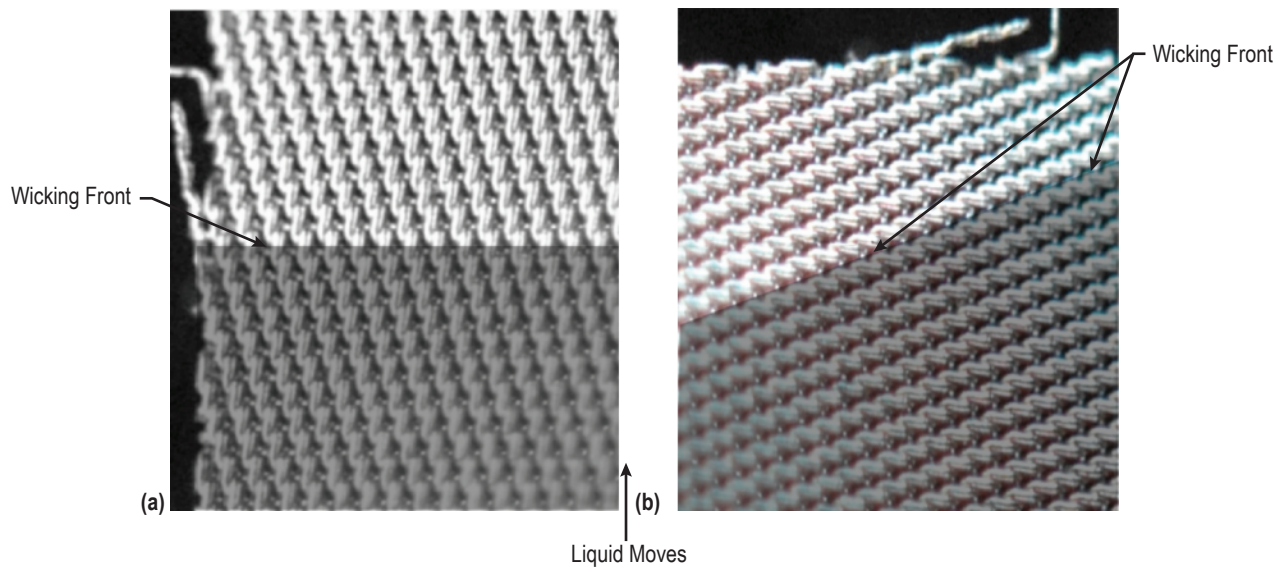
Figure 49. 165×800 mesh screen with direction of wicking indicated: (a) Perpendicular to warp wires and (b) parallel to warp wires.
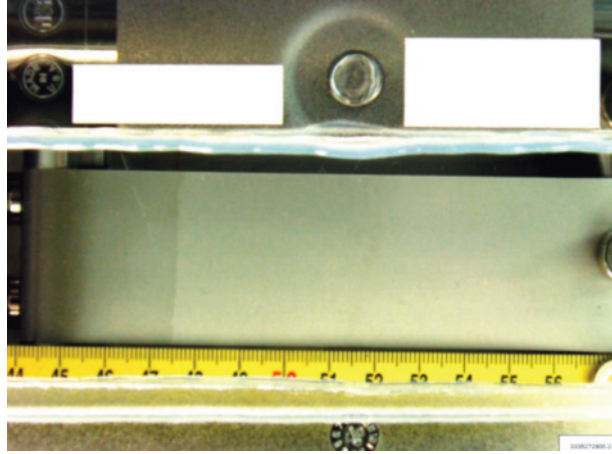
Figure 50. Horizontal wicking test—liquid moves parallel to the warp wires.
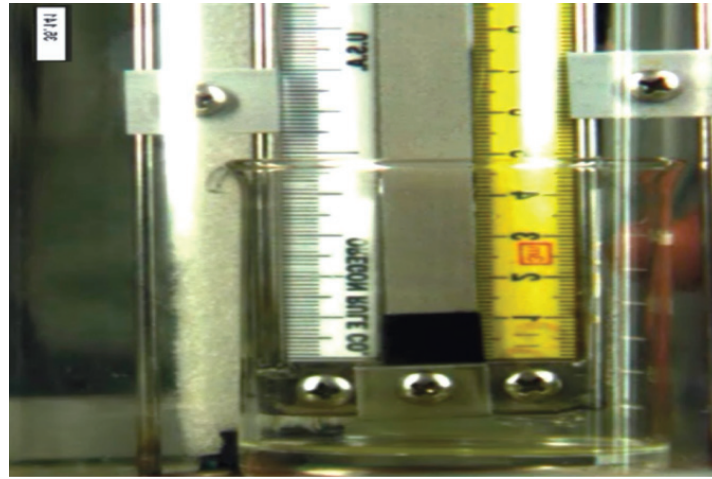
Figure 51. Wicking front moves parallel to warp wires.

For fitting experimental results in the form $t = K\,[C_1H + \ln|1 - C_1H\,|]$, the nonlinear least square method was used, and resulted in the system of equations:

$$
\left.
\begin{aligned}
K &= \frac{\sum_i t_i \left[C_1 H_i + \ln\left(1 - C_1 H_i\right)\right]}{\sum_i \left[C_1 H_i + \ln\left(1 - C_1 H_i\right)\right]^2} \\[2em]
\sum_i &\frac{H_i^2 \left\{ K\left[C_1 H_i + \ln\left(1 - C_1 H_i\right)\right] - t_i \right\}}{1 - C_1 H_i} = 0
\end{aligned}
\right\} .
\tag{1}
$$

Resolving these equation constants, C_1 and C_2 can be found and all parameters can be calculated:

$$D_c = \frac{4\sigma C_1}{\rho g \sin \alpha}, \quad K_f = \frac{4\sigma C_2}{\mu D_c} = \frac{\rho g \sin \alpha C_2}{\mu C_1}, \quad \text{and } D_h = \sqrt{\frac{32\mu C_1}{\rho g \sin \alpha C_2}}, \tag{2}$$

where D_c and D_h are the capillary and hydraulic diameters, respectively. For calculations, the Fortran program was used.

 The measured vertical wicking characteristics and analytical modeling correlations for the three screen meshes tested are presented in figures 52 and 53. The computed capillary diameters (D_c) and hydraulic diameters (D_h), based on measured wicking velocities, are presented in table 4 for the parallel and perpendicular wicking directions. Wicking height versus time for flow directions perpendicular and parallel to the warp wires with the 165×800 mesh screen are presented in figure 53. The wicking reached heights of about 0.11 m and 0.078 m in 1,200 s when the flow was perpendicular and parallel to the warp wires, respectively. It was noted that the wicking velocity was higher in the 'perpendicular to the warp wires' case. Wicking height versus time for the $200 \times 1,400$ and $325 \times 2,300$ mesh screens are presented in figure 54. The wicking reached heights of 0.087 and 0.056 m in about 1,150 s with the flow parallel and perpendicular to the warp wire direction, respectively, with the 200×800 mesh. Maximum heights of 0.067 and 0.056 m occurred in about 1,250 s with the $320 \times 2,300$ mesh screen. The analytical modeling compared very well with the experimental results with both meshes. It was noted that, consistent with observations by Symons,[2] maximum wicking velocities occurred with the flow parallel to the warp wires, in contrast to the 165×800 mesh. It was noted that evaporation was significant in all vertical testing and precluded any 'uptake' or flow rate measurements.
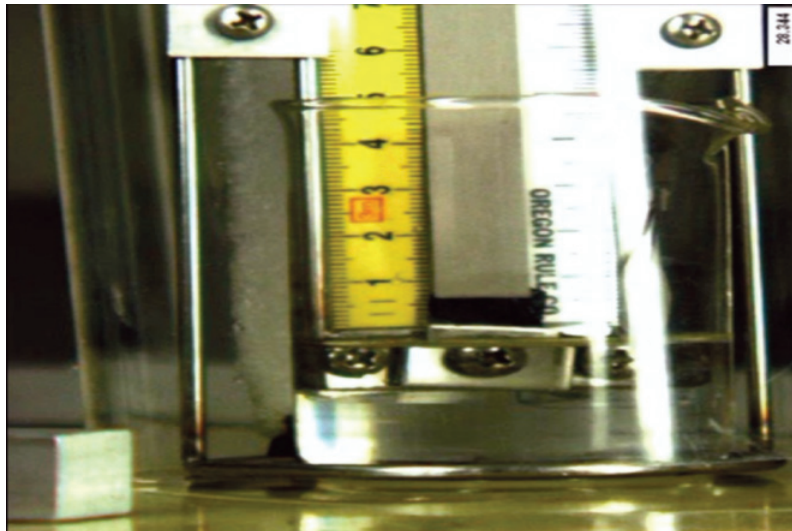
Figure 52. Wicking front moves perpendicular to warp wires.
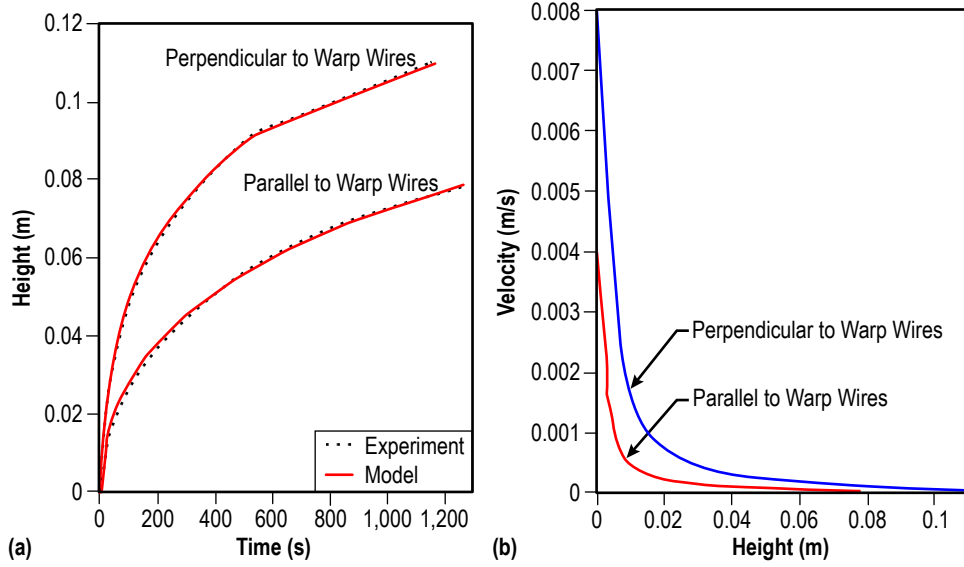
Figure 53. Wicking test results for vertical 165×800 mesh screen using isopropyl alcohol: (a) Height versus time and (b) wicking velocity versus height.

Table 4. Computed hydraulic and capillary diameters (in meters) in mesh screen.

	165×800	200×1,400	325×2,300
Parallel:			
D_c	9.545×10^{-5}	9.387×10^{-5}	1.036×10^{-4}
D_h	2.003×10^{-5}	1.974×10^{-5}	1.684×10^{-5}
Perpendicular:			
D_c	9.078×10^{-5}	1.238×10^{-4}	1.082×10^{-4}
D_h	3.710×10^{-5}	1.616×10^{-5}	1.385×10^{-4}

5.2.2 Preliminary Horizontal Wicking Testing

Horizontal wicking is of great significance because it is equal to that in zero gravity and therefore has direct application to on-orbit conditions. The vertical wicking rate testing enabled measurement of the hydraulic and capillary diameters which, in turn, are useful in analytical modeling of horizontal wicking. An analytical model for horizontal or zero gravity wicking has the following form for wicking distance versus time:

$$l = \sqrt{KD_e t} \quad , \tag{3}$$

where l is wicking distance in meters and t is wicking time in seconds.

$$K = \sigma \cos \Theta / 4 \mu \quad , \tag{4}$$
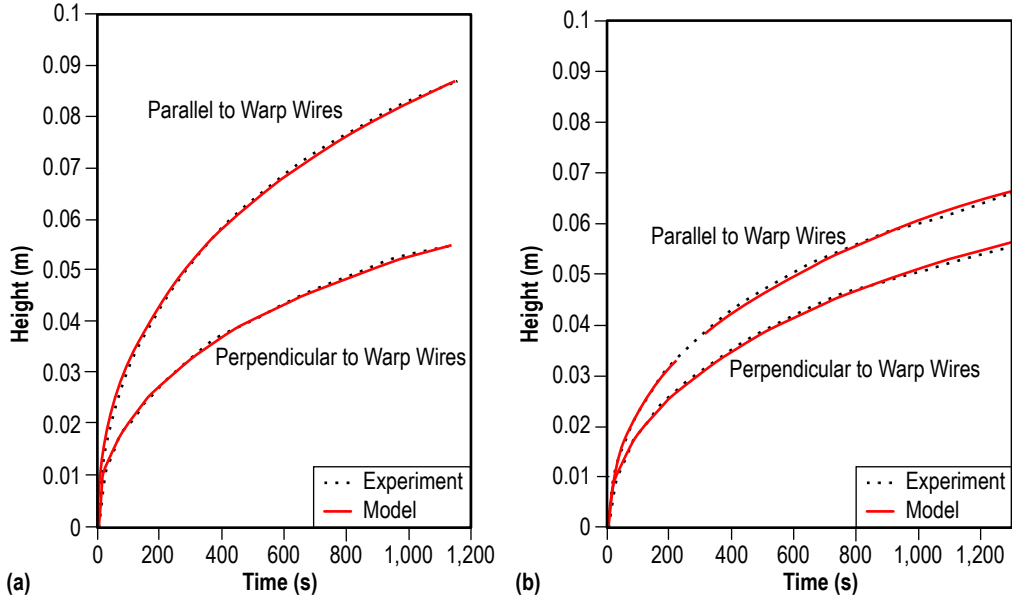
Figure 54. Isopropyl alcohol wicking test results for (a) $200 \times 1,400$ and (b) $325 \times 2,300$ vertical screens.

where the effective diameter (D_e), which is the combination of hydraulic diameter (D_h) and capillary diameter (D_c), is calculated via the relation:

$$D_e = D_h^2 / D_c .$$

(5)

Preliminary horizontal wicking is shown in figures 50 and 55, which show the liquid as it moves from left to right, parallel and perpendicular, respectively, to the warp wires of the $325 \times 2,300$ mesh. Wicking test results for the $200 \times 1,400$ and $325 \times 2,300$ meshes are presented in figure 56(a) and (b), respectively. With the $200 \times 1,400$ mesh, the wicking distance was 0.08 m within 52 s with the flow parallel to the warp wires; and wicked 0.055 m in 50 s with the flow perpendicular to the warp wires. With the $325 \times 2,300$ mesh, the wicking distance was 0.045 and 0.038 m within 40 s with the flow parallel and perpendicular to the warp wires, respectively. The computed wicking distance versus time correlated well with the measured data for both meshes. As noted with the previous testing, however, evaporation was significant and precluded any uptake rate measurements.

5.2.3 Alcohol Wicking Test Summary

Tests were conducted with noncryogenic liquid (alcohol) wicking on vertical and horizontal screens. When the liquid velocity was perpendicular to the warp wires, the wicking front was horizontal or parallel to the warp wires. When the wicking movement was parallel to the warp wires, the front was inclined to the warp wires, i.e., parallel to the shute wire direction. Wicking velocity in the parallel case was higher than in the perpendicular case, except for with the 165×880 mesh screen, which matches the Symons results from 1974.[2] Capillary and hydraulic diameters are different and both should be present in the theoretical model. Both vertical and horizontal wicking analytical models compared very well with the experimental results.
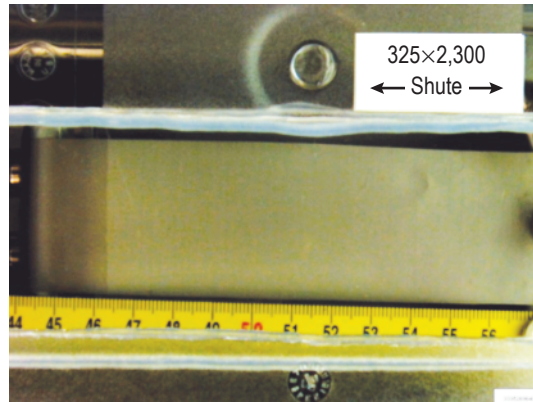
Figure 55. Horizontal wicking test—liquid moves perpendicular to the warp wires.
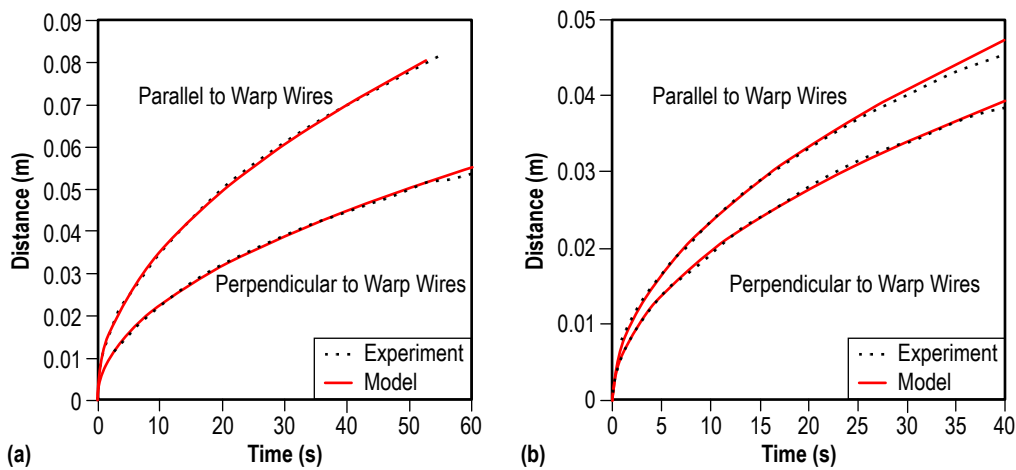
Figure 56. Wicking distance versus time results: (a) Horizontal $200 \times 1,400$ and (b) $325 \times 2,300$ mesh screen using isopropyl alcohol.

Therefore, the alcohol tests successfully served as a learning tool for the future cryogenic tests, enabled the measurement and analytical correlation of wicking rates, and allowed comparisons with data obtained by previous investigators. However, evaporation was noticeable in both horizontal and vertical testing and must be prevented if any uptake or capillary pumping experimentation is pursued in the future.

5.3 Liquid Nitrogen Wicking Tests

A cryostat was built for the purpose of characterizing the wicking properties of capillary screen meshes using LN_2 (see figs. 57 and 58). This apparatus resides in the hydrogen test facility at MSFC, Building 4628. Once the assembly was completed, the cryostat underwent cold-shock tests and checkout testing.
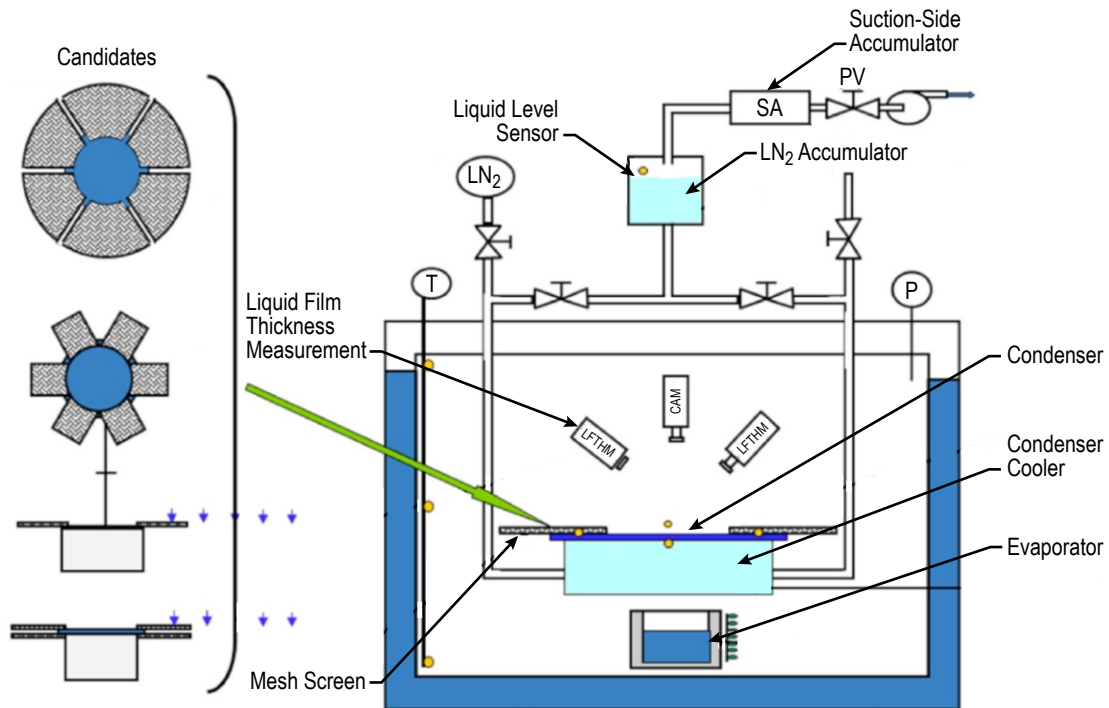
Figure 57. Phase 2 cryogenic test setup schematic.
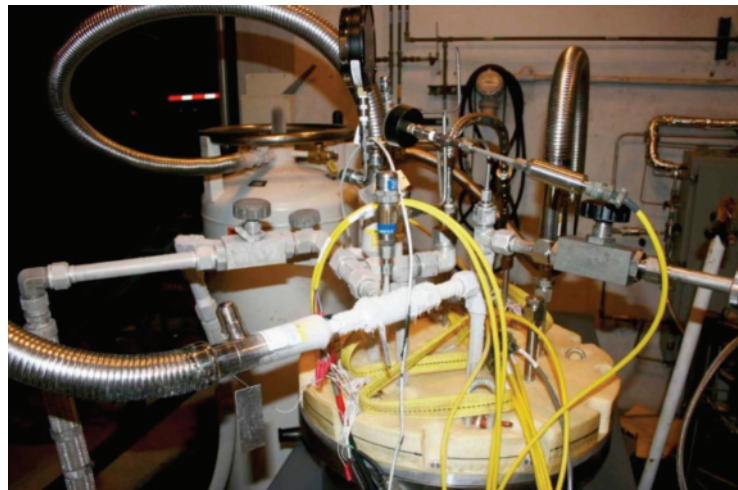
Figure 58. LN$_2$ cryostat assembly for wicking measurements.

The first tests were designed to measure the wicking velocity of LN$_2$ with a horizontally mounted screen using a digital camera mounted inside the cryostat. The laser profilometer (shown in fig. 59) was made by Δ-CAM, and was used to measure the level of the LN$_2$ reservoir, from which the total amount of mass taken up by the screen could be inferred. A new data controller card was installed in the profilometer to accommodate the scanning speeds required for measurement. A long
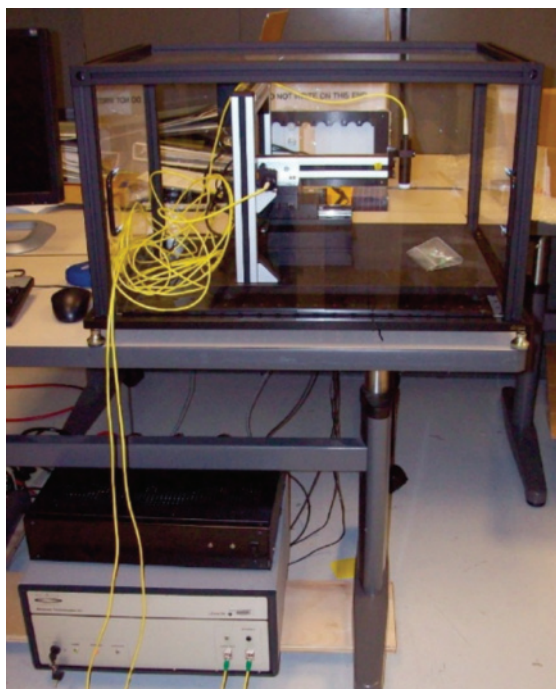
Figure 59. Profilometer for mass uptake measurements.

fiber optic cable and collimator were installed to allow the measurement to be made in the hydrogen test bay, while allowing the instrument to remain in the control room. Finally, the frame to hold the screen in position for horizontal wicking tests was designed and fabricated.

LN_2 test setup component pictures are shown in figures 60–64.

However, use of the LN_2 cryostat for measuring the LN_2 wicking properties of the wire cloth samples proved to be problematic. The in-chamber video camera suffered numerous problems due to the cold, and the nitrogen gas used to warm it introduced heat into the cryostat. It was difficult to sufficiently chill the source of LN_2, and it tended to boil when introduced into the reservoir and spatter the screen. Also, the required chilldown and warmup cycle for the cryostat limited testing to one test per day, which made the system difficult to troubleshoot.

A simpler apparatus was built (fig. 65) consisting of a dog-bowl Dewar with a purged vacuum window. The screen samples were held horizontally on a frame that was suspended in the Dewar and could be lowered so as to wet the end of the screen (fig. 66), which was bent to vertical with a radius of about 4 mm. A video camera with telephoto lens was mounted above the window, looking down, so that the screen could be imaged as it was dunked in the LN_2. A low-light camera was used so that the process could be photographed with just ambient light if necessary, to reduce glare in the image. Individual frames were captured from the video, and using image processing routines in IGOR Pro, the position of the wicking front as a function of time was determined (example shown in fig. 67).
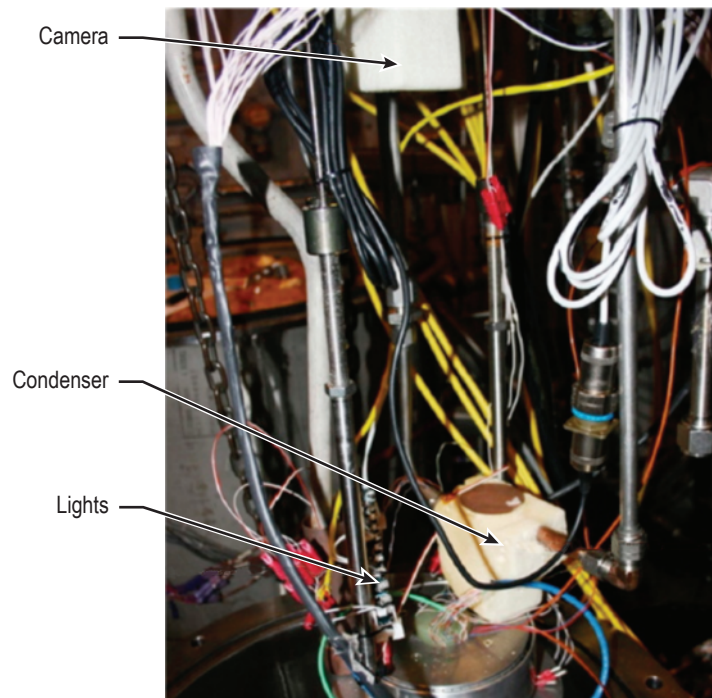
Figure 60. Assembled cryostat inside view.
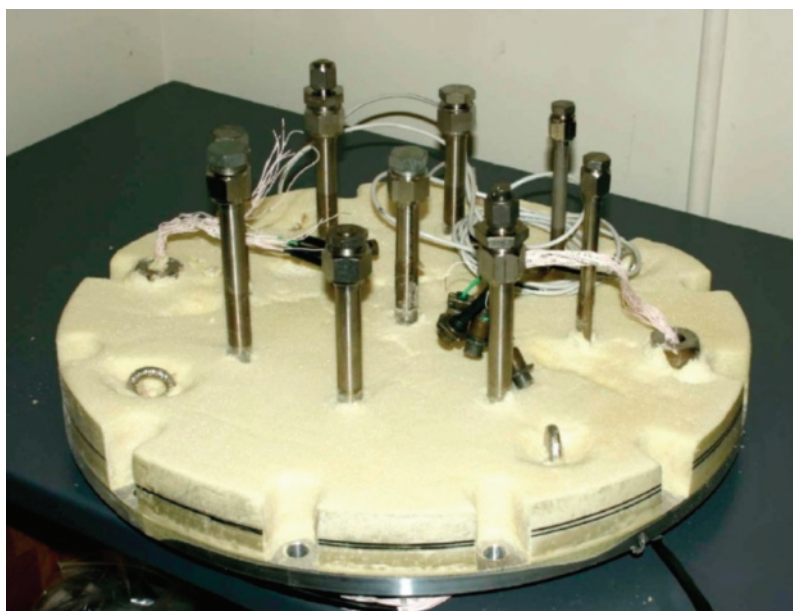
Figure 61. Insulated cryostat lid.

Figure 62. Insulated condenser.

Figure 63. Insulated LN_2 accumulator and condenser.

The data for one such case (the $325 \times 2{,}300$ mesh with wicking parallel to the shute wires) is shown in figure 68. As the wicking front was not itself perpendicular to the principle axis of the sample, both the leading and trailing-edge locations were recorded at each time interval. In addition, the estimated centroid of the wicking front was recorded, and it was found to agree well with just the average of the leading and trailing edge positions. The centroid was then used for all further data analysis. A curve given by

$$z(t) = z_0 + a_0 \sqrt{\left(t - t_0\right)} \; ,$$

(6)

which is equivalent to the well-known Washburn equation for fluid imbibition, was fitted to the data. The constants z_0 and t_0 are, respectively, the starting position and time of the liquid uptake, and as such, these are of little importance; they are artifacts of the particular experimental setup. The constant a_0, however, which incidentally, when squared, has units of a diffusion coefficient, should be

Figure 64. Equipment ready for assembly.

(a)

(b)
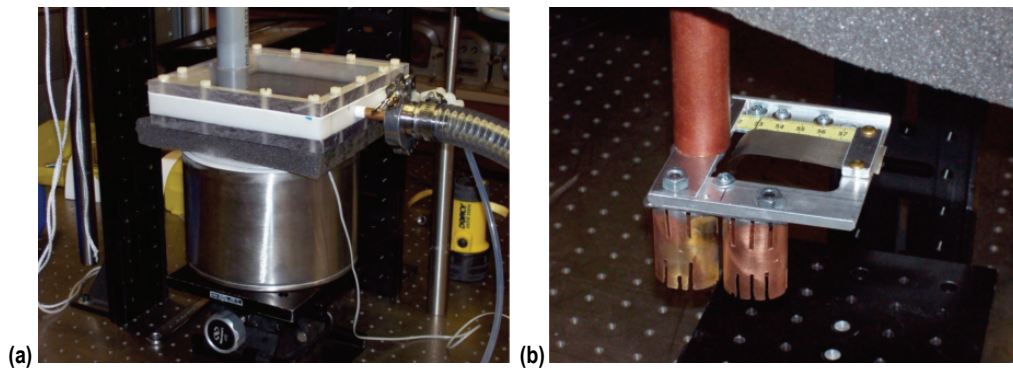
Figure 65. LN_2 wicking apparatus: (a) Dewar with purged window and (b) sample holding frame with cold finger.

a constant for the particular screen and liquid being used. In the case shown in figure 66, $a_0 = 4.2 \pm 0.2$ mm/s$^{1/2}$ = $(4.2 \pm 0.2$ mm$) \times 10^{-3}$ m/s$^{1/2}$. For the case where the wicking is parallel to the warp wires, $a_0 = (3.3 \pm 0.2$ mm$) \times 10^{-3}$ m/s$^{1/2}$.

5.4 Condensate Film Flow Analytical Modeling

The understanding of problems arising in connection with the film condensation and transport, acquisition and storage of cryogenic propellants for space-based propulsion systems has been improved. Some pertinent mathematical problems have been formulated, and their solutions obtained

Figure 66. Sample holder with screen sample immersed in LN_2.
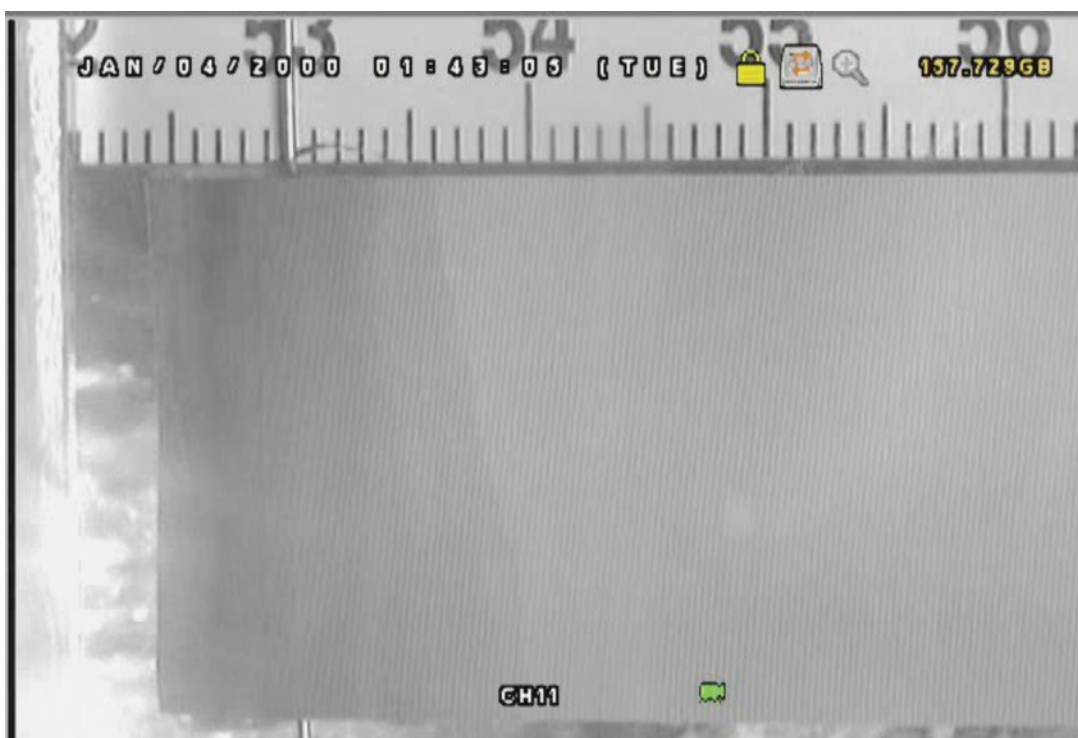
Figure 67. Wicking of LN_2 parallel to the shute wires in stainless steel $325 \times 2,300$ wire cloth.
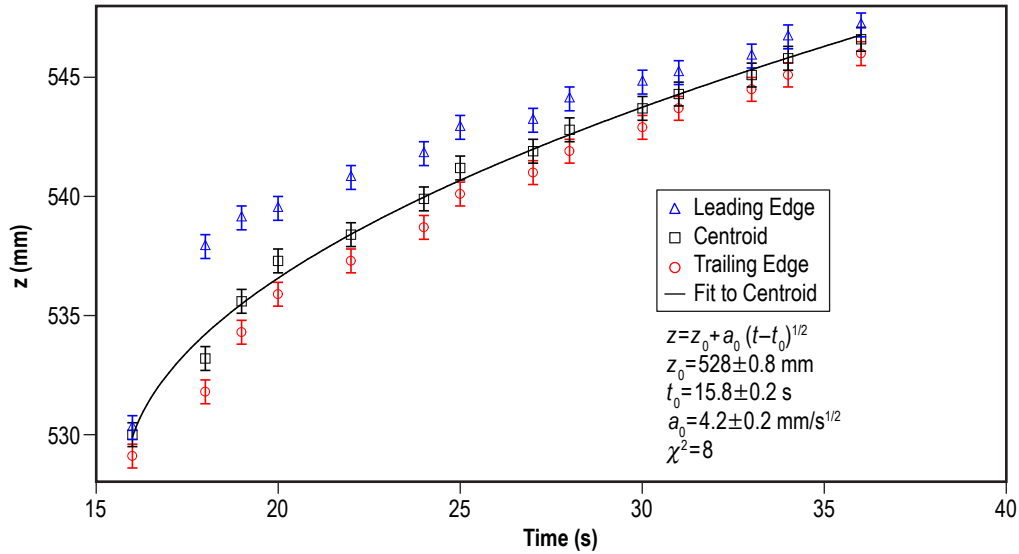
Figure 68. LN_2 wicking data for $325 \times 2,300$ wire cloth, parallel to shute wires.

in some cases. First, the pertinent scientific literature was surveyed. Whereas most of the literature addressed gravity-driven flows, a few papers were identified which consider the stability of a condensing/evaporating film with negligible gravity forces. Basic states with a time-dependent thickness of the film, but with no primary flow in the liquid film, were evaluated. Also, one-sided models, in which the vapor dynamics is largely neglected, were used.

5.4.1 Initial Modeling Approach

Next, an idealized but pertinent problem was analyzed, which concerns two parallel solid plates covered with liquid films on the inner sides. One plate is heated above the condensation/ evaporation temperature and the other plate is cooled below this saturated vapor temperature, so there is continuous evaporation of the warmer film and condensation of the vapor onto the colder film. However, the liquid films in this model, especially the condensing, thickening film, are unstable to small disturbances. Therefore, the solid plate was replaced with a porous one, through which the liquid film is removed under pressure. In contrast to the solid plate case, it was shown to be stable (except for certain exotic conditions) to small disturbances. Because the basic flow is steady and the velocity fields are uniform in space, the linear stability analysis is feasible, despite a large system of equations. The results of this work will later be submitted for publication in peer-reviewed scientific journals.

5.4.2 Liquid Film on Subcooled Horizontal Disk

Then, a more realistic geometry was considered. On the top of a subcooled horizontal disk, a liquid film condenses from the ambient saturated vapor. The liquid is forcedly removed at the disk edge, and there is an outward-directed axisymmetric flow of the film. The stationary regimes of the flow such that (a) the gravity is negligible, being eclipsed by the capillary, surface tension forces;

(b) the film thickness is everywhere much smaller than the disk radius; and (c) the so-called slow-flow lubrication approximation is valid. A nonlinear differential equation for the film thickness as a function of the radial coordinate was obtained. The two-dimensional fields of velocities, temperature, and pressure in the film are explicitly determined by the radial profile of its thickness. The equilibrium is controlled by two parameters: (1) The vapor disk difference of temperatures and (2) the mass transfer, or the liquid draining, rate:

$$b\left(h^3 h_{rrrr} + \frac{2}{r} h^3 h_{rrr} + 3h^2 h_r h_{rrr} + \frac{3}{r} h^2 h_r h_{rr} + \frac{1}{r^3} h^3 h_r - \frac{3}{r^2} h^2 h_r^2 - \frac{1}{r^2} h^3 h_{rr} \right) + h_{rr} + \frac{1}{r} h_r = c / h \ , \quad (7)$$

where

$$b = \frac{R\sigma\rho_v}{2M^2}, \quad c = \frac{3}{2} \frac{\rho_v}{\rho} \frac{\mu}{M} , \text{ and } M = \frac{k\Delta T}{l} \ . \tag{8}$$

For the flow regimes with a nearly uniform film thickness, the governing equation becomes linear:

$$\eta'''' = a h_0^{-5} - \frac{2}{r} \eta''' + \frac{1}{r^2} \eta'' - \frac{1}{r^3} \eta' \tag{9}$$

and the film interface has a concave-up quartic parabola profile:

$$h = h_0 + \frac{1}{64} a h_0^{-4} r^4 + \alpha r^2 \ . \tag{10}$$

Thus, perhaps counter to intuition, the liquid film is thicker at the edge and thinner at the center of the disk.

Next, emphasis was on development of equations for describing viscous radial film flow for a range of gravity effects. These equations have three additional terms:

$$b\left(h^3 h_{rrrr} + \frac{2}{r} h^3 h_{rrr} + 3h^2 h_r h_{rrr} + \frac{3}{r} h^2 h_r h_{rr} + \frac{1}{r^3} h^3 h_r - \frac{3}{r^2} h^2 h_r^2 - \frac{1}{r^2} h^3 h_{rr} \right)$$

$$-d\left(\frac{2}{r} h^3 h_r + 3h^2 h_r^2 + h^3 h_{rr} \right) + h_{rr} + \frac{1}{r} h_r = c / h \ . \tag{11}$$

For nearly uniform film thickness, one can create the following equation:

$$\eta'''' = a h_0^{-5} - \frac{2}{r} \eta''' + \frac{1}{r^2} \eta'' - \frac{1}{r^3} \eta' + \gamma \left(\frac{1}{r} \eta' + \eta'' \right) , \tag{12}$$

where $\gamma = g\rho R^2 / \sigma$ is the Bond number based on disk radius.

Although the film thickness variation is small, analytical definitions of the radial flow and the liquid vapor interface shape have been derived.

It has been determined that three regimes occur, depending on the disc Bond number:

(1) Small Bond numbers ($\leq$1): Capillary forces dominate the fluid motion; the surface profile is concave up and is approximated by a quartic parabola.

(2) Large Bond numbers (>1): Gravity forces dominate and the profile is concave down.

(3) Intermediate Bond numbers: Gravity and capillary forces are comparable—the profile near the disc center becomes concave down, and then with increasing radius, becomes concave up.

Results of these calculations are shown in figure 69.
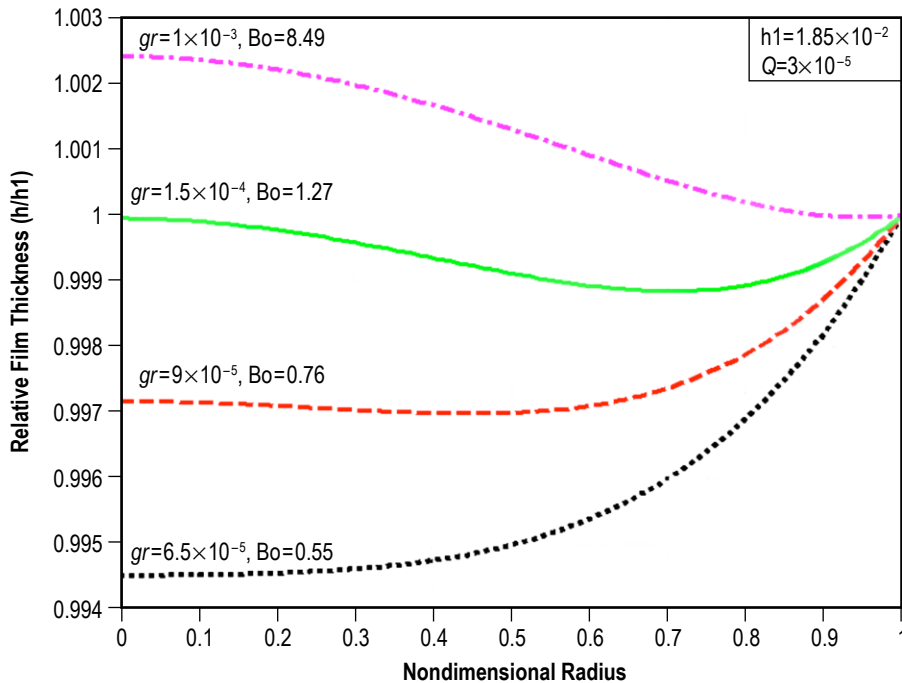
Figure 69. Condensate relative film thickness versus normalized radius.

A future phase would be to extend the modeling to include the effects of the presence of a noncondensable gas such as helium. Ultimately, the analytical modeling will assist in establishing approaches for assuring condensate coverage on a given screen mesh area.

5.4.3 Effects of Noncondensable Gas

The problem of noncondensable gas in microgravity vapor condensation was examined. To elucidate the effect in as pure a form as possible, a simple, self-consistent, one-dimensional stationary model was used. The system consisted of two parallel porous plates with a known higher pressure value outside the 'hot' plate and a known lower pressure value outside the cold plate.

Because of the pressure difference, the vapor with the known temperature is injected through the hot plate. The mixture of vapor and gas then flows toward the cold plate where the vapor condenses and the liquid is sucked through the cold porous plate by the lower pressure; however, the gas-liquid interface is impermeable to the gas. As a result, a heightened concentration of gas occurs at the interface such that its diffusive flux away from the interface exactly cancels its advection flux toward the interface.

The first principle equations (7)–(10) were used with appropriate simplifications to understand the effect. Because the gas concentration at the interface is higher, but the summary density is uniform, the vapor concentration at the interface is lower. Thus, the partial pressure of the vapor falls with the corresponding decrease in the saturated vapor temperature, which is the liquid temperature at the interface. Therefore, the temperature drop across the film can decrease significantly.

As a further development, the situation in a large, closed tank with a solid, initially quiescent mixture was considered. In the closed tank, vapor starts condensing on a solid disk with the liquid flowing to the disk edge and the condensation is eventually removed from the tank by wicking. The final stationary flow of vapor, noncondensable gas, liquid, and the liquid temperature profile are found in terms of such external parameters as the tank size, the disk temperature, the initial (resting) mixture temperature, the mixture pressure, the initial mass fraction of the gas, and the mixture mass flux.

The examination found that for each initial gas concentration that exists, the highest mass flow rate was found when a condensation process remained stationary (fig. 70). Above this maximum condensation process, the flow rate became unstable and had a periodical 'on-off' character.

Taking the mixture convection into account might relax this constraint. In the presence of gravity, however, there will be stronger convection due to buoyancy, and its mitigating effect will be stronger.
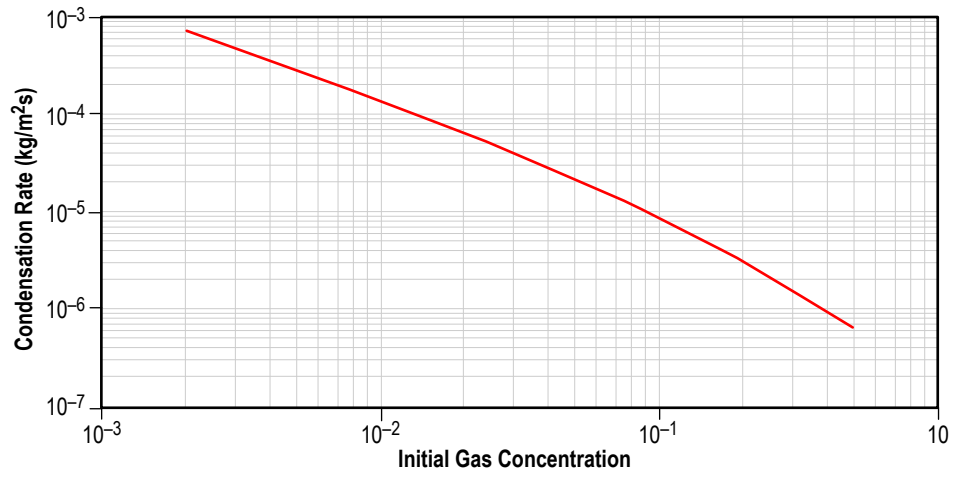
Figure 70. Maximum condensation flow rate.

6. SUBSCALE LIQUID ACQUISITION DEVICE THERMAL INTEGRATION TEST

A low-cost, fast-turnaround test apparatus was built to examine selected fluid and thermal integration problems involved with the subject feed system/LAD. The apparatus, depicted in figure 71, consists of a full-scale LAD mounted within a transparent tank and interfaced with a heated feed line mockup. The purpose of this setup is to enable the measurement of stratification within and outside of the LAD for various feed system heat loads. After a stratification pattern is established, mixing can be activated and the destratification can be evaluated for various mixing rates and techniques.
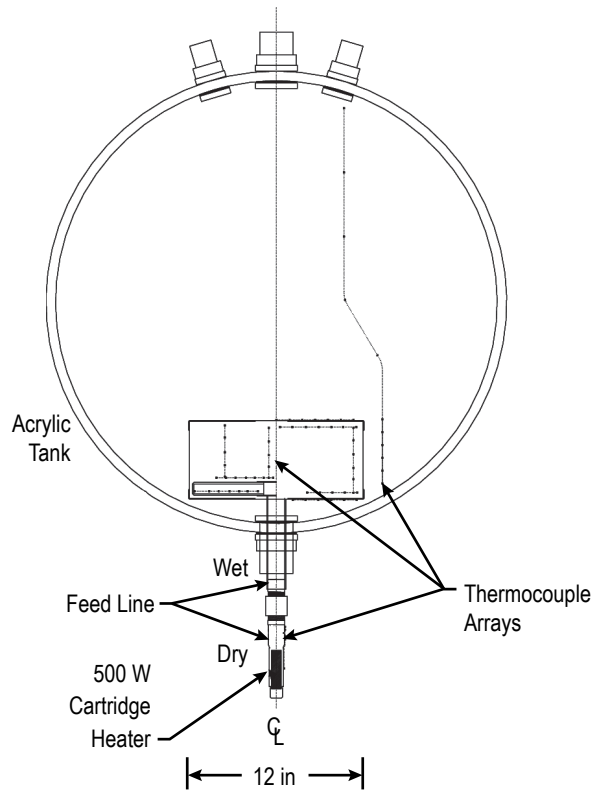
Figure 71. Plan view of transparent tank, with LAD.

A design for a full-scale start basket type LAD was provided by GRC. It was built and installed in the water tank, which has half the volume of the LCH_4 tank envisioned for Altair. The start basket, water tank assembly, and instrumentation for the test are described in sections 6.1–6.3. Presentation of the test data, along with a qualitative discussion of it, is presented in section 6.4. In section 6.5, the data are discussed in light of the thermal modeling and computational CFD model and an empirical scaling relationship.

6.1 Liquid Acquisition Device

The full-scale LAD mockup design provided by GRC (D. Chato, GRC, Personal Communication, January 2009) is a start basket, with a four-armed channel assembly at the bottom of the basket that is connected to the propellant feed line. The top and bottom plates are connected by four vertical vanes at 90-deg intervals. The channel assembly sat between these vanes and was raised roughly 6 mm (0.25 in) above the bottom plate. Ideally, the LAD should be made out of the thinnest gauge steel possible (the original design called for 0.89-mm- (0.04-in-) thick stainless). However, this was deemed too difficult to weld; for the purpose of this test, thicker material permitted the device to be made at a reasonable cost. The top and bottom plates, as well as the vanes, were made of 1.65-mm- (0.065-in-) thick 316 stainless, the channel assembly was made of 3.05-mm (0.12-in) wall square tube (316), and the feed line was made from 38.1-mm (1.5-in) o.d., 2.41-mm (0.095-in) wall stainless 304 tube. The added thermal mass due to the thicker material should be no more than 2% of the total thermal mass of the filled start basket. The start basket is shown in figure 72.
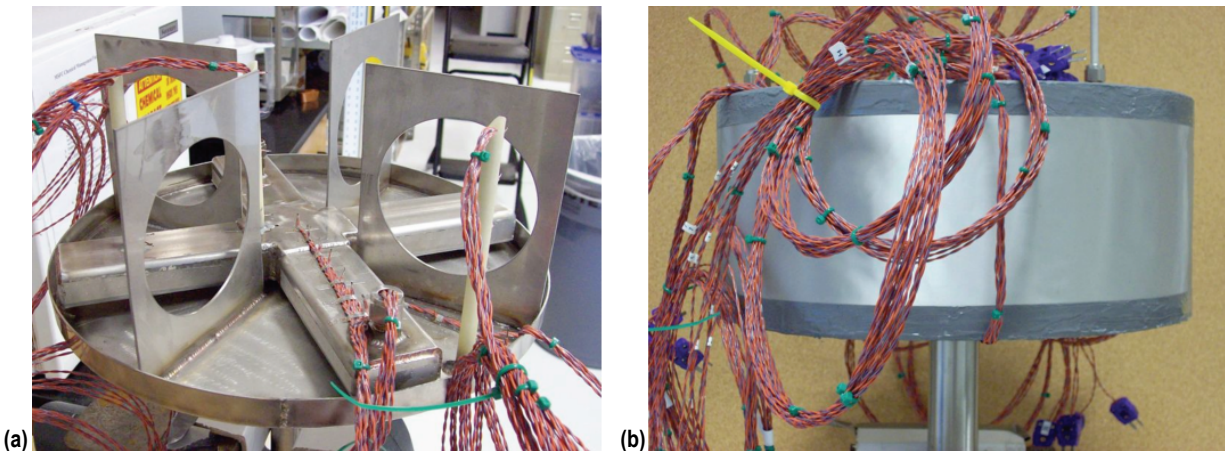
Figure 72. Start basket test hardware components and assembly pictures: (a) Interior before final assembly, showing vertical vanes, channel subassembly, and TC arrays and (b) finished, instrumented.

The bottom of each of the channel arms was covered with stainless steel, dutch twill wire cloth with a $325 \times 2{,}300$ (warp $\times$ shute) mesh. The warp wires were aligned perpendicular to the axis of the channel arms (i.e., perpendicular to a start basket radius). The outside circumferential boundary of the basket was also covered with the $325 \times 2{,}300$ dutch twill screen. In both cases, the screen was tack-welded in place, and the edges were sealed with J-B Weld epoxy. The overall dimensions of the LAD, as-built, were as follows: a diameter of 348 mm (13.7 in) and a height of 156 mm (6.13 in).

6.2 Test Apparatus

The water tank consists of two 914-mm-o.d., 19-mm-thick plexiglass hemispheres (36 in o.d., ¾ in thick) with circumferential sealing flanges. This yields a total volume of just about half that of the subject LCH_4 tank (1.1 m diameter). The tank is mounted on an aluminum table top (fig. 73) that sits on four Omega LBM-500 load cells, with a total capacity of 910 kg (2,000 lb). The load cells permit the total weight of the water, and hence the water inventory, to be measured. When full, the tank holds ≈380 kg of water. The feed line is connected to the start basket with a pipe union that has been welded closed.
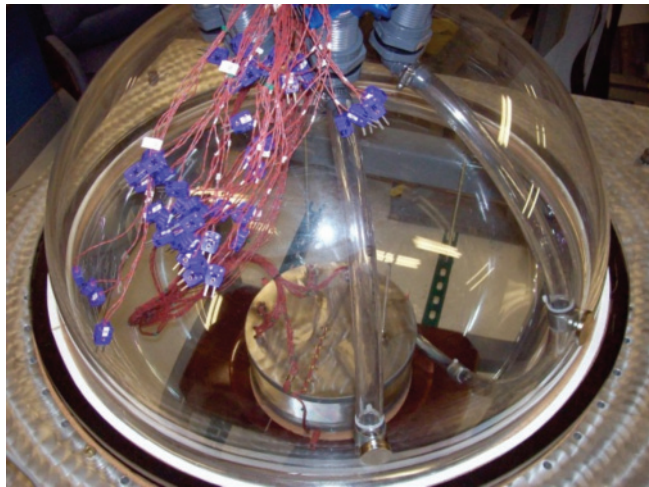
Figure 73. Water tank (empty) with start basket installed.

The start basket is sealed with an O-ring lip seal onto a PVC fitting, which fits through a hole in the bottom of the tank and is sealed with a neoprene gasket. The feed line attached to the start basket is mated to the heater pipe with a closed pipe union that separates the wet and dry sections of the feed line. Cabling for instrumentation goes out through several PVC fittings at the top. Pictures of the water tank are shown in figures 73 and 74.

A water transfer system was built to fill, drain, and circulate water in the tank (shown in fig. 75). It has a 5-μ particulate filter and an ultraviolet purification system. These, along with the addition of a small quantity of bleach, serve to keep the water clean and algae free. Initially, there was concern that the tank would be filled with water bubbles; however, this has not been the case. The cleaning procedures used seem to be adequate; elimination of microscopic debris, which can act as nucleation sites for bubbles, appears to be sufficient.

The input heat is provided by a cartridge heater that fits inside a dry section of pipe below the pipe union, which separates the wetted and dry sections of the feed line. Initially, a long section of stainless steel pipe, instrumented with TCs at regular intervals, was used to house the heater. The intention of this was to fit the TC data to a one-dimensional analytical model of conductive heat
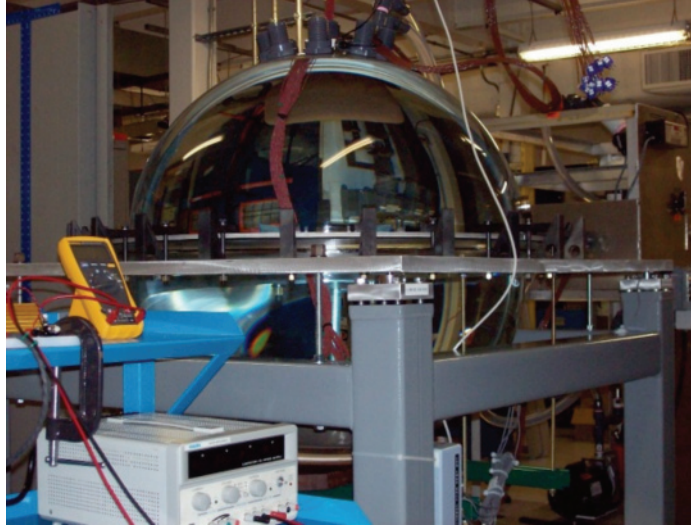
Figure 74. Water tank (filled) with start basket and instrumentation cabling installed.

Figure 75. Water supply system control panel.

flow in the annular volume of the pipe, so as to infer the heat flux. However, in addition to being too long, the low thermal conductivity of the steel limited the amount of power that could be added to the LAD to only 1 W, without melting the applied insulation (spray-on polyurethane foam).

The heater pipe was subsequently redesigned; it was made shorter, and made out of several layers of nested copper pipes, soldered together, and in turn, soldered into a copper pipe fitting. The decreased length and higher thermal conductivity of copper ($\approx$25 times higher than that of stainless steel) resulted in improved heat flow.

The pipe was stuffed with glass wool to prevent convection within the pipe, and ensure that the heat is mostly conducted along the pipe wall. The heater was smeared with heat-sink compound (zinc oxide in silicone grease) and installed in the pipe with brass shim stock to make good thermal contact. The heater (cartridge type) is rated for 500 W at line voltage, but for this test was operated with a dc power supply to provide an adjustable heating power in the range of 1 to 40 W. A picture of the heater and pipe is shown in figure 76.

Figure 76. Heater assembly with pipe and cartridge heater.

Once the heater was installed, the entire assembly below the tank was insulated with a 4-in-thick layer of wrap-on polyurethane foam. The foam was tested for heat resistance, and found to suffer no degradation up to temperatures of about 480 K. This set the maximum power that could be applied to the heater; with a heating power of 40 W, the peak temperature reached at the inside surface of the foam layer was about 470 K.

As before, TC probes were located along the length of the heater assembly to infer the heating power. However, this technique proved problematic given the irregular shape and construction of the heater pipe. It cannot be assumed that heat will flow uniformly through the annular cross section, especially given the high thermal conductivity of copper. Instead, an effective thermal conductance is estimated, $G_{th} = \Delta A$, where Δ is the thermal conductivity and A the relevant cross-sectional area. The thermal conductivity of the polyurethane foam is 0.02 W/m·K, while that of copper at 370 K is 394 W/m·K. The perpendicular conductance (i.e., through the wall of the pipe and into the foam along the entire length of the pipe) is found to be no more than 1% of the parallel conductance (i.e., along the pipe and through its cross section), under a variety of assumptions. This simple estimate does not take into account the actual temperature differences. From the actual test data, the perpendicular heat flow was estimated using the highest temperature measured on the heater pipe (the most pessimistic assumption), and was found to be no more than 2% of the applied heating power, up to the highest applied heat load of 40 W. This error of –2% is taken to be the maximum systematic error in the applied heating power, and it is of order of or smaller than the random error.

The ambient temperature in the laboratory varied considerably over the course of a day and from day to day. To counter this, the air conditioning was left running all the time. Even with this, the ambient temperature swung about 2.5 K (fig. 77).
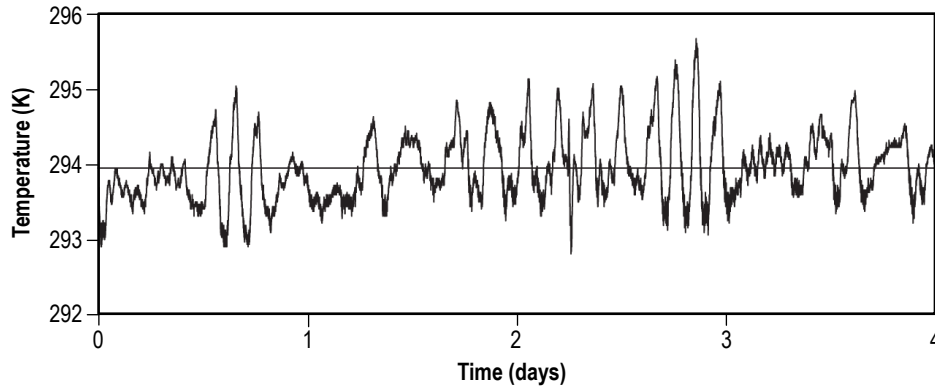
Figure 77. Ambient temperature above the tank measured over several days. The solid horizontal line is the average temperature over this time.

For added thermal stability, the tank was surrounded with a wall (welding screens) and insulated with ≈200 ft^3 of Styrofoam and cellulose packing peanuts (fig. 78). This measure reliably insulated the tank from severe temperature excursions over the (typically) several-day-long test runs. The residual heat leak through the walls of the tank was estimated to be ≈20 W, resulting in slow warming or cooling of the bulk fluid, depending on whether the initial temperature of the water was cooler or warmer than the average room temperature, respectively. After a test run, the bulk was allowed to cool for some time prior to the next test. Before several of the test runs, water was pumped out of the tank and replaced with cooler water so as to bring the temperature of the bulk fluid closer to ambient.

6.3 Instrumentation

The behavior of the fluid heating was characterized with two kinds of diagnostics—temperatures within the LAD and tank made using several arrays of TC temperature sensors. In addition, the flow patterns were photographed using a flow visualization system. An overall schematic of the diagnostic system is shown in figure 79. These two diagnostics will be described in greater detail in the following sections.

6.3.1 Temperature Diagnostics

Temperature measurements are made with type E TC probes. There are a total of 55 TC probes in nine arrays within the interior volume, attached to the top and bottom plates, and inside one of the channel arms (shown in fig. 80). There are an additional 12 TC probes on a vertical array inside the tank to measure temperatures in the bulk liquid, and 1 TC probe suspended above the tank to record the ambient temperature. The free-standing probes were made with a Hot Spot II TC bead
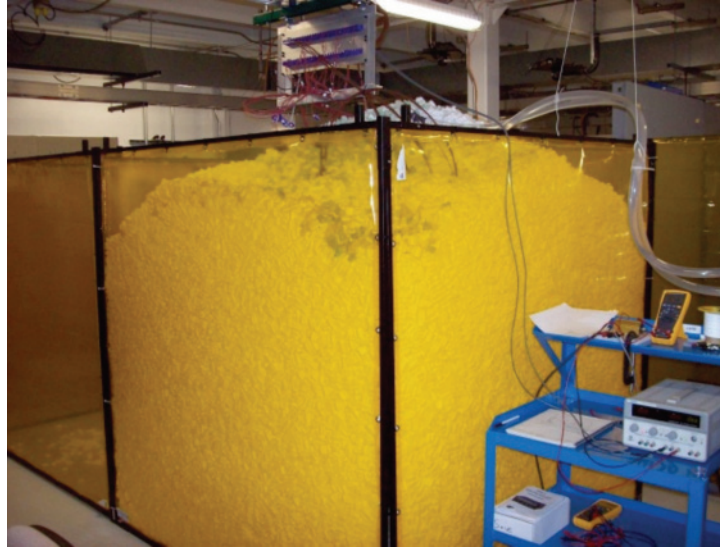
Figure 78. Water tank with insulation.
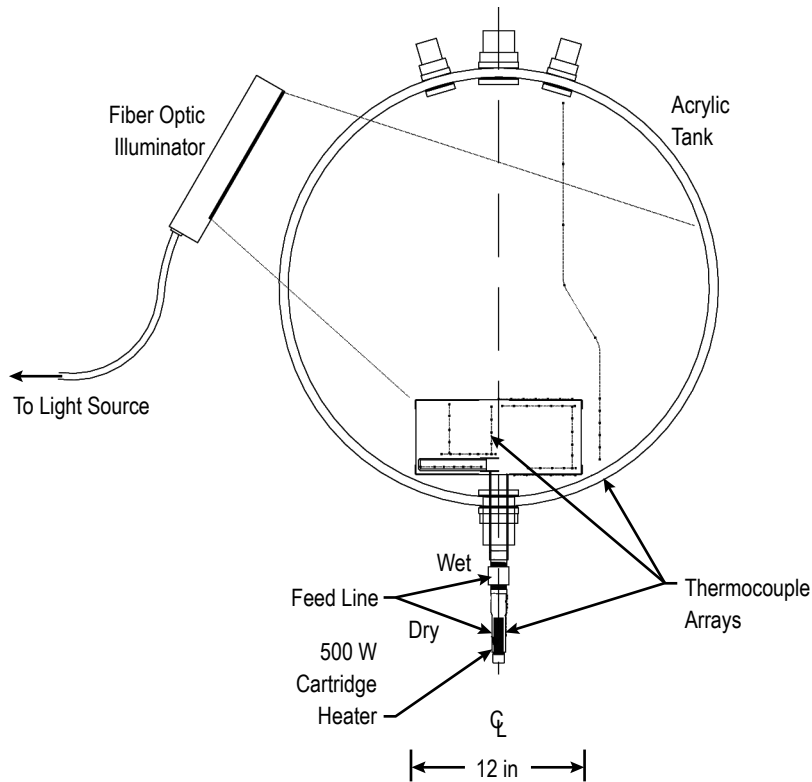
Figure 79. Diagnostics for the subscale tank, including TC arrays and the light source for flow visualization measurements (camera omitted).
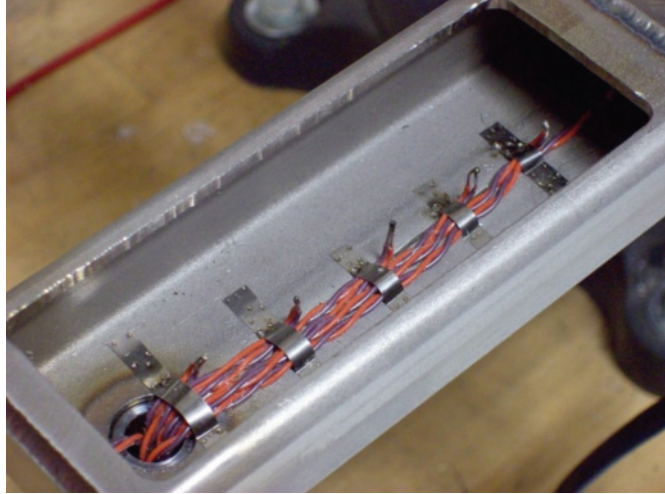
Figure 80. Thermocouple array A inside the start basket channel.

welder (made by DCC, Corp.) to ensure uniformity. The probes bonded to surfaces were spot welded in place.

The TC arrays within the start basket are distributed throughout all four quadrants, so as not to occlude too much volume in any one volume. For the purposes of comparing the data to the CFD model, the domain of which is only one quadrant, equivalent locations for the probes were calculated so as to fold them all over into just one quadrant.

The TC data are recorded with National Instruments compact Field Point TC modules (NI cFP-TC-125) used together with cold-junction compensators (NI cFP-CB-3). The vertical resolution of these digitizers was estimated at about 5 mV per bit, which corresponds to a temperature difference of 7 mK (given the 69 mV/K resolution of type E TCs). The applied heating power is measured by recording the voltage across the heater and the voltage across a precision current sense resistor ($R = 5\ \Omega$). These voltages are read into a digitizer and recorded continuously over the entire duration of a test. The digitizer modules are integrated into a compact, mobile data acquisition system adjacent to the test apparatus that is operated with LabVIEW™.

6.3.2 Flow Visualization

A particle image velocimetry (PIV) system was employed to image the liquid flow in the tank under the conditions of a heat leak introduced in the feed line. With PIV, the fluid is seeded with small tracer particles that move with the fluid, and imaged using a video camera.

The interior of the tank was lit illuminated with a fiber optic system made by Dolan-Jenner Industries, consisting of a 30.5- ×0 .05-cm (12- ×0.02-in) line light with a 10.12-cm- (4-ft-) long fiber optic bundle (model No. QF5548) coupled to a long-life, 100 W, metal halide lamp with a color temperature of 6,000 K (model No. MH-100A). The light was collimated using a cylindrical lens (a 1.27-cm (0.5-in) o.d. cladded glass rod) just in front of the line light and a slit, 21 cm (8.25 in)

beyond it. This produced a light sheet approximately 1.9 cm (0.75 in) wide across the width of the tank, which was directed toward the bottom half of the tank to illuminate the region just above the LAD (fig. 81). To eliminate any stray light from the light source, it was enclosed in a box made out of black poster board. The tank was wrapped with heavy black cloth to keep out the ambient room light.
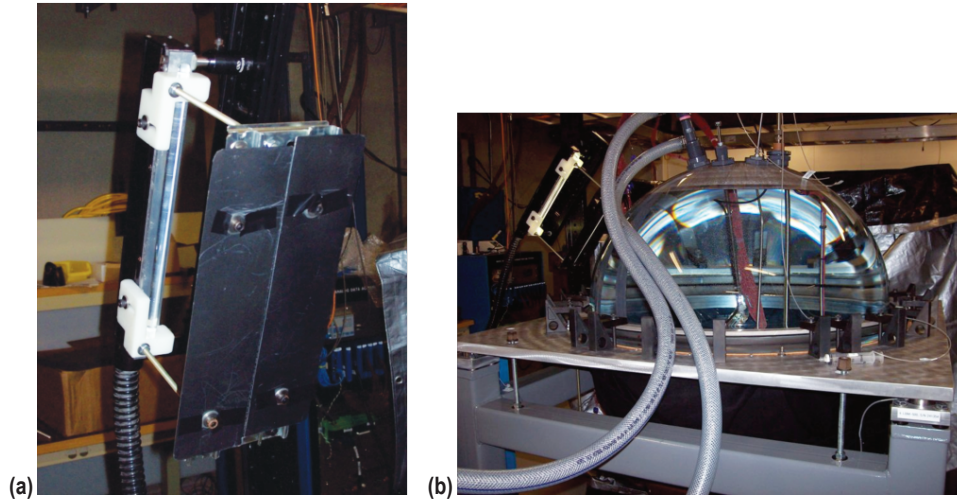
Figure 81. Tank interior lighting arrangement: (a) Line light source with collimator, and (b) line light source (at left) mounted next to the tank.

Because of refraction at the tank/water interface and to the distortion produced by the curved walls of the tank, it was not possible to photograph the flow using an externally mounted camera. An external camera mounted to a borescope, and using a right-angle prism, was tried; however, the resulting image had poor resolution and insufficient field width. Instead, an immersible camera was used (made by Lights, Camera, Action Inc.). It was installed in the tank on a swivel arm that allowed it to be swung through a limited arc (about 90°) providing a field-of-view adjustment.

A variety of tracer particles were available for these measurements: white nylon microspheres (made by Cospheric) in sizes ranging from 10 to 106 μ, 6-μ-diameter polystyrene beads, dyed in blue and red, and fluorescent polystyrene microspheres. These spheres have densities close to that of water (1.15 g/cm^3 for nylon, 1.05 g/cm^3 for polystyrene); however, they were too buoyant to track the flow, quickly rising to the surface upon introduction. Much better results were obtained with rheoscopic tracer particles obtained from Kalliroscope Gallery, Groton, MA. These small TiO_2-coated mica flakes, with sizes ranging from 4 to 30 μ, are very close to neutrally buoyant, align with the flow, and remained in emulsion for long periods of time (several days), permitting extended testing periods. The tracer particles were injected in the tank from a syringe using a spray rake, consisting of thin nylon tubing affixed to stainless steel tubes. The spray rake was situated above the LAD, and could be swiveled into and out of the light sheet. The camera and spray rake arrangement is shown in figure 82.
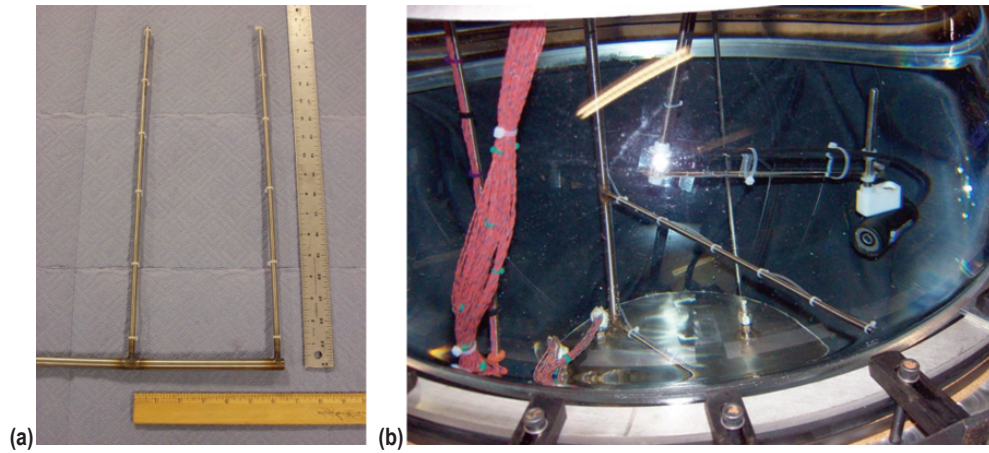
Figure 82. Camera and spray rake arrangement for particle tracing: (a) Camera and (b) spray rake.

6.4 Test Results

6.4.1 Temperature Measurements

For reference in the following discussion, the locations of the various TC probe arrays, fanned out as if they lay in one plane, are shown in figure 83. The probes in a given array are numbered, and ordered up (vertical) and out (radial) with increasing number.
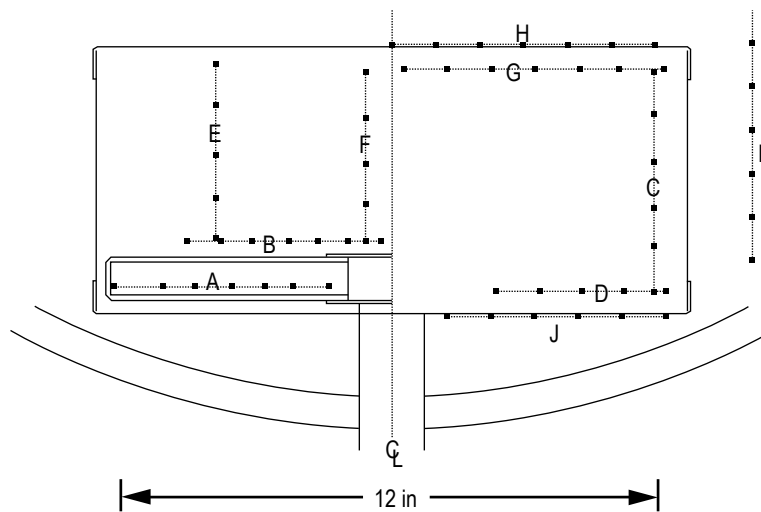
Figure 83. Temperature measurement array layout.

A series of tests were conducted at nominal power levels of 2, 5, 10, 20, and 40 W. A number of qualitative features are common to all the test cases, and these will be illustrated with the 20 W case; the actual heating power for this test, P_{heating}, was measured to be $P_{\text{heating}} = 19.5$ W. The data were recorded at a sampling rate of 0.05 Hz (1 sample per 20 s). Sampling rates of 1 and 10 Hz were also tried for brief periods, but no temporal features in the data were seen at these higher speeds. This test was run for about 4 days, and an overall quasi-equilibrium was attained, although the temperature in the tank continued to increase as the heating power was at or above the estimated heat leak of the tank. The run time, however, was sufficient for the start basket to come into equilibrium with the bulk fluid. Figure 84 shows the data from array J, which is on the underside of the lower plate. The temperature at J1, closest to the feed line, increased rapidly at first and at a much higher rate than the more outboard probes, where the heating was progressively weaker. This indicates that much more heat is being conducted up the feed line, than radially through the bottom plate, which makes sense, given that it is thicker.
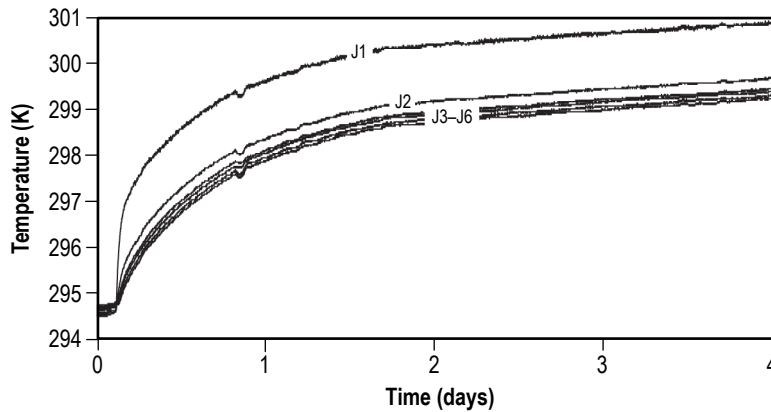
Figure 84. Temperatures recorded on array J, on the bottom of the lower plate. $P_{\text{heating}} = 19.5$ W.

The temperatures in the channel arm (array A) are shown in figure 85. There is a similar, though less pronounced, trend as on array J, perhaps indicating that heat is leaving the top of the channel assembly. There is an oscillation in the temperature at the inboard most probe (A1) with a period of 7–10 hr. This is not due to electrical noise, as it does not show up early in the test, and there is no corresponding signature in the applied power; it appears to be an actual thermal effect.

Figure 86 shows the temperatures recorded on array E, a vertical array above the channel arm at a radius of 101.6 mm (4 in), about two-thirds of the start basket radius. Before heating, the temperatures were stratified as one would expect (lower left corner of the graph), then got progressively warmer, by 0.4 K, from probe E1 to E5. This temperature difference is less than the accuracy of type E TCs, but within the observable precision of these devices. That is to say, in many trials, in cases where there was no external heating, stratification profiles were observed with temperature differences of 0.1 K or less between probes, and these profiles were reproducible and agreed with expectation for an unheated, unmixed fluid. As heat is applied, all five probes converge to one temperature, and remain there during the whole course of the test. This indicates a convective fluid flow through

Figure 85. Temperatures recorded on array A, inside the channel arm. $P_{\text{heating}} = 19.5$ W.
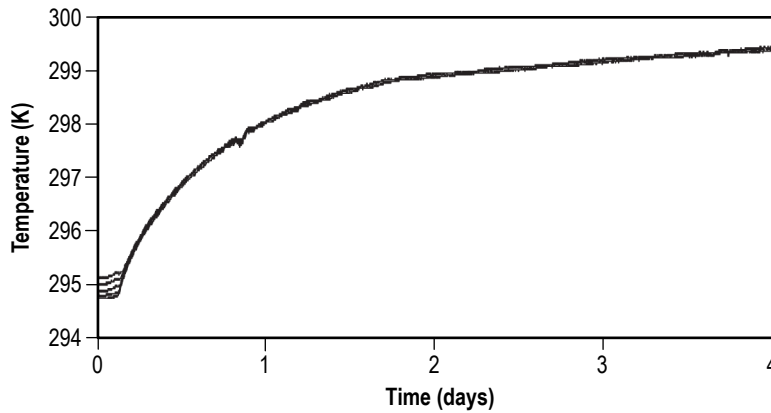
Figure 86. Temperatures recorded on array E, above the channel arm. $P_{\text{heating}} = 19.5$ W.

this region, washing out any temperature differences. Figure 87 shows the temperatures recorded on array F, a vertical array above the channel arm, at a radius of 15.2 mm (0.6 in), close to the centerline. For clarity, only probes F1 and F5 are shown. Before heating, all five probes exhibit the vertical stratification as with array E. After some time, their relative temperatures switch, and probe F1, closer to the channel assembly, becomes warmer than probe F5. Before heating, F1 is cooler than F5 by about 0.4 K. After equilibrium is reached, F1 is warmer by about 0.2 K. The initial temperature profile is partially washed out after the onset of heating, but not so completely as at the location of array E, indicating that any convective flow must be farther outboard than 15.2 mm (0.6 in) from the centerline.

Figure 88 shows the temperatures recorded on array D, spanning radially outward within the fluid, above the bottom plate. These traces show similar features to those from array E. In this case, the initial temperatures appear to be stratified radially (inside to outside, cold to warm), and these
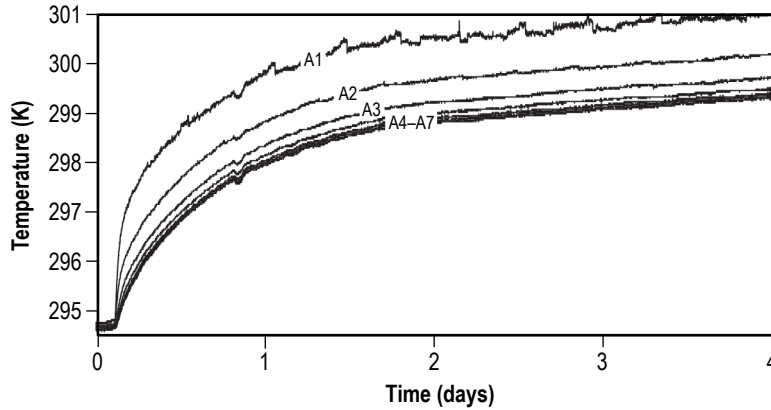
Figure 87. Temperatures recorded on array F, above the channel arm. $P_{heating} = 19.5$ W.
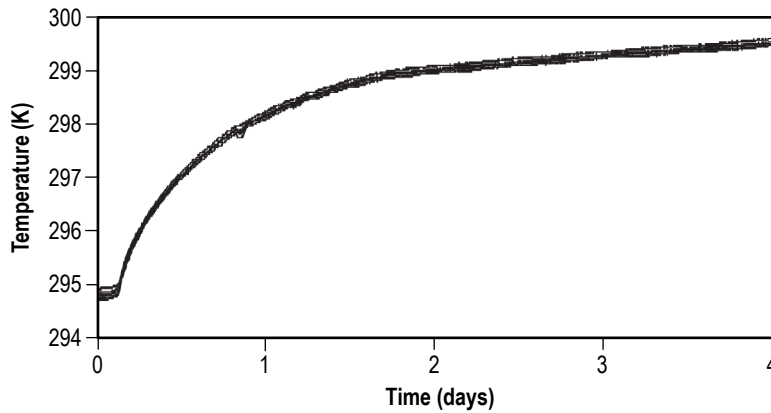
Figure 88. Temperatures recorded on array D, above the bottom plate. $P_{heating} = 19.5$ W.

differences are washed out as equilibrium is developed, as if there were the return flow of a convective cell at these probe locations, along the bottom of the start basket; however, it is not so distinctive here as is the case with the vertical array E.

Shown in figures 89 and 90, respectively, are the data from array G, inside the fluid spanning radially outward below the top plate, and array H, bonded to the top plate on the outside of the start basket and spanning radially from the center to the outer edge. Upon examination of the data, no particular trends emerge other than the overall heating.

Figure 91 shows temperatures recorded by array L, inside the bulk fluid over the course of the entire test run. Probes L1 through L6 are arrayed vertically 38.1 mm (1.5 in) from the start side-wall of the start basket, as shown in figure 90. Probe L7 and L9 are 127 mm (5 in) and 355.6 mm (14 in) above the start basket, respectively, and both are immersed in water. Probe L11 is 24 in above the start basket and in the ullage volume above the liquid.

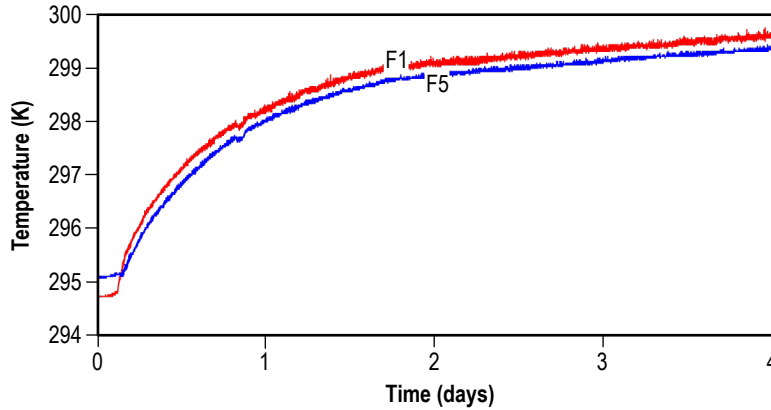Figure 89. Temperatures recorded on array G, below the top plate. $P_{\text{heating}} = 19.5$ W.

Figure 90. Temperatures recorded on array H, radially along the top plate. $P_{\text{heating}} = 19.5$ W.

Figure 91. Temperatures recorded on array L, vertical, in the bulk fluid. $P_{\text{heating}} = 19.5$ W.

Initially, the temperatures were stratified as would be expected. Before this test run, warm water from a previous test was pumped out and cool water pumped in, so as to bring the tank temperature closer to ambient. However, the fill and drain tubes were both below the mid-plane of the tank, so in filling the tank, the volume was not thoroughly mixed. Consequently, the water near the top of the tank stayed warmer, even as that near the bottom cooled. This is why probes L1–L7 showed much cooler temperatures than L9 and L11.

Figure 92 shows the same data as in figure 90, but over only the first day. As heat was applied, L1–L7 heated up while L9 and L11 cooled down. Probes L1 and L2 maintained their initial relative temperatures even during heating; however, probes L3–L7 converged on a single temperature, and probes L9 and L11 eventually converged on this temperature as well. This washing out of the temperature differences as the fluid was heated is indicative of natural convective mixing of the bulk fluid by the heat flow from the start basket. In this case, the convective flow would seem to bypass the bottom of the start basket at the level of probes L1 and L2.
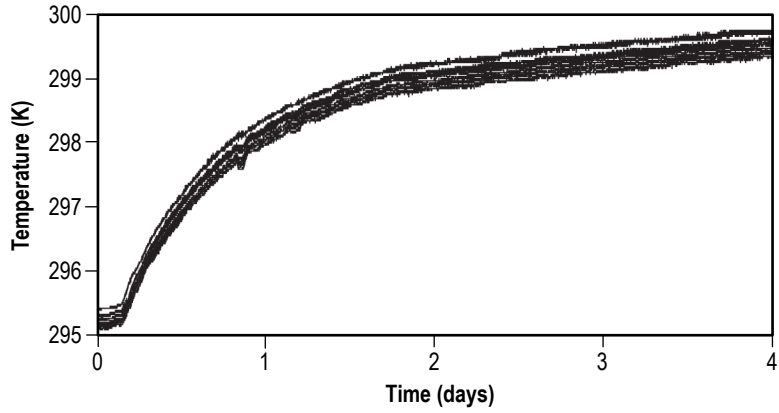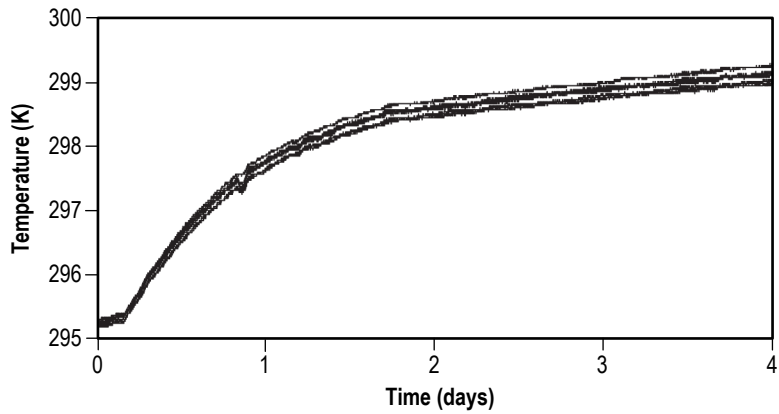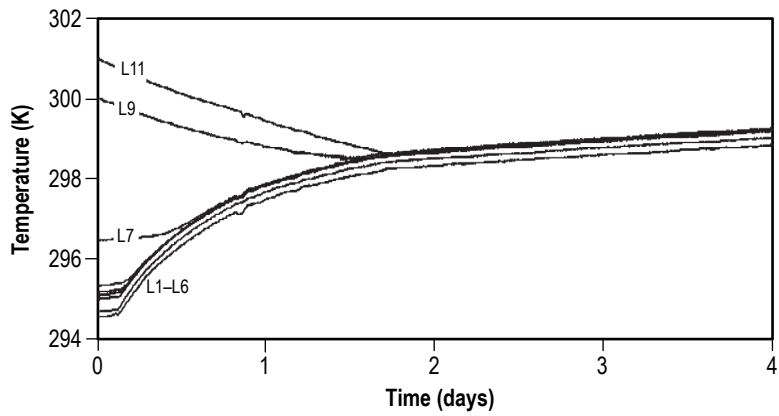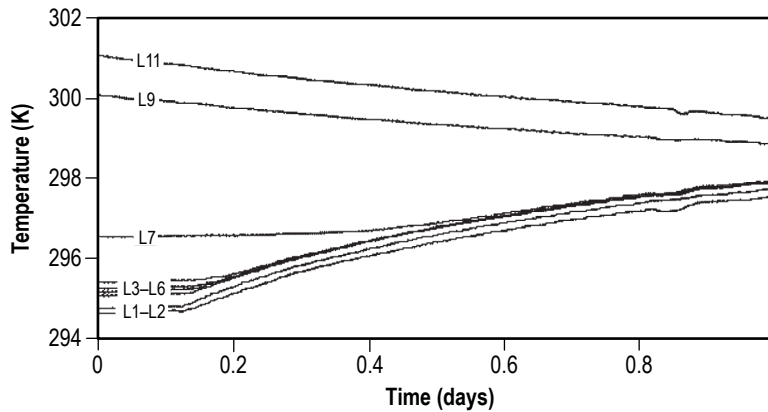

Figure 92. Temperatures recorded on array L, over the first day. $P_{\text{heating}} = 19.5$ W.

The temperatures measured by all the arrays, both inside and outside the start basket, converge to a temperature of 299.3 ± 0.3 K at the end of the 4-day-long test run, except for arrays A and J, which are closest to the feed line, and reach equilibrium temperatures 2 K warmer.

To better quantify this problem, indices that were temperature differences between certain probes are defined: four horizontal temperature indices, $\Delta T_{h1} = T_{J1} - T_{J6}$, $\Delta T_{h2} = T_{F3} - T_{C4}$, $\Delta T_{h3} = T_{H1} - T_{H7}$, and $\Delta T_{h4} = T_{H7} - T_{L6}$; and three vertical temperature indices, $\Delta T_{v1} = T_{J1} - T_{H1}$, $\Delta T_{v2} = T_{D2} - T_{G4}$, and $\Delta T_{v3} = \Delta T_{J6} - T_{H7}$. These temperature indices are illustrated in figure 93. Not every index was available for each case, as the arrays used varied for different tests.

The horizontal temperature indices for the 20 W case are shown in figure 94. There was a strong temperature gradient along the bottom plate (ΔT_{h1}), and this was due to localized heating close to the feed line. There was little variation across the top plate, or between the LAD and the bulk fluid.
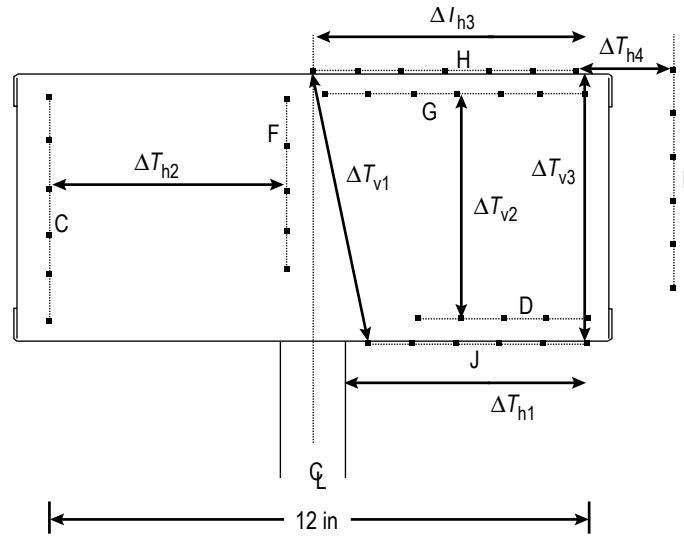
Figure 93. Definition of temperature indices.
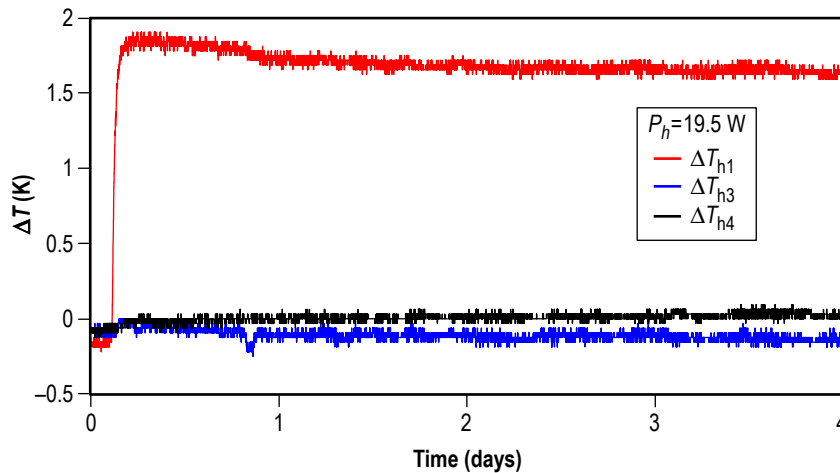
Figure 94. Horizontal temperature indices for the 20 W case. $P_{\text{heating}} = 19.5$ W.

The vertical temperature indices for this case are shown in figure 95. They start out negative due to the initial temperature stratification in the LAD. Although ΔT_{v1} is large, again reflecting the localized heating near the feed line, ΔT_{v2} and ΔT_{v3} quickly approach zero, indicating little tempera-ture gradient across the LAD from top to bottom throughout most of the LAD volume.

Figure 96 shows ΔT_{v1} over the range of heating powers used. The negative values prior to the onset of heating reflected the initial stratification in the LAD. Again, this just indicates the strength of heating where the feed line entered the LAD. The temperature differences from bottom to top in the main portion of the LAD, as characterized by ΔT_{v2} and ΔT_{v3}, respectively, became small after heat was applied, as seen in figures 97 and 98.
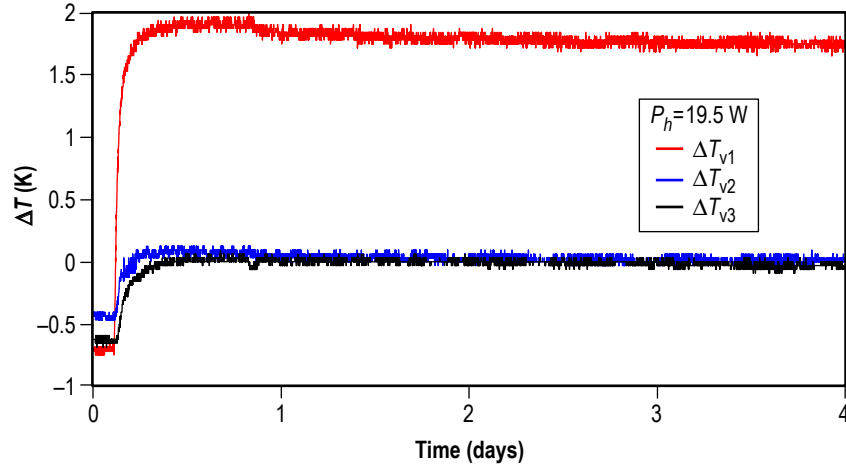
Figure 95. Vertical temperature indices for the 20 W case. $P_{\text{heating}} = 19.5$ W.
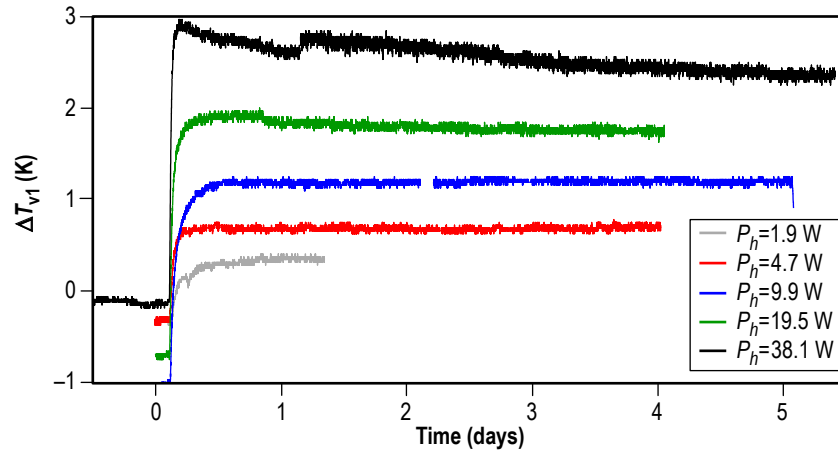
Figure 96. Vertical temperature index, ΔT_{v1}, approximately along the centerline, for different heating powers.

The radial temperature gradient across the LAD is characterized by ΔT_{h2}, shown in figure 99 for the nominal 2, 5, and 40 W cases. In this graph, the data have been smoothed for clarity. It shows a slight increase of about 0.1 K.

The difference between the LAD temperature and that of the bulk liquid is characterized by the index ΔT_{h4}, shown in figure 100. For heating powers up to 20 W, there is little or no effect observable after the onset of heating, and the bulk liquid is nearly at, or slightly below the temperature on the exterior of the LAD. At some power >20 W, however, there is a dramatic change. The heat leak through the tank wall was estimated to be ≈20 W. When the input power from the LAD is less than this, it can be thermalized in the bulk liquid. Above this, however, it would have nowhere to go, resulting in heating of the bulk.

71
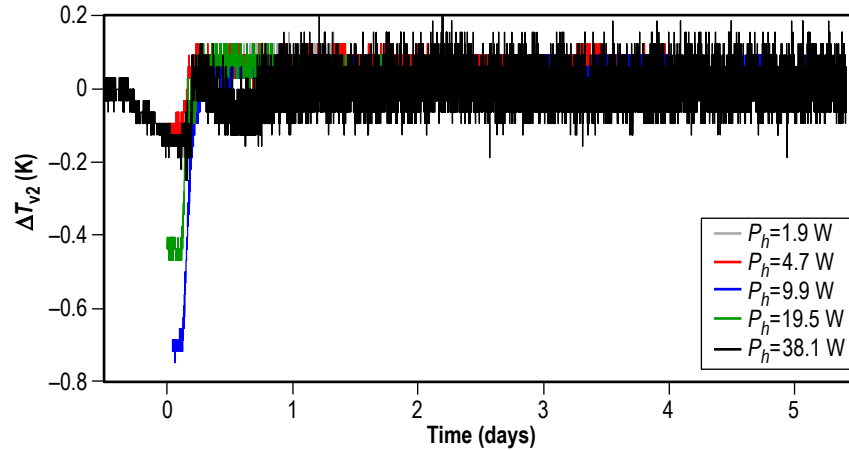
Figure 97. Vertical temperature index, ΔT_{v2}, midway out in radius, for different heating powers.
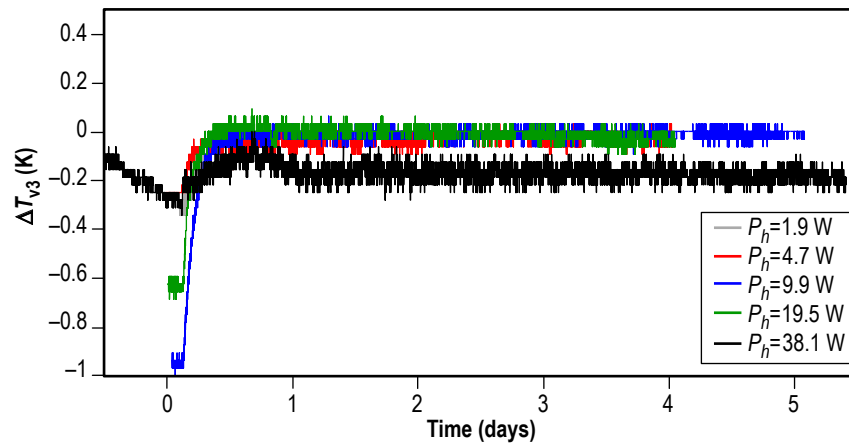
Figure 98. Vertical temperature index, ΔT_{v3}, at the edge of the LAD, for different heating powers.

6.4.2 Flow Visualization and Measurements

A second test set was conducted using the PIV apparatus described in section 6.3.2 under similar heating conditions. Four power levels were used: 9.4, 20.7, 28.4, and 37.5 W. The voltage applied to the heater was the same as in the previous corresponding cases described in section 6.4.1 (9.9, 19.5, 28.3, and 38.1 W). The fact that the resulting heating powers were slightly different is likely due to the resistance of the heater having changed somewhat. In any event, these new heating power levels are nearly the same, and the temperatures as recorded by the TC arrays were essentially the same. The time history of the temperatures recorded by three of the arrays for this new series of tests is shown in figure 101. The sudden increase in temperature at about 800,000 s was not due to an
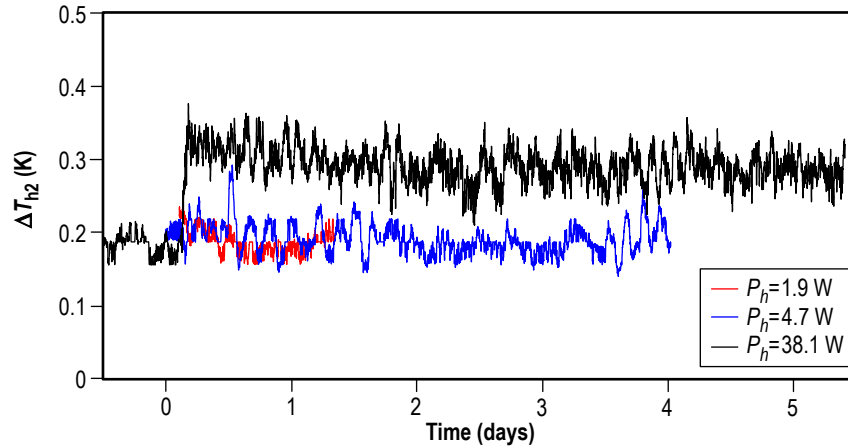
Figure 99. Horizontal temperature index, ΔT_{h2}, approximately midway up in height, for different heating powers.
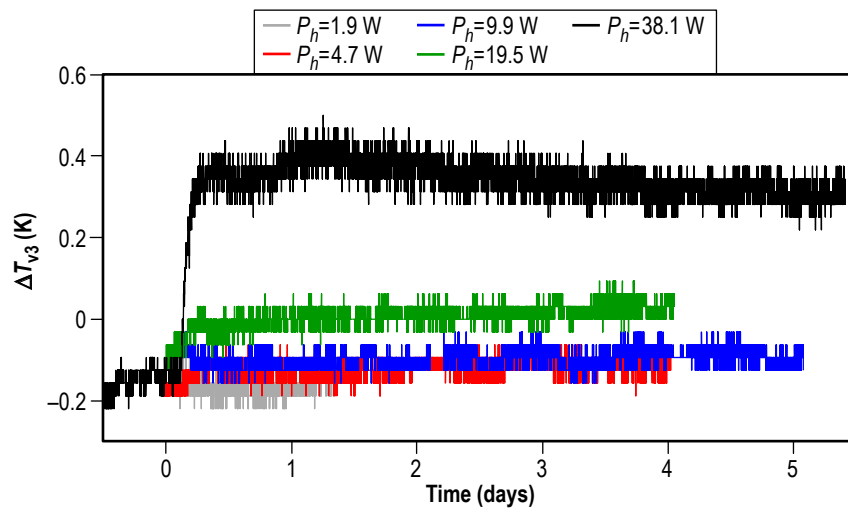
Figure 100. Horizontal temperature index, ΔT_{h4}, between the LAD and the bulk liquid, for different heating powers.

increase in the power applied to the heater, but rather to the pump operation, which was turned on to mix the water and redistribute the Kalliroscope tracer particles.

It was impractical to inject the rheoscopic tracer particles in a gentle enough manner so as not to disturb the existing flow. So instead, a large volume of particles were rapidly injected from the spray rake. This would massively perturb the flow pattern; however, the natural convective flow pattern would reassert itself within $\approx$20 min.
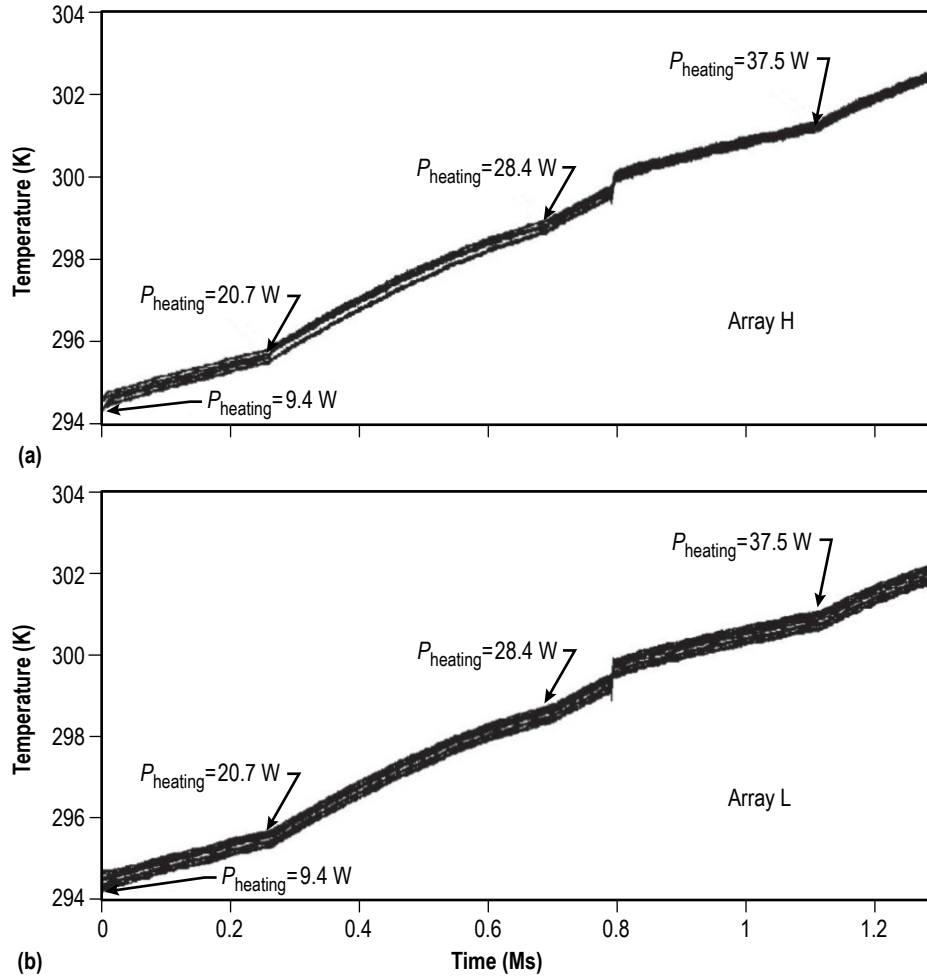
Figure 101. Time histories of temperatures recorded by TC arrays: (a) x, (b) L, and (c) H. For array locations, refer to figure 74.

The qualitative features of the flow field are exemplified by the picture in figure 102, which was taken during a test with the heating power set at 20.7 W. There is a clear boundary layer evident between a central upwelling jet directly above the LAD ($\approx$10 cm in radius), and a nearly stagnant region at larger radii. This same qualitative feature was seen with every heating power used.

Still pictures were extracted from the video files and, by following the movement of features in the curtain of rheoscopic tracer particles or by following individual particles in some cases, the flow velocities in the plane of the light sheet were determined. The radial and axial linear scale were determined from the known dimensions of the LAD and the spray rake. An example of the technique used is shown in figure 103; in this case, distinct and persistent features in the curtain of tracer particles were tracked between two images taken 17 s apart.

The two images presented in figure 103 illustrate the fluid motion as traced by persistent features in the curtain of tracer particles. The axial (red) and radial (blue) grid lines are determined from the known dimensions of the spray rake, and are then projected into the plane of the light sheet.

Figure 102. Flow field picture for heating input of 20.7 W.

Measured velocities for the nominal 10 W heating case ($P_{heating} = 9.4$ W) are shown as vector plots in figure 104. The horizontal and vertical axes are the radius (r) and height (z), respectively, measured from the top deadcenter of the LAD. The two vector plots encompass data taken from images, each spanning ≈1 min of time, and were captured after the equilibrium convective flow pattern had been established. The second vector plot (fig. 103(b)) is for a period about 40 min after the first (fig. 103(a)). The average axial flow velocity was measured to be 2.6×0.5 mm/s.The uncertainty of 0.5 mm/s was ascribed to the measurement based on the pixel resolution of the images. In the first vector plot, there is clearly also a radial component to the flow velocity. The standard deviation in the velocity measurement, σ_v, was found to be in then range of 0.14 to 0.17 mm/s. The fact that σ_v is much less than the assumed uncertainty perhaps means that the choice of uncertainty was highly conservative.

Figure 105 shows vector plots of velocity for the nominal 20 W heating case ($P_{heating}$ = 20.7 W), again, after equilibrium flow has been established. The case shown in figure 105(b) was about a day after that shown in figure 105(a). In the first case, the average axial flow velocity was found to be 3.3×0.5 mm/s with $\sigma_v = 0.2$ mm/s. In the second case, it was measured to be 3×0.5 mm/s with $\sigma_v = 0.25$ mm/s. The nominal 30 and 40 W cases are shown in figure 106 ($P_{heating}$ = 28.4 W, and $P_{heating}$ = 37.5 W, respectively). For a heating power of 28.4 W, the average axial velocity was measured to be 4.4×0.5 mm/s with $\sigma_v = 0.25$ mm/s. For a heating power of 37.5 W, the average axial velocity was measured to be 4×0.5 mm/s with $\sigma_v = 0.5$ mm/s.

One thing that falls out of this analysis is that σ_v increases with increasing power, which is expected if the flow is becoming more turbulent.
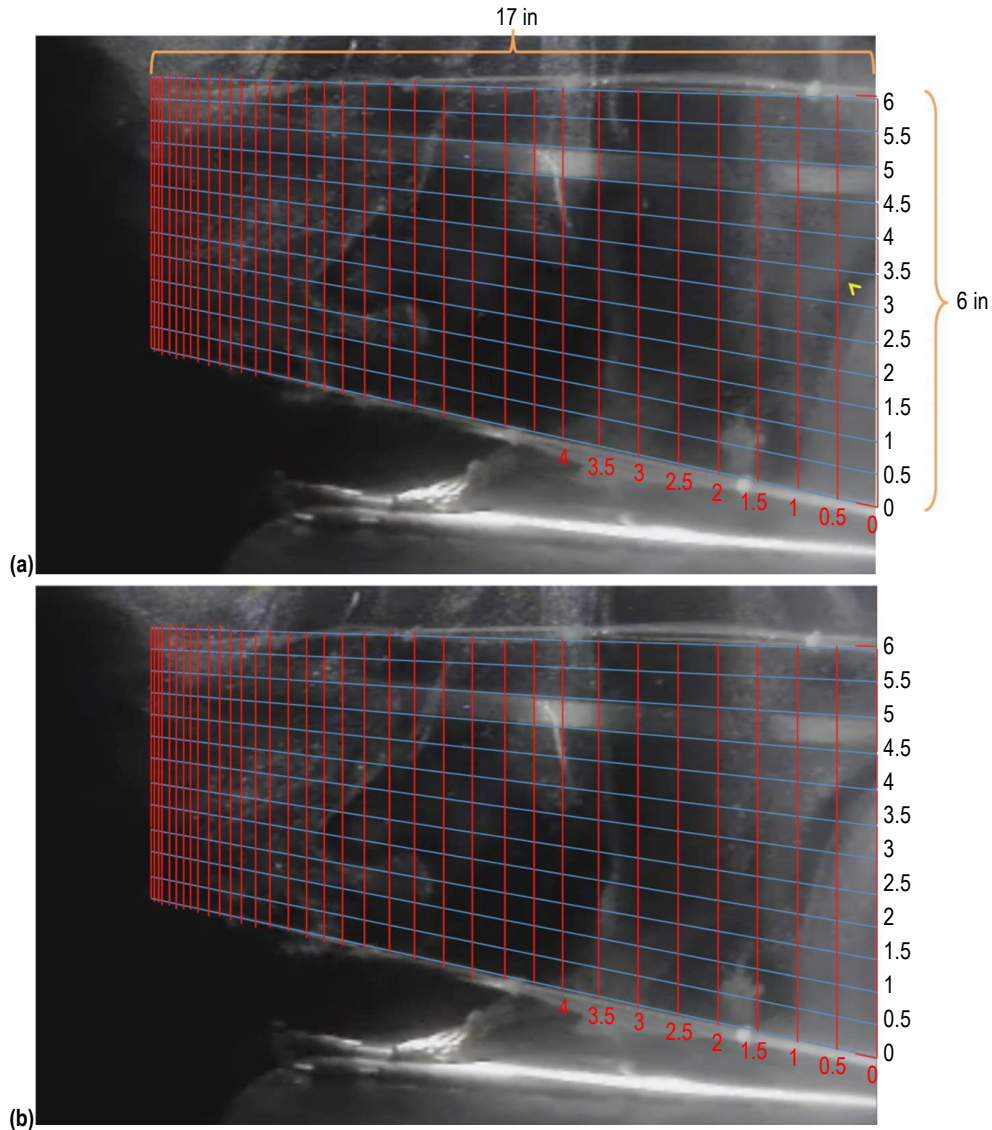
Figure 103. Fluid motion tracing result examples: (a) Flow field at time t_0 and (b) flow field at time $t_0 + 17$ s.

In summary, the measured axial flow velocity increases with increasing power, appears to become more turbulent with increasing power, and a clear boundary layer is observed that separates a central upwelling convective jet from a mostly stagnant region adjacent to the jet.

6.5 Discussion

The COMSOL model described in section 3 was run for the case of water at 293 K and normal gravity for comparison with the water test. The results of these calculations at input powers of 0.1, 0.5, 2, and 5 W are shown in figure 107. There is a convective flow in the LAD, which for $P_{heating} = 0.1$ W is laminar, but progresses to a more turbulent flow at $P_{heating} = 5$ W.

Figure 104. Vector plots of the velocity for a heating power of 9.4 W at times: (a) After equilibrium has been established and (b) about 40 min later.

The vertical temperature differences across the LAD (corresponding to ΔT_{v1}) as predicted by COMSOL for the 2 and 5 W cases are shown in figure 108. These calculations were made over a time span of several hundred seconds, much shorter than the tests. However, the calculations assume a constant heat flow into the LAD (whereas it takes a few hours to establish constant heat flow in the experimental case), and reach quasi-equilibrium within the time considered. The vertical temperature differences exhibit oscillations, especially pronounced in the 5 W case, which are not seen in the experimental data, although most of the time those data were not digitized at sufficiently high time resolution to see any such features. In those instances where higher sampling rates were used, no such features were seen. The average value of these calculated temperature differences are about twice that measured for the corresponding experimental case.

Additional trials with heating powers >5 W were attempted, but COMSOL failed to converge for these cases. The model will continue to be refined with reference to the test data.
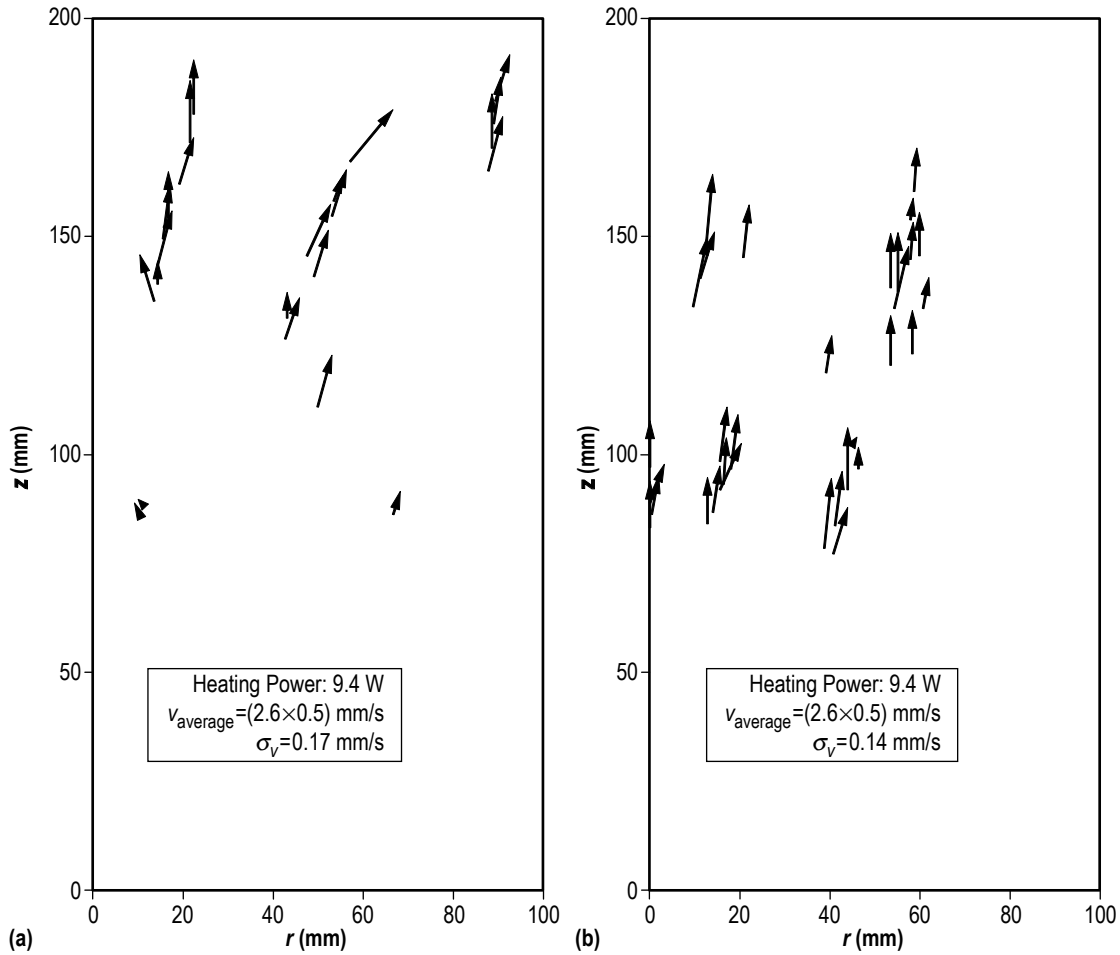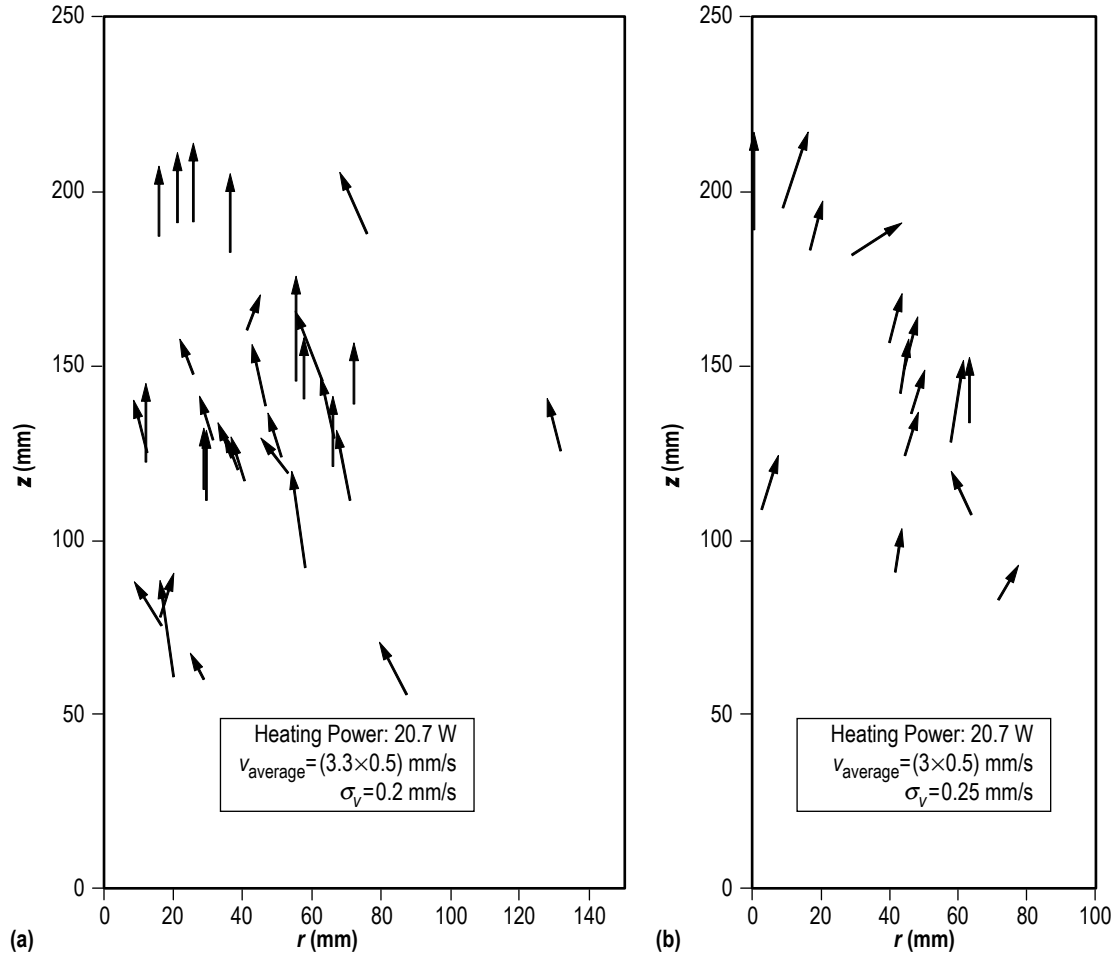
Figure 105. Vector plots of the velocity for a heating power of 20.7 W: (a) After equilibrium has been established and (b) about 1 day later.

The thermal environment of the LAD was also treated with a simple empirical scaling relationship.[3] The LAD is considered as a sphere with the same surface area as the actual LAD, which gives it a radius of $r = 170$ mm (6.7 in). The convective film heat transfer coefficient, h_f, for this idealized case is given by

$$h_f = 3.58 \left(\frac{k^3 g \beta C_P \rho^2}{\mu r} \right)^{1/4} (\Delta T)^{1/4} \, , \tag{13}$$

in MKS units, where

k = thermal conductivity
g = acceleration due to gravity
β = thermal expansivity
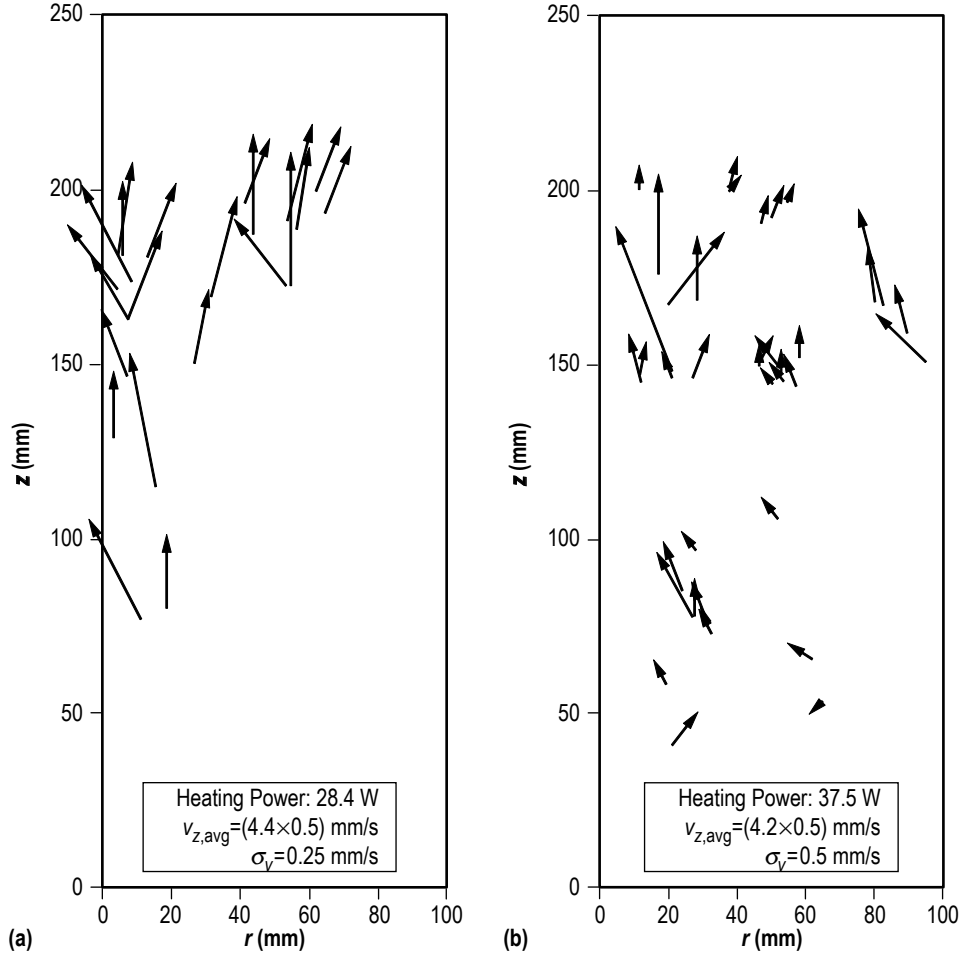
Figure 106. Velocity vector plots: (a)Heating power of 28.4 W and (b) heating power of 37.5 W.

C_P = isobaric heat capacity
ρ = density
μ = viscosity
r = radius of the sphere
ΔT = temperature drop across the film.

Equation (13) is valid so long as the Rayleigh number (N_R), given by

$$N_R \frac{R^3 g \beta C_P \rho^2 \Delta T}{\mu k} \ ,$$

(14)

is within the range $10^5 < N_R < 10^9$. For the conditions of our water test, $N_R \sim 5 \times 10^6$. Using equation (13), the total power drawn through the surface of the LAD as a function of film temperature drop is given by
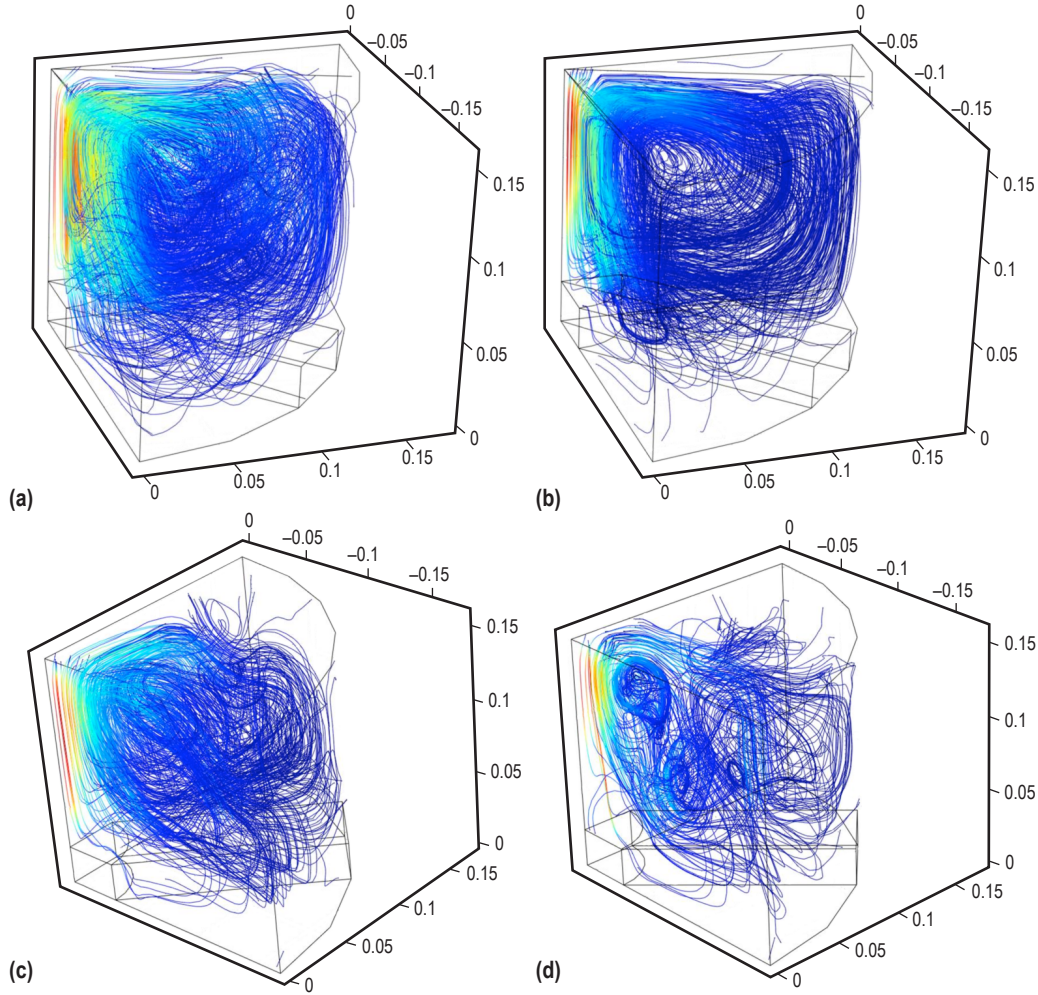
Figure 107. Flow streamlines predicted by the COMSOL model of the start basket
for different heating powers: (a) 0.1 W, (b) 0.5 W, (c) 2 W, and (d) 5 W.

$$P_{\text{out}} = h_f A_{\text{LAD}} \Delta T = a(\Delta T)^{5/4} \ , \tag{15}$$

where A_{LAD} is the surface area of the equivalent spherical LAD, and a is a constant, which for water at 293 K and 1 g is found to be $a = 345$ W/K$^{5/4}$. In equilibrium, the heat leaving the LAD will be equal to the applied heating power, $P_{\text{out}} = P_{\text{heating}}$, which yields a formula for ΔT:

$$\Delta T = \left(\frac{P_h}{345 \ \text{W/K}^{5/4}} \right)^{4/5} . \tag{16}$$

This is the temperature difference between the exterior of the LAD and the bulk liquid, as governed by natural convective heat transfer. Values of ΔT for the heating powers used in our water
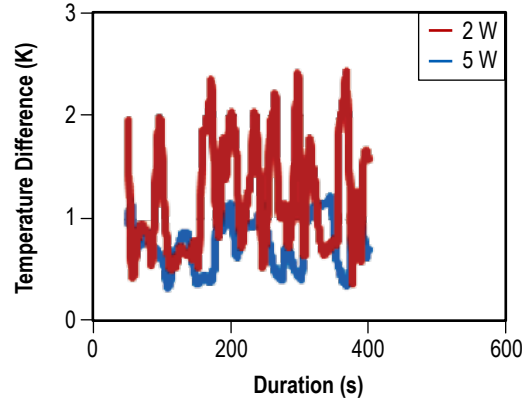
Figure 108. Vertical temperature index, ΔT_{v1}, as calculated with COMSOL for two input heating powers, $P_{\text{heating}} = 2$ W and $P_{\text{heating}} = 5$ W.

tests are given in table 5. In particular, for the 40 W case, with $P_{\text{heating}} = 38.1$ W, the calculated ΔT is 0.17 K. This is about a factor of 2 less than the corresponding temperature index, ΔT_{h4}, plotted in figure 100, reasonable agreement given the difference in geometry.

Table 5. Film temperature drop at various heating powers.

P_h (W)	ΔT (K)
1.9	0.02
4.7	0.03
9.9	0.06
19.5	0.10
38.1	0.17

Applying equation (15) to the actual case of the LAD immersed in LCH_4 on the lunar surface, with the constant evaluated for LCH_4, yields a ΔT of 10 mK for an input power of 0.75 W, compared to the calculated value of about 20 mK, mentioned in section 4.5.

Equation (16) was also applied to the case of LCH_4 in microgravity conditions ($g = 10^{-5}$ m/s^2), as would be the case during a coast period in weightlessness, the estimated temperature difference (again for a 0.66 W heat leak) is ≈ 0.1 K. For greater heat leaks, as might be expected from engine soak-back, the temperature differences can be as high as several degrees, and this could pose a problem. However this microgravity case lies well outside the domain of validity for equation (16) (as determined by the relevant dimensionless numbers), so nothing concrete can really be concluded from it. In the microgravity case, understanding the magnitude of heat entrapment will require more detailed fluid calculations. Was COMSOL modeling used or could it be used to indicate the influence of an extended 10^{-5} g condition?

7. SUMMARY AND RECOMMENDATIONS

During the past year, substantial progress has been made in a computational and laboratory investigation of heat entrapment in a representative LAD for use in the LCH_4 and LO_2 tanks for the ascent stage of a representative lunar lander concept. A comprehensive effort, the technical responsibility categories and supporting organizations were as follows: (1) Detailed thermal modeling of the LAD/feed system interactions (MSFC/EV34); (2) CFD modeling of bulk liquid thermal conditions inside the propellant tank provided interfacing conditions for the LAD thermal modeling (Boeing, Huntington Beach); (3) condensation conditioning of LAD to stabilize surface tension retention capability (MSFC/ER24, MSFC Hydrogen Test Facility, Building 4628, and The University of Alabama); and (4) system integration testing by MSFC/ER24.

7.1 Liquid Acqusition Device Thermal Analyses

Initial modeling of conditions inside the LAD were performed using heated/cooled flat plate empirical data. However, it soon became apparent that higher level modeling was required to determine convective film coefficients inside the LAD in the 1/6 g lunar environment. Therefore, a commercially available model termed COMSOL was first used to develop a two-dimensional, axisymmetric thermal model to evaluate trends and sensitivities. This modeling was followed with a full three-dimensional simulation in one quadrant of the LAD, and includes the heat conduction of the LAD components as well as CFD modeling of the liquid within the LAD. Following this, a further refinement to the COMSOL model was added: the entire LAD/tank system was simulated in a two-dimensional axisymmetric geometry using a turbulent flow model.

7.2 Bulk Liquid Computational Fluid Dynamics Modeling

A FLOW-3D CFD investigation of bulk liquid conditions in the tank provided the outer boundary conditions for a detailed thermal model of the LAD itself. Additionally, the thermal control modeling provided data regarding ullage pressure control, i.e., self-pressurization and pressure reduction via mixing. Flow visualization measurements were made to better characterize the integrated system. The flow velocities measured (in the range of 2.6 to 4.4 mm/s for heating powers spanning the range of about 10 to 40 W) agreed qualitatively with the predictions of the COMSOL model. With higher heating power, the measured velocities increased, and were found to become more irregular (as characterized by the standard deviation in the flow velocity), indicative of a more turbulent flow.

The combined observations regarding the preceding LAD thermal analyses and bulk liquid CFD modeling are as follows:

- After 20 to 30 days, the accumulated thermal energy within the LAD levels out at <2% of the total heat leak into the LAD volume.

- The bulk liquid within the LAD is generally <1 K warmer than the tank bulk liquid.

- A warm layer of liquid, ≈0.06 K above the bulk propellant, could accumulate around the LAD exterior.

- Lunar gravity is sufficient to support chaotic turbulent mixing in the LAD bulk liquid and within the acquisition channels, i.e., buoyancy is sufficient to support heat transfer via natural convection.

- With microgravity, laminar circulation occurs within the acquisition channels.

- If the mixer flow rate falls below 3.75 lpm (1 gpm), even with cool TVS outlet temperatures, the cool liquid falls to the tank bottom and the ullage pressure continues to rise.

7.3 Condensation Conditioning

The use of condensation techniques to stabilize and enhance the LAD bubble point is being analytically and experimentally pursued. A concept demonstration successfully transferred and collected LN_2 condensate against Earth's gravity. Wicking tests with alcohol indicated faster wicking perpendicular to the warp wires, except with 165×880 mesh. Excellent analytical correlations were achieved with both vertical and horizontal wicking. Capillary and hydraulic diameters are different and both should be considered in the theoretical model. Evaporation was noticeable in both horizontal and vertical testing and must be prevented in future uptake testing. When liquid velocity or movement was perpendicular to the warp wires, the wicking front was horizontal or parallel to the warp wires. When the wicking movement was parallel to the warp wires, the front was inclined to the warp wires, i.e., parallel to the shute wire direction.

Preparations for wicking tests with LN_2 are nearing completion and final checkouts are in progress. Preliminary analytical modeling of condensate film flow on a horizontal disc indicates that the surface profile is concave up at low Bond numbers and is concave down at high Bond numbers. Future modeling should be extended to include interfacing with the presence of helium pressurant.

7.4 System Integration Testing

Subscale LAD tests were conducted over a range of input powers, roughly 2 to 40 W. The results of these tests indicated that, at these power levels, there was natural convective flow both within and around the LAD, enough to bring the LAD to thermal equilibrium with the bulk liquid. The experimentally measured temperature drop between the LAD and the bulk liquid were found to agree (within a factor of 2 or so) with a simple empirical relation for convective film heat transfer.

7.5 Final Observations/Conclusions

The following are some final observations:

• Based on the conditions evaluated, the degree of heat entrapment does not appear to be a problem. However, because the ascent engine might be used as an abort mode should there be problems during lunar descent, further thermal analyses of the extended microgravity coast period is recommended.

• The FLOW-3D CFD program is substantially improved as a result of being challenged with the baseline thermodynamics. Several problems with the code were revealed and corrected as a consequence.

• Other important improved capabilities include thermal modeling in reduced gravity; capillary screen conditioning to stabilize LAD performance; understanding LAD/feed system thermal and fluid integration; and setting up and using hardware for quick turnaround experimental studies. These enhanced capabilities probably would not currently exist if the Heat Entrapment program had not been pursued.

REFERENCES

1. Bolshinskiy, L.G.; Hastings, L.J.; and Statham, G.: "Cryogenic Capillary Screen Heat Entrapment," *Cryogenics*, Vol. 48, No. 5–6, pp. 232–237, 2008.

2. Symons, E.P.: "Wicking of Liquids in Screens," *NASA TN D-7657*, NASA Lewis Research Center, Cleveland, OH, May 1974.

3. Lauer, B.E.: "Table of Heat Transfer Coefficients," *Oil and Gas Journal*, August 18, 1952 to November 2, 1953.

4. Chato, D.J.: "Cryogenic Technology Development for Exploration Missions," *NASA/TM—2007–214824* (AIAA–2007–0953), NASA Glenn Research Center, Cleveland, OH, September 2007.

5. Hastings, L.J.; Bolshinskiy, L.; Martin, A.; et al.: "Liquid Acquisition/Heat Entrapment FY09 Final Report," ER24-HeatEntrap-04, Marshall Space Flight Center, AL, September 30, 2009.

REPORT DOCUMENTATION PAGE

1. REPORT DATE (DD-MM-YYYY) 01–11–2011	2. REPORT TYPE Technical Publication	3. DATES COVERED (From - To)

4. TITLE AND SUBTITLE

Thermal Integration of a Liquid Acquisition Device Into a Cryogenic Feed System

5a. CONTRACT NUMBER

5b. GRANT NUMBER

5c. PROGRAM ELEMENT NUMBER

6. AUTHOR(S)

L.J. Hastings,* L.G. Bolshinskiy,** R.G. Schunk, A.K. Martin, R.H. Eskridge, B.D. Hamill, C.F. Gomez, A. Frenkel,*** G. Grayson,† and M.L. Pendleton‡

5d. PROJECT NUMBER

5e. TASK NUMBER

5f. WORK UNIT NUMBER

7. PERFORMING ORGANIZATION NAME(S) AND ADDRESS(ES)

George C. Marshall Space Flight Center
Huntsville, AL 35812

8. PERFORMING ORGANIZATION REPORT NUMBER

M–1323

9. SPONSORING/MONITORING AGENCY NAME(S) AND ADDRESS(ES)

National Aeronautics and Space Administration
Washington, DC 20546–0001

10. SPONSORING/MONITOR'S ACRONYM(S)

NASA

11. SPONSORING/MONITORING REPORT NUMBER

NASA/TP—2011–216474

12. DISTRIBUTION/AVAILABILITY STATEMENT

Unclassified-Unlimited
Subject Category 20
Availability: NASA CASI (443–757–5802)

13. SUPPLEMENTARY NOTES

Prepared by the Spacecraft and Vehicle Systems Department, Engineering Directorate
*Alpha Technology, Inc., **The University of Alabama in Huntsville, ***The University of Alabama, Tuscaloosa †Boeing Company, ‡Jacobs Engineering

14. ABSTRACT

Primary objectives of this effort were to define the following: (1) Approaches for quantification of the accumulation of thermal energy within a capillary screen liquid acquisition device (LAD) for a lunar lander upper stage during periods of up to 210 days on the lunar surface, (2) techniques for mitigating heat entrapment, and (3) perform initial testing, data evaluation. The technical effort was divided into the following categories: (1) Detailed thermal modeling of the LAD/feed system interactions using both COMSOL computational fluid device and standard codes, (2) FLOW-3D modeling of bulk liquid to provide interfacing conditions for the LAD thermal modeling, (3) condensation conditioning of capillary screens to stabilize surface tension retention capability, and (4) subscale testing of an integrated LAD/feed system. Substantial progress was achieved in the following technical areas: (1) Thermal modeling and experimental approaches for evaluating integrated cryogen LAD/feed systems, at both the system and component levels, (2) reduced gravity pressure control analyses, (3) analytical modeling and testing for capillary screen conditioning using condensation and wicking, and (4) development of rapid turnaround testing techniques for evaluating LAD/feed system thermal and fluid integration. A comprehensive effort, participants included a diverse cross section of representatives from academia, contractors, and multiple Marshall Space Flight Center organizations.

15. SUBJECT TERMS

low-gravity cryogenic fluid management, lunar propulsion, cryogenic liquid acquisition device/feed system thermal integration capillary screen wicking analyses and testing, capillary screen heat entrapment

16. SECURITY CLASSIFICATION OF:			17. LIMITATION OF ABSTRACT	18. NUMBER OF PAGES	19a. NAME OF RESPONSIBLE PERSON STI Help Desk at email: help@sti.nasa.gov
a. REPORT U	b. ABSTRACT U	c. THIS PAGE U	UU	100	19b. TELEPHONE NUMBER (Include area code) STI Help Desk at: 443–757–5802

National Aeronautics and
Space Administration
IS20
George C. Marshall Space Flight Center
Huntsville, Alabama 35812